Ph.D. Thesis

Defect and Surface Properties of the Silver Halides

Daniel John Wilson

Davy Faraday Research Laboratory,

The Royal Institution of Great Britain, London.

&

Department of Chemistry,

University College London.

May 2005

ProQuest LLC
789 East Eisenhower Parkway
P.O. Box 1346
Ann Arbor, MI 48106-1346

Abstract

In this thesis, state-of-the-art density functional theory calculations have been performed to study a number of properties of the rocksalt-structured silver halides which can broadly be defined as photographically-relevant. These involve point defects and their interaction with free electrons and holes, created upon excitation by actinic light.

In our initial calculations, we studied the primary intrinsic point defects within the bulk of the material, in both charged and neutral forms, using the supercell technique. We have correctly predicted the dominance of the Frenkel defect in both AgCl and AgBr, and have found that the lowest energy configuration for the interstitial cation defect in both materials involved a second cation, forming a Ag_2^{2+} split-interstitial species, orientated in a <111> direction.

We then extended this work by applying a hybrid QM/MM embedding technique to model two systems: the first represented the ideal (100) surface, while the second represented a 'realistic' finite cluster. With the first, we have calculated defect structures and formation energies on the flat surface, and have examined the well-known space-charge layer. With our finite cluster, we studied extended surface defects (steps, kinks etc.) and their interaction with individual point defects.

We have also calculated trap depths, and the localisation of holes and electrons at each of the sites. We have determined that, regardless of their location, an electron diffusely localises around the interstitial cation and strongly localises on the anion vacancy, while the corresponding hole becomes trapped around the cation vacancy on a nearest-neighbour cation. However, overall, we consider the positive kink on the surface to be the most likely electron trap, due to its relative abundance and its position within the band gap.

Finally, we have investigated the properties of the latent pre-image centre, which plays a key rôle in the photographic process.

Acknowledgements

Many people have helped and encouraged me over the course of my Ph.D. research. However, I'd like to keep this section as short as possible. Not because I'm ungrateful, but because I sincerely hope that I have already thanked those to whom I am indebted. Having said that, I'd like to mention a number of people who have been crucial to getting me this far.

I would like to thank my supervisor Richard Catlow for his help, guidance and for many useful discussions. I'd also like to thank Sally Price for her additional supervision.

For daily discussions, theoretical and technical help, and not-least their friendship, I must thank Alexey Sokol and Sam French. Thanks also to Paul Sherwood of the Daresbury Laboratory for the generous support he provided for the ChemShell package.

I would like to thank Eastman Kodak for funding this project, and in particular, Thomas Pawlik for useful advice and for his hospitality during my visit to Rochester. I must also thank Roger Baetzold for his help, enthusiasm, and for the many papers he has published on this subject, which were invaluable in getting me started with this work.

I would also like to acknowledge the UK Car-Parinello consortium for access to the academic versions of the CASTEP code, Accelrys for the use of their Materials Studio visualisation suite, and to HPCx, CSAR and the Materials Chemistry Consortium for access to supercomputing facilities, without which this work would not have been possible.

Finally, on a more personal note, I'd like to thank both Kat and my family for their never-ending support.

Publications To Date

Some of the work contained within this thesis has previously been published in the following papers:

D. J. Wilson, A .A. Sokol, S A French, and C. R. A. Catlow. Defect Structures in Silver Chloride. *J. Phys.: Condens. Matter*, **16** (2004) S2827-S2838,

D. J. Wilson, A .A. Sokol, S A French, and C. R. A. Catlow. The Role of Defects in Photographic Latent Image Formaion. *Mater. Res. Soc. Symp. Proc.*, **848** (2005) FF7.6.

Contents

List of Tables

List of Figures

Introduction to This Thesis

Background

The rôle of crystalline defects in the silver halide photographic process has long been recognised. Consequently, these materials have been very widely studied in the literature, with details of the static, dynamic, electronic, surface and defect properties having been well established. Experimentally, the atomic-scale defect properties must be inferred from ionic conductivity or thermal expansion data. Computer modelling can now be applied to problems such as these in order to gain new insights into their structural and electronic properties.

Previously, calculations have been performed to improve our understanding of the processes behind latent image formation. However, these have largely concentrated upon the most industrially-relevant aspects, such as the growth of the latent image cluster and the effects of extrinsic dopants. To our knowledge, relatively little work has been done on the earlier stage of process: the 'nucleation' of the latent image cluster.

In this work we have therefore applied modern computational techniques, based upon density functional theory, to study the properties of defects in the silver halides both in the bulk crystal, and on the important (100) surface. We have also extended this work to analyse key aspects of the nucleation process.

This work has been performed using two independent, but complementary, techniques. First, the supercell method has been applied to bulk defects. This method was chosen for its conceptual simplicity, and because it has previously been applied to model defects in a wide variety of materials. Our second method, based upon an embedded-cluster model, is considerably more involved, but potentially overcomes the limitations associated with the use of a supercell. Here, a quantum mechanically-described cluster of ions, containing the defect species, is embedded in a computationally-inexpensive environment which reproduces the

effects of the infinite lattice.

Using these techniques, we have for the first time studied the properties of point defects in the rocksalt-structured silver halides using quantum-mechanical calculations. We have also investigated the corresponding neutral point defects in attempt to understand electron and hole trapping processes within the bulk – properties of particular relevance to latent image formation.

With the embedded cluster method we have extended our calculations to study defects on the (100) surface and at bulk-like locations, reproducing the experimentally-measured space-charge layer. For the first time, we have determined the positions of the defect levels within the band gap, allowing us to ascertain the fate of free electrons and holes in the conduction and valence bands. These results suggest that the surface positive kink site is the primary electron trap in the silver halides, in agreement with the hypothesis of the direct photolysis mechanism, and that the kink strongly reconstructs in order to stabilise the electron in this location. Finally, on the basis of this work, we have suggested a formation mechanism for the latent pre-image centre.

It is worth noting that despite recent progress in digital photography, the conventional silver halide process retains its scientific relevance due its fundamental nature. Perhaps more importantly, the silver halides represent interesting materials which display a number of intriguing properties which are not yet fully understood, but can now be investigated using computer modelling.

Plan of This Thesis

In Chapter 1 we introduce the silver halides, paying particular attention to what distinguishes them from the apparently-similar alkali-metal halides. A description of the photographic process is then given which, although by no means comprehensive, should provide a flavour of the relevance of this work. A brief description of the relevant theory and methods is then given in Chapter 2.

The remaining chapters are dedicated to the results of our calculations, each one describing the results of a different technique. Chapter 3 is concerned with the use of semi-classical methods. Here we review the accuracy of current shell-model interatomic potentials for the silver halides and report the development of new potentials tailored for use in QM/MM embedding. Chapter 4 reports our work on defects in the bulk of the silver halides which, as described above, used

the supercell approach. Our complementary work using the embedded cluster method is then reported in Chapter 5.

Finally, Chapter 6 contains a discussion of the relative merits of each method, along with our final conclusions.

Chapter 1

Introduction

The silver halides are fascinating materials whose simple structures belie complex and intriguing properties. Silver chloride and silver bromide have been the prime materials of the photographic industry for over a century. They have retained this dominance, despite their relative expense, as no other materials have been able to provide the combination of properties required for this complex process to function.

The work in this thesis is concerned with understanding the basic rôle of structural defects in the process of latent image formation (i.e. the stage of the photographic process that occurs *within* the camera). In this chapter, the silver halides will be introduced, and their unique properties will be described. Their rôle in their photographic process will be outlined, and the questions this work will attempt to resolve will be described.

1.1 The Silver Halides

The first three silver halides (fluoride, chloride and bromide) adopt the rock-salt structure, while under standard conditions silver iodide adopts the wurtzite structure, as illustrated in Figure 1.1. Of these, silver chloride (AgCl) and silver bromide (AgBr) are the most widely used, and therefore the most widely studied, members of the family. Silver fluoride (AgF) is hygroscopic, thus making it unsuitable both for experimental examination, and for commercial use. Conversely, it is the extreme insolubility of silver iodide (AgI) that limits its use.

This work is therefore concerned primarily with the properties of AgCl and

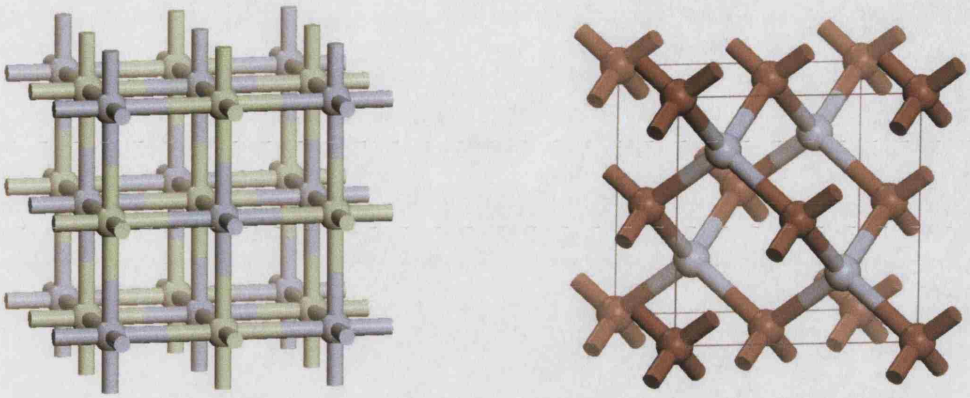

Figure 1.1: The rocksalt [left] and wurtzite [right] structures belonging to AgX (X=F,Cl,Br) and AgI respectively. Throughout this thesis, blue spheres represent silver cations, while green and brown spheres represent chloride and bromide anions respectively.

AgBr, although some predictions have also been made for AgF in Chapter 4. Despite the apparent similarity of these materials to the alkali halides, their properties differ widely. For example:

- they show a degree of directionality in their bonding,
- there is a strong Cauchy violation in the elastic constants (i.e. $C_{12} \neq C_{44}$),
- there is an inversion of the transverse acoustic and transverse optic branches of the phonon dispersion curves at the L-point of the Brillouin zone,
- they have an indirect band gap, with the valence band maximum at the L-point in reciprocal space,
- the form of the intrinsic defects, and their characteristic properties, are unique.

The reason for these differences is, of course, the presence of the silver cation. However, the types of behaviour described above are due to different aspects of its atomic structure and its interaction with the halide counter-ion. In the following sections these features will be explored.

1.1.1 Structural Properties

The cubic lattice parameters for AgCl and AgBr have been measured to be 5.51Å and 5.77Å at absolute zero. Already, this represents an anomaly as these values are considerably smaller than those calculated from the Pauling ionic radii[1] – an approximation which works well in the alkali halides.

Bucher has proposed that this bond-shortening is due to the strong van der Waals attraction between the ions.[2] Indeed, a number of classical interatomic potential calculations have also found that a large van der Waals coefficient is required in order to model the silver halides accurately.[3–5] To support his hypothesis, Bucher employed interatomic potentials in which the van der Waals coefficients were artificially reduced to the values used in the alkali halides.[6] As a result, the new materials took on many of the properties of the alkali halides, including the additivity of the experimental ionic radii. However, it is unlikely that this is a true van der Waals-type interaction. While it is certainly the case that the silver cation is more polarizable than an alkali-metal cation, one would not expect van der Waals coefficients considerably in excess of the experimentally-determined Mayer values*, as has been necessary in all previous studies.[3,7,8] The C_6 coefficient in these classical calculations represents all interactions with an r^{-6} dependence. It is possible that some missing feature of the model, such as quadrupolar deformability or partial-covalency, may be compensated in the mathematical fitting procedure by an increase in this term.

Interestingly, Density Functional Theory calculations, which include some description of electron correlation, but do not model long-range van der Waals attraction, reproduce the experimental lattice parameter reasonably well. In contrast, Hartree-Fock calculations, with no electron correlation, greatly overestimate this quantity.[9] This result again would suggest that Bucher's C_6 term is not a true van der Waals interaction.

1.1.2 Elastic and Dynamical Properties

In the 1970s, the phonon dispersion curves of AgCl[10] and AgBr[11] were measured using neutron scattering techniques (see Figure 1.2). It has been determined that in order to model the phonon dispersion curves of the silver halides accu-

*Mayer combined data from ultraviolet absorption with ionic polarizabilities to obtain values for the van der Waals coefficients, claimed to be accurate to within 15%.

rately, some description of the quadrupolar deformation of the cation must be included.[12–17] Indeed, atomistic calculations including these terms reproduce the experimental data with great accuracy,[11,12,17] while those that do not, fail to reproduce key features.[5,10]

This deformability will affect different vibrational modes of the crystal to different extents. Clearly, the modes involving the movement of planes of cations (such as the planes normal to <111>) will be some of the most significantly altered. Indeed, the transverse optical (TO) mode has an unusually low frequency at the L-point, as can be seen in Figure 1.2.

It has been argued that quadrupolar deformability is due to virtual $d - s$ excitations at the Ag^+ ions, due to the small band-gap between the d-like valence band and the s-like conduction band. The tight-binding calculations of Kleppmann and Weber[14] supported this assumption, finding the crystal-field matrix elements representing these intra-atomic transitions to be sizable. The authors provided a good fit to experimental phonon dispersion curves, and suggested that the instability of FCC silver iodide must be largely of the same origin.

The elastic constants of the silver halides are also affected by this deformability. In a crystal with cubic symmetry, the elastic constants will obey the Cauchy relation $C_{12} = C_{44}$ if the bonding is central and pairwise in nature. While this condition holds approximately for the majority of alkali halides, a number of experimental studies have shown that in AgCl and AgBr there is a very strong violation,[18–20] with $C_{12} \approx 5C_{44}$. This effect can be treated as a measure of the many-body nature of the bonding in the silver halides, which is a combined result of the quadrupolar deformability and the partial-covalency described in the previous section.

1.1.3 Electronic Properties

In the alkali halides, which have a direct band gap, the optical absorption spectrum is composed of an intense band in the UV region.[21] The silver halides show similar behaviour, but with the addition of an extended, temperature-dependent, tail into the visible region.[22] It was first proposed by Seitz in 1951 that this may be due to the valence band maximum being at a position other than the gamma-point in reciprocal space.[22] With the conduction band minimum located at the gamma-point, this behaviour leads to an indirect band gap. Excitations

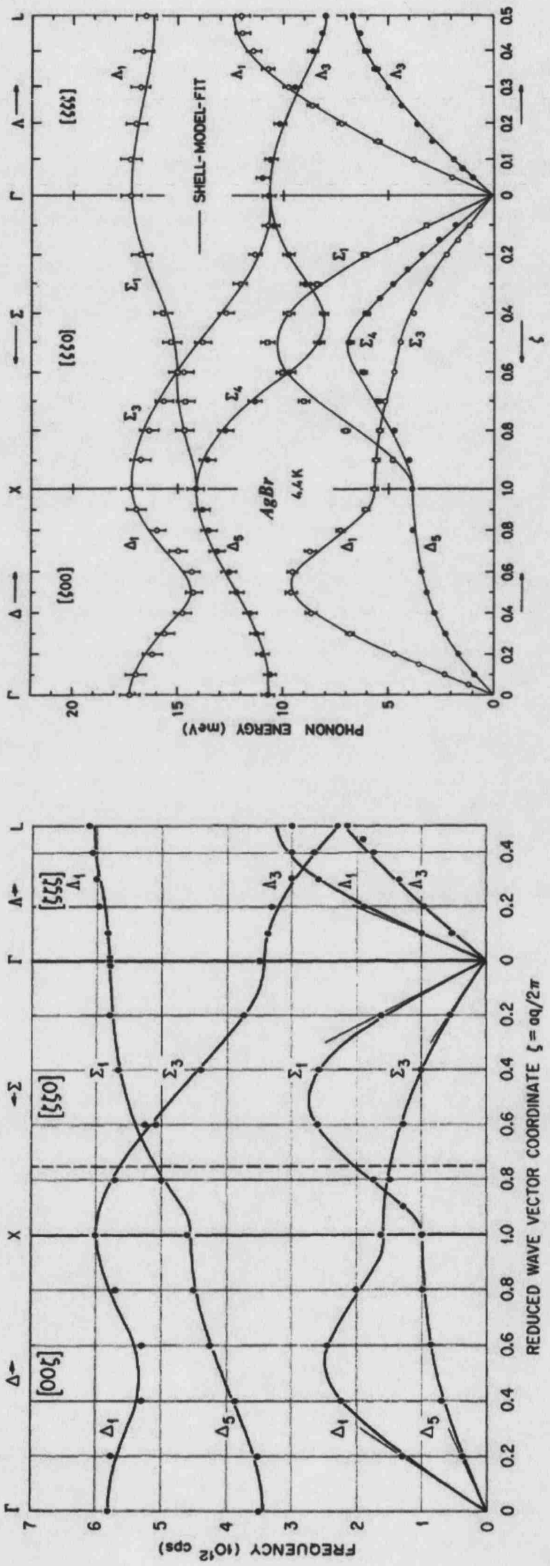

Figure 1.2: The experimental phonon dispersion curves for AgCl[10] [left] and AgBr[11] [right]. For the case of AgBr, a shell-model fit which includes the effects of quadrupolar deformation, has been overlaid by the authors.

must therefore be phonon-assisted, reducing their probability, and introducing a strong temperature-dependence. The intense band in the spectrum would result from the direct exciton transition at higher energies.

It was later suggested by Krumhansl that this valence band structure could be explained by realising that, in the Madelung potential of the crystal, the silver $4d$ level coincides with the halogen $3p$ (AgCl) or $4p$ (AgBr) level to within 1eV.[23] Due to the inversion symmetry of the crystal, the levels cannot mix at the gamma-point. However, towards the zone boundaries, they hybridise and spread, causing the inverted valence band proposed by Seitz. This hybridisation is likely to be the cause of the bond-directionality, or partial-covalency, discussed above.

These features of the band structure have been experimentally verified. Using cyclotron resonance techniques, Tamura and Masumi established that the valence band in AgBr is located at the L-point.[24] Electron transport studies have also confirmed that the conduction band minimum in AgBr is at the gamma-point in reciprocal space.[25,26] The direct and indirect band gaps in AgCl and AgBr have also been verified by optical absorption spectroscopy,[27,28] and are reproduced in Table 1.1.

Table 1.1: Experimental indirect and direct band gaps / eV.

	AgCl	AgBr
Indirect Gap	3.245	2.684
Direct Gap	5.13	4.276/4.820*

*Doublet due to large spin-orbit splitting.

There have also been a large number of computational studies ranging from early LCAO[29,30] and APW[31] calculations through to accurate Hartree Fock,[32,33] post-Hartree Fock[9] and Density Functional based methods.[34–40] As would be expected from experience with other materials,[41] the Hartree Fock calculations overestimate and Density Functional calculations underestimate the band gaps. However, they all show qualitative agreement, and confirm the $p-d$ mixing in the valence band[29] and the largely s-like character of the conduction band.[38,39]

Irradiation with light of sufficient energy will create an electron-hole pair, or exciton. This pair can become self-trapped in the pure material, and is believed to consist of a self-trapped hole (STH) with a weakly bound electron.[42] The binding energy of these self-trapped excitons (STE) is small: 0.022eV in AgBr

and 0.04eV in AgCl.[25] Hence, they readily dissociate at room temperature into free electrons and holes.

The free electron in the defect-free bulk silver halides will diffuse efficiently, only limited by scattering from phonons. Accordingly, they have large room temperature drift mobilities of 50 $cm^2V^{-1}s^{-1}$ for AgCl[43] and 60 $cm^2V^{-1}s^{-1}$ for AgBr.[44] Conversely, the hole can become self-trapped within the lattice, severely limiting its mobility to just 0.02 $cm^2V^{-1}s^{-1}$ for AgCl[45] and 1 $cm^2V^{-1}s^{-1}$ in AgBr.[46]

This STH is known to be localised on a single silver ion.[47,48] As a result of this localisation, a Jahn-Teller distortion occurs, splitting degenerate valence band states, and producing a bound state which is stable to 50K.[49,50] This process relies upon the unique valence band structure of the silver halides which, as discussed earlier, have appreciable cation character.

1.1.4 Defect Properties

Structural defects occur in all natural crystals as a consequence of the second law of thermodynamics: their presence introduces degrees of freedom, and hence entropy, into the system. In binary ionic materials such as the silver halides, point defects in their ground state will be charged, and thus must exist as part of a neutral pair. In the silver halides, the dominant form are of the Frenkel type, on the silver sub-lattice.[22,51] Thus they consist of silver vacancies (V_{Ag}^-) and silver ions in interstitial regions of the crystal (Ag_I^+), which is not the case for the vast majority of rocksalt-structured materials which favour Schottky-pairs, consisting of cation and anion vacancies (V_{Ag}^-/V_X^+).

Early estimates of the concentration and formation energies of defects in the silver halides were based on detailed analyses of thermal expansion data.[52,53] However, more accurate values have since been obtained from ionic conductivity data, which are highly dependent upon both the form of the defects and their concentrations.[54–58] The values quoted by Friauf[56] are reproduced in Table 1.2.

The presence of defects in a crystal dramatically alters the behaviour of electrons and holes produced on photo-excitation. For instance, the famous F-centre in the alkali halides is formed when a free electron becomes trapped within an anion vacancy.[59] In the silver halides, anion vacancies do not exist in concentrations great enough that F-centres can be detected. The only other centre capable

Table 1.2: Experimental defect properties, from Reference 56.

	AgCl	AgBr
Frenkel Defect Formation Enthalpy / eV	1.49 ± 0.02	1.16 ± 0.02
Defect Concentration / cm^{-3}	1.15 x 10^{12}	9.80 x 10^{13}

of trapping an electron is the interstitial silver cation. ENDOR spectroscopy has been applied to this system and it has found that the trap depth is very small, resulting in a very delocalised electron.[60,61]

The corresponding cation vacancy is thought to be an efficient hole-trap.[50,62,63] The isolated STH is stable only up to 50K, but when it becomes complexed to a cation vacancy its EPR signal persists up to 110K.[50] While the higher-resolution ENDOR spectroscopy of Bennebroek *et al.* showed no signal pertaining to the presence of a vacancy,[48] the experiments were performed both at much lower temperatures (at which isolated STHs would be expected to dominate), and with larger crystals in which the defect concentration is smaller (as discussed in further detail in Section 1.1.6).

1.1.5 Defect Migration

The analysis of the conductivity measurements mentioned in the previous section depends upon a detailed model of the migration mechanisms involved. It has been found that the mobility determined through ionic conductivity considerably exceeds that found using self-diffusion measurements and the Einstein relation.[64,65] This discrepancy is due to correlation in the migration path, and led to the proposal that the interstitialcy migration dominates in the silver halides.[64,65] In this mechanism, a cube-centred interstitial ion pushes a neighbouring lattice site ion into an interstitial region, taking its place on the lattice site, as illustrated in Figure 1.3. This process may happen in a collinear or non-collinear fashion, each having a different probability.

The collinear interstitialcy mechanism dominates in AgCl and AgBr, and has been found to have exceptionally small migration barriers, as can be seen in Table 1.3. It has been proposed that the migrating cation undergoes quadrupolar deformation upon migration, substantially lowering the energy barrier.[13,66] Despite having a greater energy barrier due to steric restrictions, the non-collinear

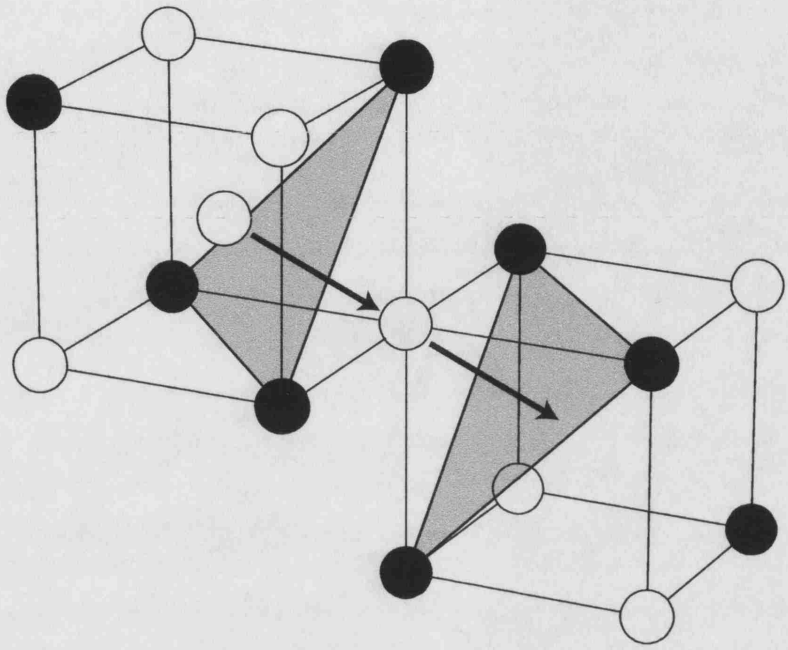

Figure 1.3: The collinear interstitialcy migration mechanism

interstitialcy migration path is also thought to occur.[64,67] The energy barriers in this case are also shown in Table 1.3.

Migration of the corresponding silver vacancy is thought to contribute significantly to cation transport. The process occurs via movement of a nearest neighbour cation into the vacancy, leaving behind an empty lattice site. Rather than migrate directly, which would involve an energetically unfavourable passage through the centre of a pair of halide ions, the cation is proposed to move via a pair of non-collinear jumps,[13,56,69] as can be seen in Figure 1.4. Again, the

Table 1.3: Experimental defect migration barriers / eV. *ci* represents the collinear interstitialcy mechanism; *nci*, the non-collinear mechanism; and *v* the vacancy migration.

	AgCl[68]	AgBr[57]
ΔE_{ci}	0.003	0.048
ΔE_{nci}	0.113	0.481
ΔE_{v}	0.278	0.297

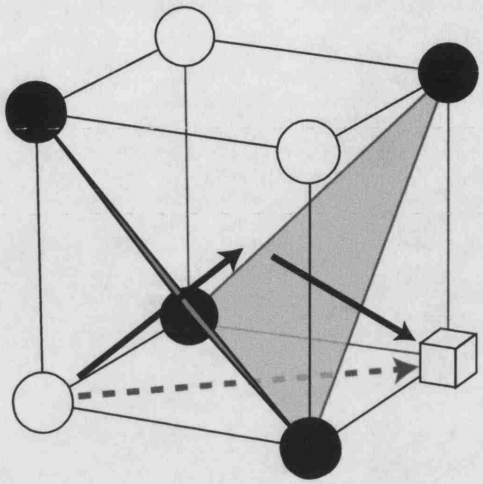

Figure 1.4: Illustration of the proposed vacancy migration mechanism. The dashed arrow corresponds to the energetically unfavourable direct route, while the solid arrows show the lower energy pathway.

experimental energy barriers are reproduced in Table 1.3.

There have been a number of attempts to model the migration behaviour. The earliest of these was by Hove in 1956[70] who used primitive interatomic potentials for AgCl to study the three mechanisms above. While his quantitative results are now believed to be unreliable, he observed the same ordering as reported in Table 1.3. More recent shell-model potentials have had greater success, reproducing the defect formation energies and their temperature dependence.[3,5] However, these failed in their application to defect migration unless an *ad hoc* description of the quadrupolar deformation of the migrating cation was introduced.[57,66]

Finally, it should be pointed out that recent experimental and theoretical work have shown strong evidence that the interstitial cation exists not at a cube-centre, but in a split-interstitial configuration involving a second cation.[60,61,71] Should this be confirmed, the above analysis would become invalid, as there would only be a single interstitial migration mechanism. However, this proposal is not inconsistent with experimental data; but accurate comparisons would require re-analysis of these results based on the new model.

1.1.6 Silver Halide Surfaces

The average size of a silver halide grain used in a photographic emulsion is around 1 μm. Hence the surface properties of the silver halides are relatively important, and have been studied extensively. Only the {100} and {111} faces are stable, and thus only grains of cubic and octahedral geometry are found naturally.[25]

Atomistic modelling of the non-polar (100) surface of AgBr suggests a very simple picture in which the ions have small displacements perpendicular to the surface, creating a 'rumpling' effect.[72] This model was later supported by surface extended x-ray absorption fine structure (SEXAFS) spectroscopy.[73]

The situation for the polar {111} surfaces is more complex, as they must reconstruct in order to reduce its surface dipole, which would result in a half-filled layer of either silver or halide ions. Hamilton and Brady's early electron diffraction experiments on AgBr resulted in a model consisting of top layer of silver ions, arranged in a hexagonal configuration,[74] which is in agreement with more recent AFM measurements,[75] but disagrees with both the atomistic modelling[72] and SEXAFS studies[73] which favour an alternate-row model. To our knowledge, this issue has not be resolved.

Just as in the bulk, defects are present at the surfaces of the crystal. A typical surface will be covered in flat terraces and atomic-scale islands laced with vacancies, adatoms, steps and kinks, as illustrated in Figure 1.5. These defects need not occur in neutral groupings. In fact, this latter behaviour will happen only at the isoelectric temperature where the free energies of formation will be identical. Indeed, it has been measured that the {100} surfaces have a space-charge layer consisting of a negatively charged surface and a charge-compensating subsurface concentration of interstitial silver cations.[72,76–78] The resulting spatial distribution of the defects within the space-charge layer has been derived by solution of the Poisson equation.[79–81]

The positively-charged surface kink sites are thought to play a key rôle in the formation of a space-charge layer due their low coordination, and therefore their low binding energy to the surface. As a result, they provide an efficient source of cations for redistribution into the bulk. The surface kink sites have been shown via simple symmetry arguments to have a charge of $\pm\frac{1}{2}e^-$, depending on its occupancy by a cation or an anion,[22] and are thought to be crucial to the photographic process (see Section 1.2).

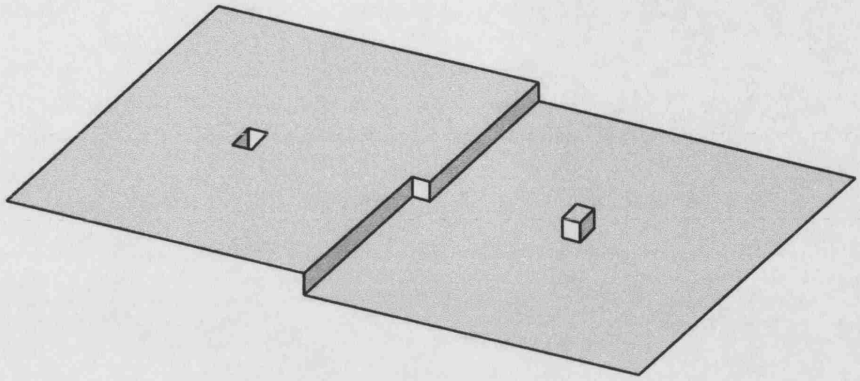

Figure 1.5: A simplified illustration showing various surface defects: a surface vacancy, a step, a kink, and an adatom.

The effects of the space-charge layer can cause the properties of small crystallites to deviate strongly from those measured in large macroscopic crystals. For instance, the defect concentrations are increased by two or more powers of ten, and migration barriers are lowered.[82] Indeed, the conductivity of AgBr has been measured to be proportional to the surface to volume ratio.[25] As will be described in the following section, these properties are highly beneficial to the photographic process.

1.2 The Photographic Process

A commercial photographic film consists of many micron-sized silver halide crystallites suspended in gelatin. These crystallites are generally composed of AgCl, AgBr or a solid solution of the two, sometimes with a small admixture of iodide.

When a film is exposed, certain grains will be exposed to light. Given enough photon flux on a given grain, a small silver cluster will form on its surface. This cluster, known as the photographic latent image, will catalyse the reduction of the whole grain to macroscopic metallic silver (along with halogen dimers) during the development process. These silver clusters represent dark specks on the resultant negative image.

The detailed mechanism behind the process of latent image formation has been the subject of much discussion over the past century. However a consensus has not yet been reached. The basic principles were first outlined by Gurney and

Mott in 1938,[83] but have evolved since then into the direct photolysis mechanism of today.[25,69]

1.2.1 Direct Photolysis

When a grain of silver halide is struck by light of great enough energy, an electron/hole pair is created. In the direct photolysis theory, the electron is vastly more mobile than the hole, which rapidly becomes trapped within the bulk of the crystal.[84] Owing to the absence of deep electron traps in the bulk of the material, the electron diffuses until it becomes trapped at a surface defect site, which happens within 10^{-8} seconds of exposure.[85] Due to its low coordination and partial positive charge, the positive kink is thought to be the most likely site for trapping (see Section 1.1.6). The electron is not thought to strongly localise, and will instead precess around the surface defect in a large orbit. However, it will alter the net charge of the site, and cause the surrounding ions to relax, deepening the trap. In simplified notation:

$$kink^{\frac{1}{2}+} + e^- \rightarrow kink^{\frac{1}{2}-}. \tag{1.1}$$

This negatively-charged centre will then draw the highly mobile interstitial cations from the subsurface space-charge layer towards the surface, whereupon one will be reduced to a neutral silver atom, regenerating the positive kink:

$$kink^{\frac{1}{2}-} + Ag_I^+ \rightarrow kink^{\frac{1}{2}+} + Ag(s). \tag{1.2}$$

This silver atom, known as the *latent pre-image centre*, is only metastable and may recombine with a free hole. However, due to its location on an anion lattice site, the silver atom is an efficient electron trap. Thus it may trap an additional electron, then interstitial, to form Ag_2, which is stable and is known as the *latent sub-image centre*.[25] This dimer does not catalyse the development process, but with repeated electron and interstitial trapping, a *latent image centre* is formed which is catalytically active. Depending upon the exact nature of film, this centre is composed of 3-5 atoms. The processes involved in the growth of these silver clusters have been modelled with increasingly accurate methods by Baetzold.[86–89] As a result, the geometries and electronic properties are now well understood, as are the dependencies on surface site.

The latent image centre acts as a catalyst for the reduction of the silver halide grain to silver during photographic development. In this way, the cluster size is effectively amplified by a factor of as much as 10^9, making it visible to the human eye.

1.2.2 Chemical Sensitisation

Despite the strict requirement of only 3-5 photons to form a developable cluster, the most sensitive emulsions usually require 6-10 photons, which is due to a number of factors:

- Dispersity (the formation of more than one latent image cluster per grain),
- Regression (the loss of a latent image cluster through reaction with mobile holes),
- Electron-hole recombination.

In order to improve efficiency, silver halides grains are often heated with aqueous solutions of gold and sulphur salts, resulting in chemisorbed Ag_2S and $AgAuS$ clusters.[69] These chemical sensitisers direct the formation of the latent image such that, in ideal cases, only a single latent image centre is formed, which is achieved by providing a preferential surface site for electron trapping, usually Ag_2S.[69,83] Gold atoms are usually also present, and are incorporated into the latent image cluster, improving the ability of small clusters to develop. Again, the calculations of Baetzold and co-workers have provided useful insights into these processes.[90,91]

An alternative, *reduction sensitisation*, involves partially reducing the grains in an emulsion such that a number of small silver clusters are formed on the surface. As they would not generally be located at a positive kink, their energy levels would not be compatible with the nucleation and growth mechanism described in the previous section. However, they act as hole traps, reducing the probability of recombination. Absorbed hydrogen gas is thought to play a rôle similar to that of reduction sensitisation centres, and has long been used by astronomers to improve the performance of their photographic detection plates.[92]

1.2.3 Spectral Sensitisation

The silver halides are intrinsically sensitive only to the UV and blue regions of the spectrum. For a realistic image in the visible spectrum, organic dye molecules are often employed. These molecules are electrically excited upon illumination by longer wavelengths, and will transfer their excited electrons into the conduction band of the crystal to which they are attached.[25,69,93] Colour photography thus involves a sophisticated layering of colour filters and colour-specific dyes.

1.2.4 Photo-Aggregation Theory

Mitchell's photo-aggregation theory, which has been offered as an alternative to the presently accepted direct photolysis mechanism described here, deserves comment.

While similar to direct photolysis, Mitchell argued that holes, rather than electrons, play the key rôle,[94,95] which came about as a result of experiments on large crystals which suggested that the positive holes are more mobile than interstitial cations. Thus, recombination should occur in preference to latent image formation. In addition, from these data, he calculated that there should be less than one interstitial defect per grain.

Instead, a hole would become trapped at negative kink site. The net positive charge on the kink would then repel a silver cation into a subsurface interstitial position, and leave behind a Br_2^- species. Due to the partial covalency of the silver halides, and their high dielectric constant, Mitchell argued that an electron would not become trapped at a positive kink site. However, the combination of the kink with a nearby subsurface interstitial cation provided the necessary conditions for electron trapping, which would then allow for the creation of a silver atom. The formation of a developable latent image cluster would then occur in a similar fashion to the direct photolysis theory.

The failing of this theory is that small crystallites have vastly different defect properties than large crystals due to the presence of the space-charge layer. Thus, subsurface interstitial cations will reach surface-trapped electrons rapidly. Consequently, the direct photolysis mechanism is widely accepted to be more realistic, and therefore has been the basis of most modern work.

1.3 Aims of This Work

As should be clear from this chapter, the silver halides have unique and interesting properties which make them ideal materials for the photographic process. However, not all aspects of the process are fully understood. Much work has been done on the industrially-important growth processes of the latent image cluster, and the effects of chemical and spectral sensitisers. However, some key quantities are not yet known.

The properties of bulk defects have not been studied since the early work, based on interatomic potentials, even though this method had clear deficiencies for the systems in question. State-of-the-art quantum mechanical calculations can now give more reliable structures and energetics, while also providing information on the electronic structure. Our primary aim is therefore to determine both the structural forms of the intrinsic defects in the bulk and at the surfaces, and the depth of hole and electron traps associated with these defects.

Much of the work regarding latent image formation has concentrated on the step-wise growth of the silver-atom clusters on the surface from Ag_1 to Ag_n. However, there has been relatively little work on the earlier stages of the process. As such, we also wish to understand the mechanism by which the first silver atom, the latent sub-image centre, is formed.

Chapter 2

Methodology

The methods used in this study are entirely computational. While the basic theories that underpin these methods have been known for decades, today's increased computing power has resulted in new applications. Therefore, we can now study larger systems in greater detail than has been possible before.

Along with this increased power have come advances in quantum chemical theory. Over the last 40 years, Density Functional Theory (DFT) has progressed to a state where it has become a primary tool for modelling crystalline materials.

In this chapter, the basic ideas behind semi-classical and DFT-based methods are outlined, followed by an introduction to the methods used to model defects in insulating materials.

2.1 Semi-Classical Modelling

The idea behind semi-classical calculations is to remove all the quantum-mechanical detail from short-range ion-ion interaction, and replace it with a simple function, known as the interatomic potential. With a set of parameters describing the interaction between all pairs (and, optionally, triplets and quartets) of ions in a crystal, remarkably accurate properties can be calculated at relatively little computational expense. In this section, the basic concepts behind these methods are outlined. For a more complete description, the reader is directed to the volume edited by Catlow and Mackrodt,[96] or the recent paper by Gale and Rohl.[97]

2.1.1 Ion-Pair Interaction

In ionic crystals, the interatomic potential can be described as the sum of a Coulombic contribution, a short-ranged repulsive term and an attractive van der Waals term. The Coulombic term, given simply by Coulomb's law (Equation 2.1), will provide the dominant contribution to the total energy: typically around 90%.

$$U(r_{ij}) = \frac{q_i q_j}{r_{ij}} \tag{2.1}$$

where $q_{i,j}$ are the ionic charges, r_{ij} is the interatomic separation, and all quantities are in atomic units.

Although simple in form, in practice these terms are difficult to calculate as they form a conditionally convergent series. As a result, special techniques and conditions must be employed to transform the sum into a convergent series. The most widely used example for bulk crystals is the Ewald sum,[98] which imposes conditions of charge neutrality and zero dipole moment, then splits the sum into two terms: one rapidly convergent in real space, and one rapidly convergent in reciprocal space. As will be described later, there are also methods which allow these two conditions to be broken.[99,100]

In order to model a thermodynamically stable crystal, repulsive terms are required. These result from the Pauli exclusion principle, and along with the dispersive attraction, provide much of the chemical character of the material. These contributions are usually combined into a single term, usually of the form described by Buckingham, which is shown in Equation 2.2, and illustrated in Figure 2.1.

$$U(r_{ij}) = A\exp(-r_{ij}/\rho) - C/r_{ij}^6 \tag{2.2}$$

where A, ρ and C are constants, fitted to either quantum mechanical or experimental data.

The first term in the equation describes the overlap repulsion. The functional form of this interaction will be complicated, and involve knowledge of the electronic structure of each atom. In practice, it is replaced by a simple exponential term which reflects the radial dependence of a 1s-orbital. In an alternative form, described by Lennard-Jones, the repulsion is represented by an r^{-12} term.[101]

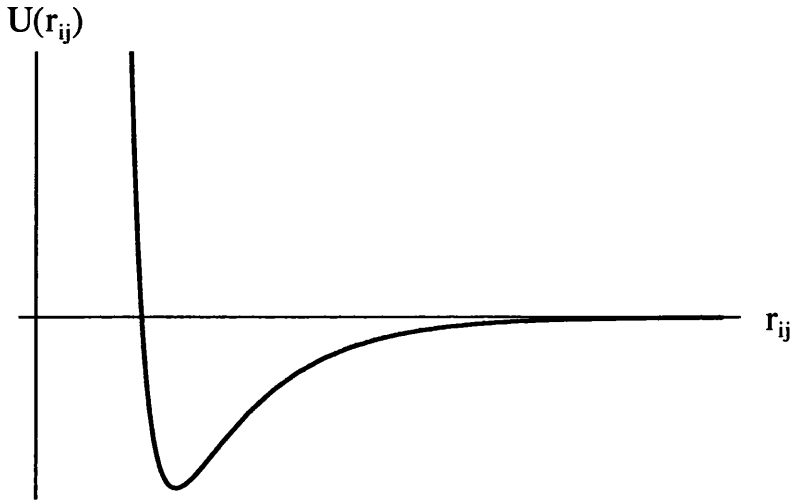

Figure 2.1: Plot of a standard Buckingham potential (Equation 2.2).

While more mathematically efficient, this has been shown to be inferior to the Buckingham form for most ionic materials.

The second term describes the attractive short-range dispersion, or van der Waals, force, which is due to the interaction of two dipoles produced through random fluctuations of two polarizable ions. It is quantum mechanical in origin, and the leading term has been shown to take the r^{-6} form shown here. Higher-order terms from other fluctuating multipoles are generally unnecessary, but have the forms r^{-8}, r^{-10} and higher.

2.1.2 Many-Body Interaction Terms

In many materials the bulk properties cannot be reproduced accurately using simple two-body interactions. A measure of the importance of many-body interactions in a material is the degree to which the Cauchy condition is violated. Cauchy stated that, for centrosymmetric cubic crystals at equilibrium, the elastic constants must satisfy the condition $C_{12} = C_{44}$. Deviations are small in materials such as the alkali halides, but are large in the silver halides (where $C_{12} \approx 5C_{44}$).

Three-body interactions arise from two different effects. First, due to the form of the underlying molecular orbitals, a triplet of ions may have a preferred internal angle. Thus, a term can be introduced which penalises deviation from

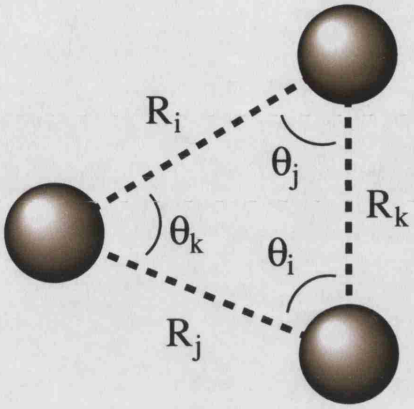

Figure 2.2: Definition of the bond lengths and angles in Equation 2.4.

this angle, which would be of the form:

$$U(\theta) \sim (\theta - \theta_0)^2 \tag{2.3}$$

where θ is the actual angle of the triplet, and θ_0 is the 'preferred' angle.

The other form, used in ionic materials without directional bonding, is the three-centre dispersion relation (i.e. the three-body equivalent of the van der Waals interaction). This term was derived by Axilrod and Teller,[102] and takes the form:

$$U(R_i, R_j, R_k) = C_{ijk} \frac{1 + 3\cos\theta_i \cos\theta_j \cos\theta_k}{R_i^3 R_j^3 R_k^3} \tag{2.4}$$

where the R's and θ's are interatomic separations and angles, as shown in Figure 2.2, and C_{ijk} is a constant. This form has been used by Baetzold *et al.* to model the defect properties of the silver halides with some success.[5]

Four-body interactions are often required to model the dependence upon torsional angles of molecular species. Similarly, they can be used when modelling planar species, such as the carbonate anion, in order to reproduce the out-of-plane bending mode.[103]

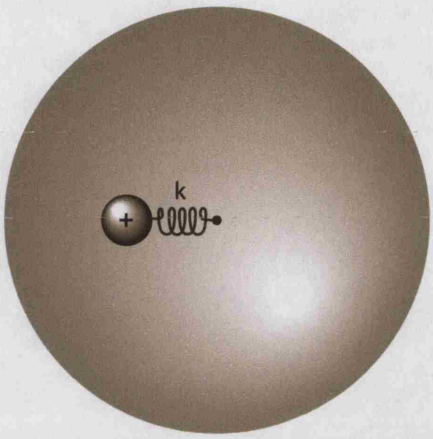

Figure 2.3: Illustration of the 'shell model' of Dick and Overhauser.[104] The small sphere represents the core, which contains the nucleus and the core electrons. The larger sphere, which is negatively charged, represents the remaining valence electron(s). The two are connected via a spring of spring constant k.

2.1.3 Polarizability

Normally in binary ionic materials such as the halides and oxides, the anion will be highly polarizable. In some cases, such as the silver halides, the cation will also have an appreciable polarizability. In materials such as these, the simple monopole-monopole Coulomb term must be supplemented with terms involving dipoles and possibly quadrupoles.

The effects of dipole polarizability are commonly introduced using the simple mechanical *shell model* of Dick and Overhauser,[104] which decomposes the atom into two parts: the outer valence electrons (the shell), and the inner core containing the nucleus and all core electrons (known simply as the core). The core and the shell are both charged, but do not interact Coulombically. However, their positions are coupled via an harmonic spring, as illustrated in Figure 2.3.

Use of this model has lead to accurate descriptions of the dielectric, phonon and defect properties of many ionic materials.[105–109] Some materials, such as the silver halides, require quadrupolar-interaction terms.[12,14,110] The shell model cannot easily be extended to include these interactions, and thus alternative techniques must be used.

One alternative, is to assign each point ion a dipole and quadrupole polariz-

ability. The contributions to the energy from the dipole and quadrupole can then be calculated as a function of the electric field at that point in space.[110–112] The primary disadvantages of this seemingly superior method are that the polarizabilities are independent of their chemical environment, and also that the calculations require self-consistent optimisation, as the electric field on one centre will depend upon the induced multipoles on the surrounding ions.

2.1.4 Calculation of Crystal Structure and Properties

Given a particular crystal structure and a full set of interatomic potentials for the constituent ions, the total lattice energy of the system, U, may be calculated. The derivatives of this energy with respect to various quantities can provide a wealth of data about the properties of the crystal.

The first and second derivatives with respect to atomic positions are used directly in structural optimisation calculations. Many algorithms have been developed which aim to find the global minimum, and hence the most stable structure, in an efficient and accurate way. Knowledge of the matrix of second derivatives, known as the Hessian, is highly beneficial, as it can be used to calculate directly the position of the local minimum of a quadratic surface. However, in realistic systems, repeated calculation of the inverse Hessian is required, which can be an expensive process - especially for larger systems. Algorithms known as DFP[113] and BFGS[114] have been designed which update, rather than re-calculate, the inverse Hessian after each step. These have been shown to be extremely efficient, and have been widely implemented.

For a system at equilibrium geometry, the Hessian can also tell us about phonons in the crystal. The dynamical matrix, $\mathbf{D}(\mathbf{k})$, can be calculated from the sum of these derivatives multiplied by a reciprocal-space dependent phase factor. The frequencies can then be obtained from the eigenvalues of the equation:

$$\mathbf{D}(\mathbf{k})\mathbf{u} = \sqrt{M_i M_j}\omega^2\mathbf{u}. \tag{2.5}$$

where $M_{i,j}$ are the masses of the ions (assuming a two-ion basis), ω is the angular frequency, and $\mathbf{u}$ are the eigenvectors corresponding to the vibrational modes.

A plot of the resultant frequencies against position in the Brillouin zone, $\mathbf{k}$, gives the phonon dispersion curves of the crystal.

The elastic properties of the material can also be calculated in a similar fash-

ion. The elastic constants can be determined via the second derivatives of the energy with respect to strain (ϵ):

$$C_{ij} = \frac{1}{V}\left(\frac{\partial^2 U}{\partial \epsilon_i \epsilon_j}\right) \tag{2.6}$$

where V is the volume of the unit cell, and the values form a 6 x 6 symmetric tensor.

Within the symmetry of the crystal the number of independent matrix elements is reduced. For a cubic material, such as silver chloride, the only unique elements are C_{11}, C_{12} and C_{44}. Given these quantities, other elastic data such as the bulk and shear moduli can be approximated using simple relations.[97]

The dielectric constants may also be routinely calculated. Two extreme values are usually quoted, corresponding to the application of static and high frequency electric fields. Each form a 3 x 3 tensor with coefficients calculated according to:

$$\varepsilon^0_{\alpha\beta} = \delta_{\alpha\beta} + \frac{4\pi}{V}(\mathbf{q}\mathbf{D}^{-1}_{\alpha\beta}\mathbf{q}) \tag{2.7}$$

where α, β correspond to Cartesian directions, $\mathbf{q}$ is the vector containing the charges of all particles, and $\mathbf{D}_{\alpha\beta}$ is the second derivative matrix.

The two quantities differ due to the nature of the polarization. For the high frequency case, only the electrons can adapt to the changing field, and so D and q contain values for the shells only. For static fields, the nuclei have time to relax, and thus both the cores and shells appear in the expression and the dielectric screening is much greater.

The results of our calculations employing these semi-classical techniques are reported in Chapter 3.

2.2 Density Functional Theory

2.2.1 Introduction

Density Functional Theory puts the ground-state electron density at the heart of electronic structure calculations. The origins of the method are in the Thomas-Fermi model, which approximated the kinetic energy of the electrons as a functional of their density, while neglecting exchange and correlation interactions.[115,116] However, these approximations result in a method that is not accurate enough

for most practical applications.

In 1964, Hohenberg and Kohn published a landmark paper proving that if the electron density of a system is known, the external potential, $V_{ext}(\mathbf{r})$, can in principle be uniquely determined.[117] Given this potential, the full Hamiltonian is known, and any other property of that system may be calculated. In addition, they stated that a universal functional for the energy in terms of the density can be defined for any given potential. The global minimum value of this functional is equal to the ground-state energy, while the corresponding density is also that of the ground-state (Equation 2.8).

$$E_{HK}[n] = T[n] + E_{int}[n] + \int d^3r V_{ext}(\mathbf{r})n(\mathbf{r}) + E_{II} \tag{2.8}$$

where n is the electron density, $T[n]$ and $E_{int}[n]$ are the kinetic and internal energy functionals, $V_{ext}(\mathbf{r})$ is the external potential described above, and E_{II} is the interaction energy of the nuclei.

Unfortunately, the theorem could provide no information about the functionals involved. In fact, these unknown functionals will in general have complex non-local forms. As a result, the Hohenberg-Kohn theorems are of limited direct applicability.

However, in 1965, Kohn and Sham published a method which brought practical applicability to Hohenberg and Kohn's theory through the use of some additional approximations.[118] They re-expressed the many-body form of the Hohenberg-Kohn theorem (Equation 2.8) in a single-particle form:

$$E_{KS}[n] = T[n] + \int d^3r V_{ext}(\mathbf{r})n(\mathbf{r}) + E_{Hartree}[n] + E_{II} + E_{xc}[n] \tag{2.9}$$

where $T[n]$ is now the independent-particle kinetic energy, $E_{Hartree}[n]$ is the self-interaction energy of the density, and $E_{xc}[n]$ contains all the (unknown) many-body exchange and correlation effects.

Key to the theory is the assumption that the *exact* many-body ground state density can be represented using the independent particle densities. Thus the advantage of this approach is that if the exchange-correlation functional $E_{xc}[n]$ is known, the ground state energy and density of the many-body system can be determined.

In practice, $E_{xc}[n]$ is unknown, but by the Kohn-Sham construction, it can

be approximated as a local or semi-local functional. There is currently an active research area trying to find the best approximations to this complex functional. This work is summarised in the following section.

2.2.2 Exchange-Correlation Functionals

Local Density Approximation

The Local Density Approximation (LDA), originally formulated by Kohn and Sham,[118] was the first example of an exchange-correlation functional. It was proposed that the exchange-correlation energy could be approximated as an integral over all space, with the energy density at each point assumed to be the same as in a homogeneous electron gas with that density. This is reasonable for materials such as metals, which can be considered to be close to the limit of the homogeneous electron gas.

Generalised-Gradient Approximations

For materials which have a greater degree of variation in their electron density distribution, the inclusion of extra terms dependent on the magnitude of the density gradient, $|\nabla n|$, generally provides a more accurate representation of the exchange-correlation functional.[119] As a result, the overbinding found in LDA calculations is reduced, and bond lengths are increased.

Common examples of these Generalised-Gradient Approximation (GGA) functionals include B88,[120] PW91[121] and PBE.[122] Due to the additional complexity, calculations using these functionals take approximately 50% longer than those using the LDA.

Hybrid Functionals

The idea behind hybrid functionals is to empirically combine the strengths of DFT with those of the Hartree-Fock approach. This is reasonable, as the two methods often have opposing characteristics: HF underbinds while DFT overbinds; HF overestimates and DFT underestimates band gaps.

Simply mixing Hartree-Fock's exact exchange into the DFT exchange-correlation functional as a linear combination has provided some of the most accurate functionals available today. A simple example is given in Equation 2.10, where α is a

fraction fitted to experimental data.

$$E_{xc} = \underbrace{\alpha E_x^{HF} + (1-\alpha)E_x^{LDA}}_{\text{Exchange Terms}} + \underbrace{E_c^{LDA}}_{\text{Correlation Term}} \tag{2.10}$$

This method can, and usually is, extended to use GGA DFT. One of the most common hybrid functionals, B3LYP, uses Hartree Fock and Becke's B88 functional for exchange along with LYP correlation.[123]

Also of note due its relevance to this work, is the systematic optimisation procedure also by Becke.[124] In this method, the exchange and correlation functionals were expanded in a power series involving the density and its first derivative. To this, a fraction of exact exchange was added. The resultant 10 parameter form was fitted non-self-consistently to the G2 set of atomic and molecular energy data,[125] and provided very accurate results. Later, Hamprecht *et al.* re-parameterised the B97 functional using a self-consistent procedure, resulting in the B97-1 functional.[126] More recently the B97 functional form has been used again, with parameters fitted to thermochemical data and the exchange-correlation *potentials*, obtained using the method of Zhao *et al.*[127] This resulted in the B97-2 functional,[128] which represents a significant improvement over the B97, B97-1 and the B3LYP functionals. The B97-2 functional has been used extensively in the QM/MM work reported in Chapter 5.

2.3 Basis Sets

In all practical applications of DFT, and in electronic structure calculations in general, a basis set must be introduced with which to represent the electron density, usually comprising analytical functions of a particular form, typically gaussian functions or plane waves. If this set were mathematically complete the accuracy of the calculation would be unaffected by its choice. However, in reality, this infinite set of functions must be truncated, and as a result accuracy is lost. The computational effort of a calculation scales with the number of basis functions, and so a balance between accuracy and efficiency must be found.

In order to maximise the quality of a finite basis set, it should represent the underlying structure of the material. Two of the most common methods are described in the following sections.

2.3.1 Atom-Centred Basis

In this basis set, functions are placed where they are needed: around each atom. The most commonly used variant are the Gaussian Type Orbitals (GTO) which have the form:

$$\chi_{\zeta,n,l,m}(r,\theta,\varphi) = NY_{l,m}(\theta,\varphi)r^{(2n-2-l)}e^{-\zeta r^2} \tag{2.11}$$

where N is a normalisation constant, $Y_{l,m}$ are spherical harmonics and ζ controls the width of the orbital.

These have the disadvantage that they do not have the same behaviour as real atomic orbitals, and therefore a linear combination of many such functions must be used in order to reproduce the required forms. Their widespread use therefore relates to the great efficiency with which they can be manipulated mathematically.

The size of a GTO basis set is classified according to a standard notation. A minimum basis set, which has only enough functions to contain the electrons of the neutral atom, is known as *single zeta* (SZ). Basis sets with double and triple this number of functions are called *double zeta* (DZ) and *triple zeta* (TZ) respectively. As the atoms become heavier, often only the active outer valence electrons are treated at this level, and the basis sets are therefore termed DZV and TZV. Furthermore, extra polarization functions may be added with higher angular momentum, which allow for lower symmetries in the density, leading to DZVP and TZVP quality basis sets. The latter are used for all calculations in Chapter 5.

As long as the basis set remains incomplete there will be large systematic errors in the computed energies. Relative energies, however, are far more accurate due to error cancellation. This rule breaks down when differing geometries are compared, as the quality of the basis set is not consistent. For example, when the two constituent atoms of a dimer move closer together the description of one ion becomes improved due to the proximity of the basis functions on the other. The result is a lowering in energy of the bound system, and an overbound dimer. This effect is known as basis set superposition error (BSSE), and must always be considered in calculations of this type.

2.3.2 Plane Wave Basis

Rather than have a basis set based upon the positions of the nuclei, which allows for calculations in any periodicity (e.g. gas phase, condensed matter), the plane wave basis set is restricted to the three dimensional periodicity of the crystal unit cell. This means that Bloch's theorem can always be applied, resulting in an electronic wavefunction of the form:

$$\psi_{i,\mathbf{k}}(\mathbf{r}) = u_{i,\mathbf{k}}(\mathbf{r})e^{i\mathbf{k}.\mathbf{r}}, \tag{2.12}$$

where $u_{i,\mathbf{k}}(r)$ has the periodicity of the cell.

This is, of course, true for condensed phase atom-centred basis calculations, in which $u_{i,\mathbf{k}}(\mathbf{r})$ will be a complicated periodic function involving the positions of the nuclei. For the case of the plane wave basis set, $u_{i,\mathbf{k}}(\mathbf{r})$ is simply taken to be a plane wave expansion:

$$u_{i,\mathbf{k}}(\mathbf{r}) = \sum_{\mathbf{G}} c_{i,\mathbf{G}} e^{i\mathbf{G}.\mathbf{r}}, \tag{2.13}$$

where $\mathbf{G}$ are the reciprocal lattice vectors.

Therefore, the single-electron wavefunction can be written as a sum of plane waves:

$$\psi_{i,\mathbf{k}}(\mathbf{r}) = \sum_{\mathbf{G}} c_{i,\mathbf{k}+\mathbf{G}} e^{i(\mathbf{k}+\mathbf{G}).\mathbf{r}}. \tag{2.14}$$

Again, this basis set must be truncated. One of the great advantages of this method is that a single parameter controls the quality of the basis set. This parameter is known as the cut-off energy, and corresponds to the kinetic energy of the largest wavevector in the plane wave basis:

$$E_{cut} = \frac{\hbar^2}{2m}(\mathbf{k}+\mathbf{G})^2 \tag{2.15}$$

All plane waves of kinetic energy below this value are included in the expansion.

Other advantages are: the basis set treats all space equally, without any bias towards atomic positions, eliminating BSSE; they are mathematically very simple, improving efficiency; and they are potentially mathematically complete. The main disadvantage of their use is that a very large number of plane waves,

often millions, are required in order to achieve chemical accuracy.

2.4 Pseudopotentials

When dealing with heavy atoms, the number of required basis functions can be very large. Fortunately, the innermost core electrons can be considered inactive, and therefore chemically unimportant. The idea behind the pseudopotential approach is to replace the Coulomb potential of the nucleus and the effects of these core electrons by an effective potential which acts upon only the valence electrons. The resultant decrease in required basis set size increases the efficiency of the calculations without a loss of accuracy. In fact, accuracy can often be *improved* by incorporating relativistic effects into the pseudopotential which would not normally be accounted for.

Key to the pseudopotential approach is the transferability of the potential. The conditions for a 'good' pseudopotential were laid out by Hamann, Schluter and Chiang:[129]

- The all-electron and pseudo valence eigenvalues should agree,
- The all-electron and pseudo valence wavefunctions should agree outside a chosen core radius,
- The logarithmic derivatives of the all-electron and pseudo valence wavefunctions should agree at the core radius,
- The first energy derivative of the logarithmic derivatives of both wavefunctions should agree at the core radius,
- The integrated charge within the core regions should agree.

When all of these conditions are met, the resultant pseudopotentials are termed norm-conserving, and have proved to be very accurate and transferable. However, when used with plane wave basis sets, high cut-off energies are usually required, resulting in expensive calculations.

It has since been determined that the norm-conservation condition can be relaxed, leading to smoother potentials, if an auxiliary function is added to deal with the rapidly varying electron density around each ion's core. This approach,

resulting in *ultrasoft pseudopotentials*, has greatly increased the efficiency of today's calculations, and has been used for all calculations in Chapter 4.

2.5 Brillouin Zone Sampling

When imposing periodic boundary conditions upon a system, the number of electrons becomes a finite, manageable quantity. However, the wavefunction and density become artificially limited to the periodicity of the chosen cell. As can be seen in Bloch's equation (Equation 2.12), this is compensated by the introduction of reciprocal space-dependent exponential term, which may introduce long wavelength oscillations into the wavefunction.

These reciprocal space vectors, or k-points, all exist within (or can be mapped back into) the first Brillouin zone of the crystal. At each k-point, the eigenvalues of the Hamiltonian will form a series of discrete energy levels. These levels will generally vary smoothly between neighbouring k-points, and will thus form bands of energy levels, an example of which can be seen later in Figure 4.3.

In order to reproduce all the long-range effects in the infinite crystal, the set of k-points should be in principle be infinite. However, this set can be reduced significantly to a small subset of representative points by exploiting the smoothness of the calculated properties with small changes in k-space. The resulting subset can often be further reduced by the use of symmetry. Early studies in the literature have achieved reasonable accuracy using simple gamma-point calculations, in which the phase-factor in Equation 2.12 is removed ($\mathbf{k} = (0, 0, 0)$). However, modern calculations must use a representative sample of k-points if chemical accuracy is to be achieved.

2.6 Point Defect Calculations

Calculations of defect properties have been performed for over 40 years, starting with simple classical models,[107,130] and lately applying high level quantum mechanical techniques.[131,132] Several techniques have been devised for studying defects computationally. These can be placed into two broad categories:

- those that exploit the symmetry of, and the methodologies developed for, the host crystal,

- those that treat the defect and its immediate surroundings as an isolated cluster, employing the methodologies developed for molecular systems.

In the following sections both approaches will be described.

2.6.1 Supercell Methods

The simple idea behind the supercell method is to place a defect into a cell that is larger than the primitive unit cell, as depicted in Figure 2.4. This can be used as a direct method with which to study defects at high concentrations, but as concentration decreases, supercell size must increase. However, as the computing resources required for such a calculation will increase with the number of atoms in the system, clearly the limits will be reached quickly.

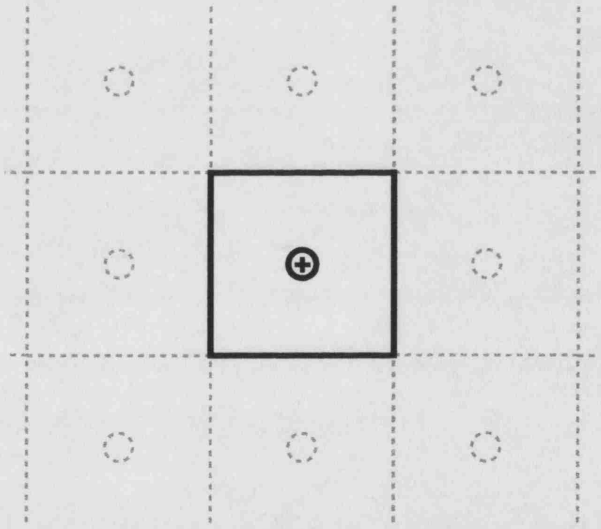

Figure 2.4: Illustration showing the supercell technique

Given that defects are normally present in small concentrations, it is useful to adapt these methods in order to approximate a state of infinite dilution. For the simple case of neutral defects, the interaction between a defect and its periodic images will be minimal*. Given a supercell large enough to encompass any

*This only strictly true of defects with no multipole moments whatsoever.

structural relaxations, an accurate defect formation energy can be obtained by using a sufficiently dense k-point grid.

The situation is more complicated with charged defects. In this case, an infinite array of charged supercells results in a divergent Coulomb sum. This problem can be circumvented using a neutralising background charge, which hopefully will not alter the structural properties of the defect nor energy differences between two similar cells.

For the case of a homogeneous jellium background charge, the error in using this approach can be corrected for *a posteriori* using the term derived by Leslie and Gillan.[99] A further term due to the quadrupole moment of the defective system has also been derived,[100] leading to the correction formula for systems with no net dipole moment:

$$E_{corr}(L,q) = E_0 + \frac{\alpha q^2}{2\varepsilon L} + \frac{2\pi qQ}{3\varepsilon L^3} + O[L^{-5}] \tag{2.16}$$

The second term simply amounts to the energy of a system of periodic charges in a uniform background charge, where q is the defect charge and α is the appropriate Madelung constant for this model system. The third term describes the jellium-quadrupole interaction, where Q is the quadrupole moment. Each term is reduced by the dielectric constant, ε, to simulate the effects of the polarizable crystalline lattice. Clearly, this approximation is only exact in the limit of infinite supercell size.

Correcting the defect energetics with these terms has been shown to drastically improve the convergence with respect to supercell size (see Section 4.1.5). The individual defect formation energies can then be calculated according to:

$$E_f(q) = E_{def} - E_{pure} - n_M\mu_M - n_X\mu_X + q\mu_e + E_{corr}(q), \tag{2.17}$$

where E_{def} is the energy of the defective cell, E_{pure} is the energy of the defect-free reference system, $n_{M/X}$ are the change in number of cations/anions on going from the pure cell to the defective system, $\mu_{M/X}$ are the cation/anion chemical potentials relative to their standard states, q is the net cell charge, μ_e is the chemical potential of the electron and E_{corr} is the correction described above (Equation 2.16).

The chemical potential of the electron, μ_e, or equivalently the Fermi energy, is undefined in a perfect insulator,[133] and hence calculation of charged defect

formation energies is problematic. For uncharged defects, however, the chemical potentials can routinely be calculated relative to their standard states.

When calculating the full reaction cycle (i.e. the formation of a pair of charge-compensating defects) two such equations are combined. For the cases of the cation Frenkel and Schottky defects, the resulting equations are:

$$\Delta E_{Frenkel} = E_{def}(M_I) + E_{def}(V_M) - 2E_{pure} + E_{corr}(M_I) + E_{corr}(V_M), \quad (2.18)$$

$$\Delta E_{Schottky} = E_{def}(V_M) + E_{def}(V_X) - \left(2 - \frac{1}{N}\right) E_{pure} + E_{corr}(V_M) + E_{corr}(V_X), \quad (2.19)$$

where N is the number of MX formula units in the pure cell, and all other terms are as described above.

For the Schottky pair, it is assumed the removed ions combine and add to the bulk material, and hence the sum of their chemical potentials can be replaced with the energy of a pair of ions in the bulk. The dependence upon the electron chemical potential is cancelled, and thus calculation of these energies is tractable regardless of charge state.

The calculation of energies in insulating materials are complicated by the lack of a consistent reference energy. In some calculations, energies may be referenced to the valence band maximum, however in general this is hard to implement in a consistent fashion. Insertion of a defect into the band gap, or alteration of the defect's charge state, may also affect this reference energy. One method of correcting for this behaviour is to compare the electrostatic potential at a distance from the defect with that of the pure bulk material.[134] Alternatively, comparison of the energies of unaltered semi-core states in the band structures may suffice.[135]

2.6.2 Cluster-based Methods

In cluster-based methods, a fragment around the site of interest is excised from the crystal and is treated as a large 'molecule'. This approach has the advantage of utilising standard quantum-mechanical molecular codes such as GAMESS-UK[136] and GAUSSIAN,[137] which can often provide greater flexibility than codes which implement periodic boundary conditions. For instance, while post-Hartree

Fock and time-dependent DFT methods are readily available in many molecular codes, they are rarely implemented in those designed to model the solid-state. As a result, calculations of excited states can routinely be performed using cluster-based techniques.

There are, however, drawbacks to this method:

- The cluster must be large enough to contain the major structural relaxations around a defect, which can lead to large, costly, calculations.
- The electrostatic potential within the cluster will be missing all the long-range electrostatic contributions from the removed crystalline lattice, resulting in incorrect positioning of the energy levels.
- A defect within the cluster will interact with the artificially-imposed surface. The under-coordinated surface species will be more polarizable than in the bulk and hence the electronic polarization due to the defect will be overestimated and the electronic structure may well be wrong.

Various schemes have been developed to improve the accuracy and efficiency of this technique. Most are based upon the idea of embedding the cluster within a representation of the infinite crystal lattice. In the literature, this has been achieved using techniques which fall into two broad categories: those codes which employ semi-classical ions and/or point charges to reproduce the effects of the infinite crystal, such as ICECAP,[138,139] ChemShell,[140] and GUESS;[141] and those codes which use the results of *ab initio* periodic calculations to represent the extended crystal, such as EMBED[142] and the method of Carter *et al.*[143]

We have employed the former approach, termed QM/MM embedding, for the work in this thesis. One of the most important factors affecting the accuracy of this technique is the quality of the coupling between the QM and MM regions. The various levels of sophistication have previously been characterised by Bakowles and Thiel:[144]

Mechanical Embedding The QM cluster is relaxed in a gas-phase calculation. The nuclei from this calculation appear as point charges in a separate MM calculation.

Electrostatic Embedding The MM nuclei are explicitly included in the QM Hamiltonian as point charges.

Polarized Embedding As electrostatic embedding, but the shell-model ions' polarizability is coupled to the QM charge density.

We have used a self-consistent polarized embedding model in which the QM and shell-model MM polarizations are brought to equilibrium using an iterative technique at each step of the geometry optimisation.

At the interface between the QM and MM regions, special techniques are required to reduce the unphysical effects of this artificial boundary. For covalent materials, this can be a complex task, as each broken bond must be terminated, usually by hydrogen atoms. The total energy expression must then be altered to remove the contributions from these centres. For ionic materials, such as those studied here, the situation is far more simple, with a region being defined which has a degree of quantum character, but is also modelled using interatomic potentials. Further details of our method will be described in Chapter 5.

It is important to note that for practical reasons we must impose a limit on the number of ions that are free to relax in our system. This number can be rather large, and will easily encompass any structural relaxations in our system. However, we cannot model the long-ranged effects of polarization, which are very important when modelling charged systems. Using the equation of Jost[145] we can however, include this contribution to the total energy *a posteriori*:

$$E_{bulk}^{polar} = -\frac{q^2}{2R}\left(1 - \frac{1}{\varepsilon}\right) \tag{2.20}$$

where q is the charge of the system, R is the cut-off radius after which we do not relax our ions, and ε is the dielectric constant of the material.

This equation has been generalised by Sokol for surface calculations, as performed here:[146]

$$E_{surface}^{polar} = -\frac{q^2}{2R}\frac{\varepsilon - 1}{\varepsilon + 1} \tag{2.21}$$

These correction terms cannot be neglected as they have been shown to stabilise charged systems by around 0.5eV for singly charged systems within a typical embedding scenario. Due to the q^2 dependence in the equations, this will rise rapidly for higher charge states.

The methods described here, although complex, have been shown to produce accurate surface defect formation energies for ZnO[146] and MgO.[147] We have used this technique extensively to study silver chloride, as reported in Chapter 5.

Chapter 3

Semi-Classical Calculations

As described in Chapter 2, semi-classical methods provide a very efficient way of obtaining information about closed-shell systems. When a reliable, transferable, model of the interactions has been derived it can be used to study either very large systems or very long time-scale dynamics, leading to a more comprehensive picture of the properties of the crystal.

In this chapter, previous work has been re-examined to investigate the applicability of existing interatomic potentials to modern simulations of the silver halides. We have then derived a new set of potentials which have been optimised for use in our QM/MM calculations reported in Chapter 5.

3.1 Method

Two programs were used for this work: GULP (General Utility Lattice Program),[97,148] and MARVIN'S Program (Minimisation and Relaxation of Vacancies and Interstitials for Neutral Surfaces).[149] Both employ the standard techniques described in Section 2.1, including the use of the shell-model to model dipole polarization. While GULP is the more versatile code, until very recently it did not include the ability to impose two-dimensional periodic boundary conditions required for surface calculations, and thus MARVINS was utilised for this work.

While the general features of the semi-classical method have already been discussed, in this chapter it will be necessary to introduce some additional functional forms, particularly for our three-body interactions. For the sake of clarity, they will be described as they arise.

3.2 Assessment of Existing Potentials

Although a number of authors have reported interatomic potentials for the silver halides,[3,5,7,8,150,151] only a few have been applied to the calculation of defect properties,[3–5,57,66] the primary purpose of this work.

In order to find a robust set of interatomic potentials for use here, we have applied each of the sets to the calculation of key properties, and as a result, we have reassessed the quality of each in the modern context. Although there are other older sets, they have not been studied here as they all have known deficiencies.[70,150] Furthermore, potentials using the polarizable point-ion model described in Section 2.1 have not been investigated,[7,110,151] as this approach is known to have serious deficiencies.

3.2.1 Potentials of Catlow *et al.*

The simple two-body potentials of Catlow *et al.* were the first set of potentials to reproduce key defect properties of AgCl accurately.[3] As can be seen in Table 3.1, they have larger van der Waals coefficients than would be expected on the basis of ion polarizability. However, it has been proposed that this effect is due to the partial-covalency of the silver halide bonds. By modern standards these are primitive potentials, as they act upon nearest-neighbours only. However, they have been widely applied and have been shown to be consistent with experiment in a number of cases.[72] Due to their two-body nature, they fail to model the Cauchy violation in the elastic constants, and are thus unsuitable for general application.

Table 3.1: The two-body shell-model interaction potentials for AgCl of Catlow *et al.*,[3] which are of the Buckingham form (Equation 2.2). The shell charges and spring constants are: Q_{Ag}=-9.4826|e|, Q_{Cl}=-2.485|e|, k_{Ag}=597.69 eVÅ^{-2} and k_{Cl}=29.38 eVÅ^{-2}. All interactions are nearest-neighbour only.

	Ag-Ag	Ag-Cl	Cl-Cl
A/eV	16528.0	2518.8	1227.2
ρ/Å	0.2370	0.3272	0.3214
C_{ij}/eVÅ^6	224.0	219.52	75.00

It should be noted that the techniques used to derive these potentials were

used to obtain similar quality potentials for AgBr.[4] These potentials are not discussed here as our primary interest lies with AgCl. However, they suffer the same limitations as the potentials described above.

3.2.2 Potentials of Baetzold *et al.*

These potentials are a product of the same group as the previous set, but employ three-body potentials in an attempt to improve the description of the bulk and defect properties.[5] The Axilrod-Teller coefficients reported in the original publication were incorrectly scaled to compensate for over-counting.[152] The corrected potentials are reported in Tables 3.2 and 3.3. While the resultant elastic and dielectric properties are in good agreement with experiment, the phonon dispersion curves are inconsistent with the data from neutron scattering.[10] However, this would be expected due to the lack of quadrupolar terms (see Section 1.1.2).

Table 3.2: The three-body interatomic potentials of Baetzold *et al.* for AgCl.[5] The shell charges and spring constants are: Q_{Ag}=-19.396|e|, Q_{Cl}=-2.485|e|, k_{Ag}=4500.0 eVÅ^{-2} and k_{Cl}=29.38 eVÅ^{-2}. The corrected values of the Axilrod-Teller coefficients, C_{ijk}, are reported here. The two- and three-body cut-offs are 2.5a, and 5.5Å respectively, where a is the anion-cation distance.

	Ag-Ag	Ag-Cl	Cl-Cl
A/eV	16528.0	2416.48	1227.2
ρ/Å	0.2370	0.3302	0.3214
C_{ij}/eVÅ^6	336.0	275.0	75.0

	Ag-Ag-Ag	Ag-Ag-Cl	Cl-Ag-Cl	Cl-Cl-Cl
C_{ijk}/eVÅ^9	124.86	758.67	30.22	8988.96

The use of these three-body potentials proved problematic in our defect simulations, where the majority of calculations failed to converge due to a poor choice of radial cut-off distance for the Axilrod-Teller potentials. The cut-off, which defines which species will interact, was chosen to be 5.5Å, which is very close to the cubic cell length of 5.5064Å. The original calculations were performed using the CASCADE[153] code, in which a database of interacting species was created at the initialisation stage, and was not updated. With the increased computing power available today, the GULP code calculates the interacting species before

Table 3.3: The three-body interatomic potentials of Baetzold *et al.* for AgBr.[5] The shell charges and spring constants are: Q_{Ag}=-25.967$|e|$, Q_{Br}=-2.705$|e|$, k_{Ag}=4109.34 eVÅ^{-2} and k_{Br}=24.66 eVÅ^{-2}. The corrected values of the Axilrod-Teller coefficients, C_{ijk}, are reported here. The two- and three-body cut-offs are 2.5a, and 5.5Å respectively, where a is the anion-cation distance.

	Ag-Ag	Ag-Br	Br-Br
A/eV	16528.0	4943.0	2948.2
ρ/Å	0.2370	0.3012	0.3320
C_{ij}/eVÅ^6	268.0	228.4	248.0

	Ag-Ag-Ag	Ag-Ag-Br	Br-Ag-Br	Br-Br-Br
C_{ijk}/eVÅ^9	300.09	14.47	0.00	20293.63

each geometry optimisation step. With large values of C_{ijk}, as we have here, atoms that interact do so strongly, which can cause ions to move in and out of the cut-off sphere, causing large changes in the total energy, and hence the convergence problems we observed.

Consequently, although these are possibly the most accurate shell-model potentials available, their applicability is limited unless they are re-parameterised using a more suitable cut-off distance.

3.2.3 Potentials of Kiang and Goddard III

The results reported from this systematic study of the effects of polarization on the AgBr phonon dispersion curves appear promising.[8] However, using their favoured set of potentials (Set V), we find the crystal to be unstable. Using a simpler model (Set III), we achieve stability, but do not obtain properties of the quality reported by the authors.

It is clear that unreported methodological differences may be the cause of these discrepancies. However, converting their *exponential-6* term to the form of a standard Buckingham potential (Equation 2.2) and combining their three fitted coefficients to obtain A, ρ and C has revealed to us their unphysical nature. These potentials are clearly of little value, and consequently, no further investigation was carried out.

3.2.4 Conclusions

It is evident from the work reported here that there are no satisfactory shell-model potentials for the silver halides. This problem is probably attributable to the lack of a quadrupolar term in the potential and the inability to model the effects of hybridisation in the valence band. However, it is also clear that the extent of this deficiency depends upon the property which is being calculated. Elastic and dielectric properties, for example, can be modelled accurately using three-body interaction potentials and the shell model.

While the general applications of these type of potentials are limited, their use in a combined QM/MM scheme, such as described in Section 2.6.2, can easily be justified. The remainder of this chapter is therefore concerned with the derivation of new potentials tailored to this purpose.

3.3 New Interatomic Potentials

3.3.1 Investigation of the Repulsive Potential

Early interatomic potentials relied upon fitting the coefficients of the analytical forms described previously to experimental data using approximate mathematical relationships. As previously mentioned, Mayer calculated the dispersion coefficients for a number of ionic materials on the basis of ultraviolet absorption spectra and polarizability data.[150] However, for many years it has been possible to undertake numerical fitting procedures so that parameters can be fitted to a large body of experimental data, such as structural, elastic, dielectric and phonon properties.

With increased computing power, first principles calculations have been used to provide a greater understanding of ion-ion interactions.[154,155] For the silver halides, techniques based on the electron gas method[156] have been used by Catlow *et al.*[3] and Jacobs *et al.*[4] to calculate the A and ρ parameters in the Buckingham potential for AgCl and AgBr.

In this work, we have applied a modern hybrid density functional, and a very accurate basis set, to investigate the interaction between pairs of like ions, where parameters fitted empirically are more uncertain. To a reasonable approximation, the resultant interaction curves are formed from three components. The dominant of these is, of course, the Coulomb repulsion, to which is added short-

range repulsion and an attractive term. Although this approach appears similar to the description of the Buckingham potential, there are no dynamical van der Waals interactions in these (static) calculations, and thus the attraction is not of the same origin. Instead, it is present due to the monopole-induced dipole and induced dipole-induced dipole interactions between two charged, polarizable, species.

Our aim is therefore to strip away the Coulomb and attractive interactions, leaving behind only the repulsive part of the potential. We should then be able to assess the suitability of the Buckingham repulsive potential for these interactions, and determine accurate values for the A and ρ parameters.

If we assume the ions to be structureless point dipoles, we can calculate this interaction analytically (for proof see Appendix A), resulting in the following expression for identical species with unit charge:

$$U(r) = -\frac{\alpha}{r}\left(\frac{r^3 - 2\alpha}{r^6 - 4\alpha^2}\right) - \alpha r^2 \left(\frac{r^3 - 2\alpha}{r^6 - 4\alpha^2}\right)^2, \tag{3.1}$$

where α is the polarizability of the two identical species.

We have therefore fitted this function to the attractive region of our Coulomb-subtracted quantum mechanical data. Despite having only one free parameter, a very accurate fit can be achieved for the chloride-chloride interaction. The fitted parameter can then be fed back into the equation, so that the attractive component can be removed from our data. The repulsive part of the Buckingham potential can then be fitted to the remaining data, and the A and ρ parameters can be determined.

For the the silver-silver interaction, the one-parameter attractive potential did not provide a sufficiently good fit. For this reason, dependence upon hyperpolarizability was introduced into our derivation. Unfortunately, with these terms, an analytical result for the attractive potential could no longer be deduced. However, using an iterative scheme, a power series was determined (see Appendix A), which for identical, singly charged, ions reduces to:

$$U(r) = -\frac{2\alpha}{r^4} + \frac{6\alpha^2}{r^7} - \frac{16\alpha^3}{r^{10}} - \frac{5\beta^2}{2r^{11}} + \frac{40\alpha^4}{r^{13}} + \cdots, \tag{3.2}$$

where β is the hyperpolarizability.

Using this equation, a good fit to the quantum mechanical data was then

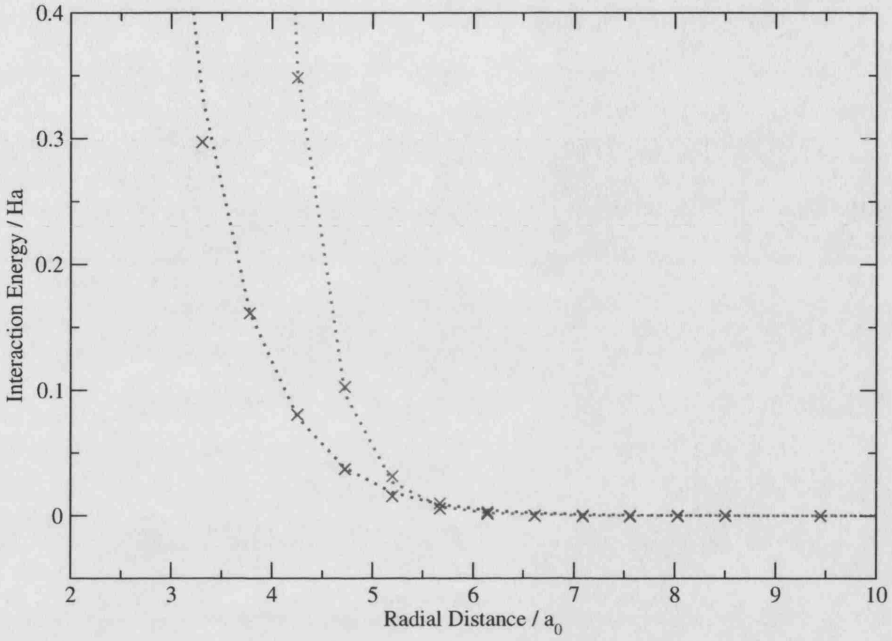

Figure 3.1: The hybrid-DFT-derived repulsive potentials for Ag-Ag (blue) and Cl-Cl (green). In each case, the crosses are the DFT data, while the dashed lines correspond to a Buckingham-fit with the parameters shown in Table 3.4.

possible by varying the two parameters α and β. Again, the fitted parameters were fed back into the equation, allowing us to remove the attractive contribution from the interaction curves. It should be noted that applying this expansion to the chloride data resulted in a negligible hyperpolarizability, and thus we reverted to the analytical expression for this case.

Table 3.4: The repulsive parameters derived from QM data.

	Ag-Ag	Cl-Cl
A/eV	1057000	1423
ρ/Å	0.194	0.346

The repulsive potentials obtained using this methodology are shown in Figure 3.1, with the fitted values of A and ρ reported in Table 3.4. It is clear that the exponential dependence of the Buckingham repulsive potential is well suited to modelling these interactions. Furthermore, the trends shown here are in agree-

ment with our knowledge of the electronic structure of these ions: the silver ion is larger but relatively dense, whilst the chloride ion is smaller but more diffuse, i.e. $A_{Ag} > A_{Cl}$ and $\rho_{Ag} < \rho_{Cl}$. These trends are also shown in the values derived by empirical methods (see Tables 3.1 and 3.2), and thus give them a solid theoretical footing.

These parameters were then used in the derivation of a new set of shell model potentials, described in the following section.

3.3.2 Derivation of a QM/MM Interatomic Potential

Bearing in mind the intrinsic limitations of the shell model for studying the silver halides, we have not attempted to model every property of these materials accurately. For use in a QM/MM embedding scheme, accuracy in some properties is more important than for others.

For our calculations, the following are the most important factors:

- lattice parameters, so that the electrostatic potential within the QM region is accurate;
- elastic constants, so that the structure responds correctly upon relaxation;
- dielectric constants, so that for charged systems, polarization of the crystalline environment is correctly described;
- surface relaxations, so that the surface structure of the MM regions matches that of the central QM region.

In previous work it has been shown that shell-model potentials with three-body interaction terms can achieve most of these objectives.[5] The use of three-body potentials for surface calculations has not been investigated. However, we cannot envisage their inclusion adversely affecting the accuracy of these calculations.

Due to inconsistencies in the implementation of the Axilrod-Teller potential between codes (see Section 3.2.2), we decided against using this form for our new potentials. Instead, we employed the simple `bcross` potential, which is normally used in molecular mechanics simulation, but is also physically justified for use in ionic materials as it can model ionic deformation. It takes the form:

$$U(R_i, R_j) = K(R_i - r_e)(R_j - r'_e) \tag{3.3}$$

where K is a fitted constant, r_e,r'_e are fixed equilibrium bond lengths, and R_i,R_j are the interionic separations.

The experimental data included in the fitting procedure were the lattice parameter, the elastic and dielectric constants, and the phonon frequencies at the Γ, X and L points of the Brillouin zone. Although we used the results of the previous section as starting points (initially holding their values fixed), we found that we could substantially improve the fit to our data by optimising these parameters. This finding is not unexpected, as we know that essential aspects of the physics of this material are missing from our model, and as a result, the parameters in our fitting procedure will adjust to compensate. In total we fitted the 15 parameters reported in Table 3.5 to 20 experimental values. As can be seen from Table 3.6 the bulk properties obtained from these potentials are of as good quality as those from previous potentials.

Table 3.5: Our QM/MM shell-model interaction potentials for AgCl. The shell charges and spring constants are: Q_{Ag}=-2.9427|e|, Q_{Cl}=-3.4656|e|, k_{Ag}=906.04 eVÅ^{-2} and k_{Cl}=33.70 eVÅ^{-2}. All two-body interactions are included up to 10 Å. The three-body interactions pivot around the centre ion in the triplet, and are nearest-neighbour only.

	Ag-Ag	Ag-Cl	Cl-Cl
A/eV	40619.7	3385.7	6265.0
ρ/Å	0.2411	0.2754	0.3219
C_{ij}/eVÅ^6	53.126	4.987	174.240

	Cl-Ag-Cl	Ag-Cl-Ag
K/eVÅ^{-2}	0.251	-0.07

Finally, we have employed the MARVINS code to examine the surface relaxations of the non-polar (100) surface of AgCl, the object of our QM/MM calculations in Chapter 5. For reasons of accuracy and efficiency, we need the surface properties calculated using our potentials to match those from QM calculations as closely as possible.

Figure 3.2 shows the surface which has been relaxed using our MM potentials. The relaxations, as shown on the right of the figure, display the characteristic

Table 3.6: Comparison of interatomic potentials for AgCl.

	Experiment	Catlow*	Baetzold†	This Work
Lattice Parameter / Å	5.506	5.506	5.511	5.502
Relative Permittivity				
ϵ_0	9.55	9.49	9.48	9.59
ϵ_x	3.97	3.97	2.99	3.86
Elastic Constants / GPa				
C_{11}	75.9	88.5	74.9	74.9
C_{12}	39.1	14.0	36.5	41.2
C_{44}	6.89	12.8	11.6	20.2

*Constant volume calculation using the potentials of Catlow *et al.* from Reference 3.
†Constant pressure calculation using the potentials of Baetzold *et al.* from Reference 5.

'rumpling' effect exhibited by other rocksalt-structured materials.[157–159] With our potentials, the cations sink into the surface slightly while the anions rise.

The magnitudes of these relaxations have been compared with equivalent surface-slab calculations performed using the plane wave DFT code CASTEP[160] (see Chapter 4 for further details). In this technique, a two-dimensional slab is periodically repeated in one dimension, and modelled using a code employing three-dimensional periodic boundary conditions. Care must be taken that the slabs are sufficiently isolated from each other. Likewise, the slab should be thick enough that the two external faces do not interact. Of course, these demands must be offset by the computational demands of such a calculation. For these calculations we used a vacuum gap of 25Å, and slab of AgCl 20Å thick, which we found to give converged results. All other details of the calculations were identical to those described in Chapter 4.

As can be seen from Table 3.7, both set of results predict that the surface chloride ions will relax further out of the surface than the silver cations. There is a large discrepancy in the average position of each layer; our MM results predict a slight inward relaxation of the surface layer, with the direction of relaxation oscillating in the subsurface layers, while the QM results predict outward relaxations for all layers. Unfortunately, there are no experimental data with which to compare our results.

We consider that this unusual behaviour can be explained by comparing the electronic structure in the bulk and at the surface. As discussed in the Intro-

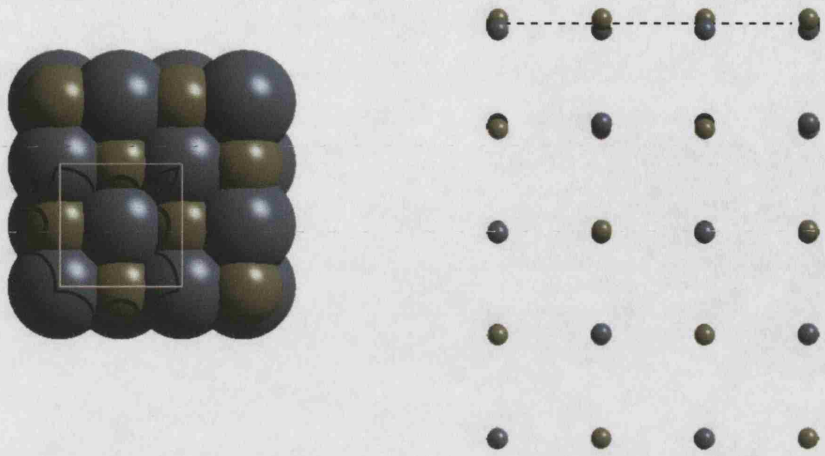

Figure 3.2: The MM-relaxed (100) surface of AgCl. The figure on the left shows a plan view of the surface with the surface unit cell, while the figure on the right illustrates the surface relaxations by looking along the (100) plane.

duction, strong $p - d$ hybridisation occurs in the valence band of silver chloride, which has the effect of shortening the ionic separations. Towards the surface, this electronic structure is perturbed and the degree of hybridisation is reduced. As a consequence, the ionic separations increase, resulting in the observed behaviour.

It seems that shell model interatomic potentials will not be able to model this surface relaxation accurately. However, we consider that we can proceed with QM/MM modelling on the basis that the errors introduced into the electrostatic potential of the central region by this incorrectly-described surface will be small. The results of our QM/MM calculations are therefore reported in Chapter 5.

Table 3.7: A comparison of surface rumpling using the CASTEP and MARVINS codes. The values quoted are vertical displacements from the unrelaxed lattice-site positions / Å.

	MARVINS		
	Ag-topped	Cl-topped	Average
Surface Layer	-0.18	+0.11	-0.04
Surface - 1	-0.07	+0.10	+0.02
Surface - 2	-0.03	+0.01	-0.01

	CASTEP		
	Ag-topped	Cl-topped	Average
Surface Layer	+0.22	+0.42	+0.32
Surface - 1	+0.24	+0.33	+0.29
Surface - 2	+0.18	+0.22	+0.20

Chapter 4

Periodic DFT

In this chapter we have applied the supercell technique, along with a plane wave basis set, to study defects within the bulk of the rocksalt-structured silver halides.

The plane wave basis set, although not as efficient as the atom-centred set, provides two distinct advantages when dealing with isolated point defects in solid-state materials:

- For a given level of theory, the accuracy of a calculation is determined by a single parameter (see Section 2.3.2),
- All space is treated equally, with no bias towards atomic positions. Hence, vacancies are described at the same quality as their surrounding ions.

The disadvantage of this choice is that it can only be applied to systems which have periodic boundary conditions in three dimensions. In order to calculate the energies of isolated ions or defects, they must be placed in a large enough supercell that interaction between periodic images is minimal.

After a description of the methodology used in this work, the energetics and geometrical structures of the charged point defects in AgF, AgCl and AgBr are reported. Following on from this, the forms of the corresponding neutral defects, and the localisation patterns of the trapped electron/hole are discussed.

4.1 Method

The new version of the CASTEP (CAmbridge Sequential Total Energy Package) code[160] was used for these calculations as it employs the plane wave-pseudopotential

methodology, and has the functionality to deal with charged defects. Additionally, the source-code is available and has been optimised for the UK terascale supercomputing facilities, where many of these calculations were performed.

All calculations made use of the PBE[122] exchange-correlation functional, due to its accuracy and numerical stability. Further details are described in the following sections.

4.1.1 Pseudopotentials

Pseudopotentials are essential to the plane wave basis set methodology. The size of the basis set necessary to describe core electrons would make the calculations prohibitively expensive. Instead, their effects are included by incorporating them into a pseudopotential, as described in Section 2.4.

The PBE-derived ultrasoft pseudopotentials supplied with the CASTEP code were used for all calculations, having core and valence regions consisting of $([Kr]).4d^{10}.5s^1$ for silver, and $([He]).2s^2.2p^5$, $([Ne]).3s^2.3p^5$ and $([Ar].3d^{10}).4s^2.4p^5$ for fluorine, chlorine and bromine respectively.[160] Crucially, these pseudopotentials were derived using relativistic theory, and hence have the properties necessary for an accurate description of the heavier ions.[161]

4.1.2 Basis Set

As detailed in Section 2.3, the size of the basis set in a plane wave calculation is defined by its cut-off energy. Wave vectors greater in energy than this cut-off energy will be excluded from the wavefunction expansion. Increasing the cut-off will therefore improve the accuracy of a calculation, but will also increase its cost. A balance between these two factors must be achieved.

A thorough study of the convergence behaviour of the defect energies with the plane wave cut-off has been performed for all three materials. Very similar behaviour was observed in each case, suggesting that the description of the silver cation is the key factor affecting the accuracy of these calculations. We found that using a cut-off of 350eV leads to defect energies, for both charged and neutral point defects, that are converged to within 0.01eV.

4.1.3 Reciprocal Space Sampling

The sampling scheme used here is that of Monkhurst and Pack,[162] which simply consists of a regular grid of points in reciprocal space. Such a set can be specified by three integers, corresponding to the number of points in each direction in reciprocal space.

A study of the convergence of the defect energy with the density of the k-point grid was performed for each of the three materials. It would be expected that the convergence would be faster for closed-shell charged defects than for neutral defects with trapped electrons or holes. Consequently, convergence was investigated for two systems: the charged and the neutral anion vacancy (F-centre). This defect was chosen as it represents a well-behaved system in both charge states.

As expected, the neutral defect converged more slowly, requiring a k-point density of 33Å to achieve convergence to within 0.01eV. For the corresponding charged defect, a grid of only 22Å was needed. For consistency, a grid of 33Å was used for all calculations, which corresponds to 3x3x3 k-points for a cubic 64-ion supercell and 2x2x2 k-points for a cubic 216-ion supercell. For most calculations, this number was drastically reduced by the application of symmetry.

4.1.4 Validation

As a test of these parameters, the gas-phase dimers, both homonuclear and heteronuclear, involving silver and the three halide anions were modelled, maintaining periodic boundary conditions by placing each dimer in an empty unit cell of sufficient size to isolate the dimer from its images. For ease of comparison, a cubic cell with lattice parameter equal to that of our AgCl 64-ion supercell (described later) was chosen ($a = 11.066$Å). The results of these calculations are tabulated in Table 4.1, along with corresponding experimental results. While the bond lengths are in good agreement (within 2% of experimental values) the bond dissociation energies are less well reproduced, with the halogen molecules being strongly overbound. It should be noted, however, that these homonuclear diatomics represent a 'worst case scenario' in that the pseudopotentials will have been generated and optimised for closed-shell X^- species, and would be expected to perform better for X_2^{2-} dimers than for the X_2 molecules studied here. By contrast, the heteronuclear diatomics, in which charge-transfer will have occured,

Table 4.1: Dimer properties calculated within periodic boundary conditions using the CASTEP code.

	Bond Length (Å)		Dissociation Energy (eV)	
Dimer	This Work	Experiment	This Work	Experiment
Ag_2	2.58	2.53[163]	1.75	1.64[164]
F_2	1.43	1.41[165]	2.22	1.66[166]
Cl_2	1.98	1.99[165]	2.90	2.51[166]
Br_2	2.31	2.28[165]	2.41	1.98[167]
AgF	2.03	1.98[165]	3.55	3.67[168]
$AgCl$	2.29	2.28[165]	3.14	3.24[169]
$AgBr$	2.42	2.39[165]	2.84	3.01[168]

are modelled far more accurately, with binding energies within 0.2eV of experimental values. We consider therefore that for the defect systems studied here, the set of parameters used for these calculations should lead to minimal error.

4.1.5 Defect Calculation Methodology

All calculations within this Chapter were performed using the supercell method. The lattice parameters of these cells were chosen as integer multiples of the cubic values obtained through initial constant pressure geometry optimisation calculations. These values are discussed in the next section, and are reported in Table 4.2. As we are attempting to describe the properties of isolated point defects, all subsequent calculations were performed at constant volume.

Initial calculations were performed using a cubic supercell containing 64 ions, of which only the inner 27 were allowed to relax, leaving the boundary atoms fixed. A select number of calculations were also performed using larger supercells containing 216 ions. For these, an extra spherical shell of ions was allowed to relax, bringing the total number to 33.

The defect was placed near the centre of the cube, and symmetry was imposed on the cell, where appropriate, to reduce computational expense. We can be confident that our supercells adequately enclose the major structural relaxation around the defects in question, as the displacements of the outer ions are small. However, a proper description of the electronic effects may require a larger cell.

When modelling aperiodic systems within periodic boundary conditions, the

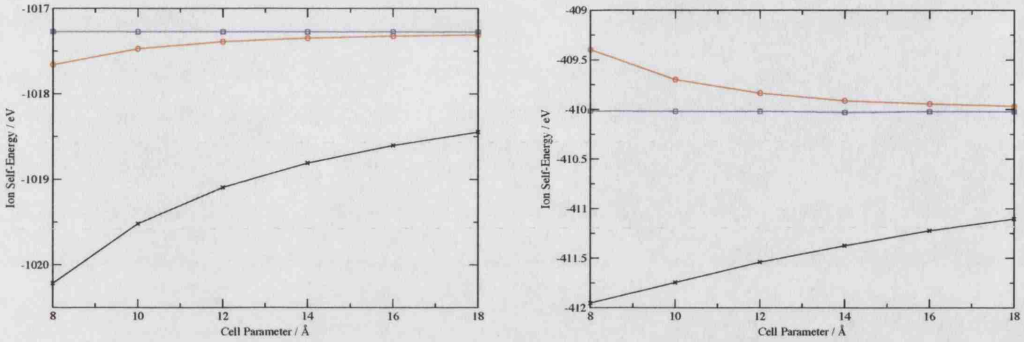

Figure 4.1: Convergence of the ion self-energy with cubic supercell size for Ag^+ [left] and Cl^- [right]. Black lines and crosses are the raw energies output by CASTEP, which converge as L^{-1}. Red lines and circles are the same energies corrected by the Leslie-Gillan term,[99] and converge as L^{-3}. Finally, the blue lines and squares correspond to the energies that have been corrected according to the Makov-Payne scheme,[100] which converges as L^{-5} or faster.

choice of k-point sampling in the first Brillouin zone is critical.[170] A good choice can accelerate convergence with supercell size by minimising defect-defect interactions. We followed Makov *et al.*,[170] who suggested using a converged Monkhorst-Pack k-point set for calculations on smaller cells, but on larger cells where gamma-point calculations would normally suffice, substitute a set of k-points, which would exclude the direct interaction of a defect with its nearest images. For cubic systems such as the silver halides, a set containing four $(\frac{1}{4}, \frac{1}{4}, \frac{1}{4})$-type k-points was reported to be the most efficient.[170]

For all charged defect calculations the correction terms described in Equation 2.16 have been applied *a posteriori*. Evaluation of the first term (L^{-1}) could be performed routinely, and had the effect of destabilising each charged defect by approximately 0.2 eV. Calculation of the second term (L^{-3}) was more involved, as it required us to analyse the positions of the nuclei and the electron density within the supercell to produce a value for the quadrupole moment, Q, for the defect. As can be seen in Figure 4.1, these corrections worked very well for isolated ions (which can be considered as defects in the vacuum of an empty cell), and a reasonable energy was obtained from all of the supercells studied.

For defects in the solid state, the density of the defective cell can be divided into two contributions: the underlying defect-free lattice; and an aperiodic overlay which resembles a molecular density, and represents the isolated point defect.

The spurious interactions between the aperiodic densities in neighbouring cells accounts for the observed supercell size dependence, and our value for Q must be obtained from this density.

As shown in Equation 2.16, the correction was reduced by the dielectric constant of the material to account for dielectric response. Experimental values for this property were used for AgCl and AgBr. Due to lack of experimental data for AgF, a reasonable estimate was made. However, the defect energies would not be expected to be strongly dependent upon the chosen value.

4.2 Pure Material

As an initial test of the reliability of these calculations, fundamental properties of the silver halides have been calculated. The cubic lattice parameter, a, the bulk modulus, B, and the three elastic constants, C, are shown in Tables 4.2 and 4.3, which were calculated using a primitive unit cell and the Finite Strain technique [171, Appendix G].

Table 4.2: The cubic lattice parameters for the silver halides at absolute zero.

	Calculated	Experiment
AgF	5.01	(4.94)†
AgCl	5.53	5.51
AgBr	5.82	5.77

†Room temperature value from Ott.[172]

Table 4.3: Elastic properties of the silver halides at absolute zero. The bulk moduli, B, and the elastic constants C.

	B/GPa		C_{11}/GPa		C_{12}/GPa		C_{44}/GPa	
	Calc.	Expt.	Calc.	Expt.*	Calc.	Expt.*	Calc.	Expt.*
AgF	58.8	-	75.7	-	50.3	-	-3.8	-
AgCl	50.4	51.3	67.3	75.9	41.9	39.1	5.4	6.9
AgBr	37.9	49.8	53.8	75.5	29.9	36.7	7.5	8.3

*Elastic data for AgCl from the low-temperature data of Hidshaw *et al.*[18]
Elastic data for AgBr extrapolated from the high-temperature data of Cain *et al.*[20]

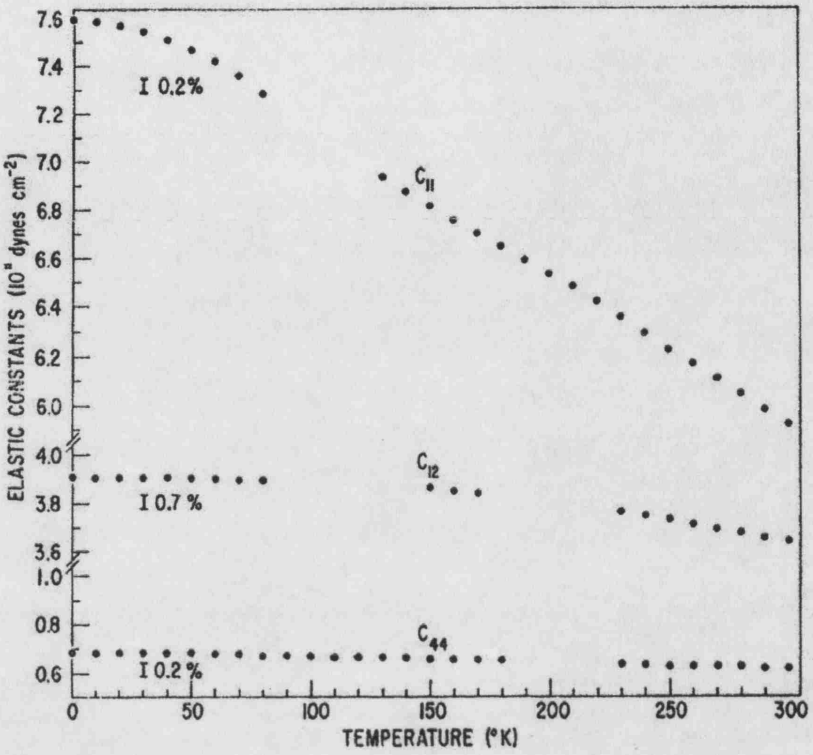

Figure 4.2: The variation of the elastic constants of AgCl with temperature, in the range 4.2 - 300K, from Reference 18.

As with other GGA-DFT calculations, the lattice parameters are systematically (slightly) overestimated due to incomplete self-interaction cancellation. The experimental values for the elastic properties of AgCl are extrapolated to 0K from data in the range 4.2 - 300K[18] and thus can be considered more accurate than the data for AgBr which are obtained from data in the range 273 - 673K.[20] Given the non-linearity at low temperatures found by the former authors (see Figure 4.2), the experimental data for AgBr can be considered only rough estimates. This may explain the apparent softness of AgBr in our calculations. To our knowledge, no experimental elastic data exist for AgF.

Given these results, we have confidence that our method more accurately represents the silver halides than the atomistic methods of previous defect studies.[3,5] These models, although fitted to structural and elastic data, failed to accurately reproduce the strong Cauchy violation ($C_{12} \neq C_{44}$) shown in the data in Table 4.3. This is an indication that fundamental interactions were unaccounted for in

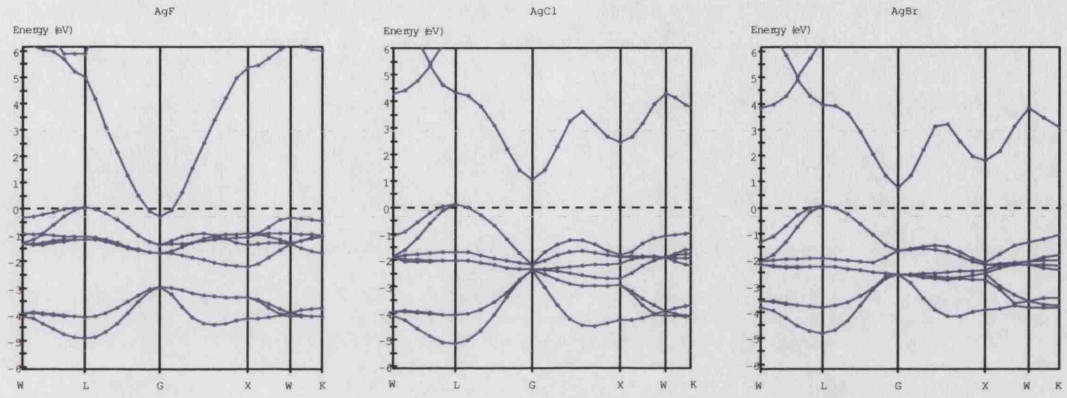

Figure 4.3: The calculated band structure of AgF [left], AgCl [centre] and AgBr [right]. Special points of the Brillouin zone: Γ/G=[0; 0; 0], X=[$\frac{1}{2}$; $\frac{1}{2}$; 0], K=[$\frac{3}{8}$; $\frac{3}{8}$; $\frac{3}{4}$], L=[$\frac{1}{2}$; $\frac{1}{2}$; $\frac{1}{2}$], W=[$\frac{1}{2}$; $\frac{1}{4}$; $\frac{3}{4}$].

the simple form of the interatomic potentials used in these studies. Furthermore, our results are in better agreement with experiment than earlier LDA calculations for AgCl,[34] highlighting the need for gradient-corrected (GGA) functionals.

Also considered were the basic electronic properties, shown in Figure 4.3 and Table 4.4. The use of Kohn-Sham eigenvalues to calculate band gaps is not theoretically justified and has been shown to be unreliable. Consequently, we also report here values calculated using the equation:[41]

$$\Delta E_{BG} = E[-] + E[+] - 2E[0] \tag{4.1}$$

where $E[-]$ and $E[+]$ correspond to the energy of a perfect cell containing an excess electron or hole respectively, and $E[0]$ is the energy of the pure, charge-neutral, perfect cell.

Table 4.4: Electronic properties of the silver halides.

	Direct Band Gap / eV		Indirect Band Gap (L $\rightarrow \Gamma$)/ eV		
	Calculated*	Expt.	Calculated*	Calculated†	Expt.
AgF	4.96	4.63	-0.36	0.52	2.8[173]
AgCl	4.22	5.15	0.94	1.73	3.245
AgBr	3.87	4.29	0.71	1.84	2.684

*Obtained via eigenvalue spectrum †Obtained via Equation 4.1

While our results are in good agreement with previous DFT studies,[34,35,174] each having an indirect $L \rightarrow \Gamma$ transition, as with all DFT calculations these band gaps are systematically underestimated.[41] Silver fluoride has been found to be a negative indirect band gap material in the eigenvalue spectrum, where it should have a positive gap of 2.8eV.[173] Based on a positive direct band gap we nevertheless attempt calculation of the defect properties. In this approach we expect to reproduce, to a first approximation, the properties primarily controlled by the charge density distribution (i.e. formation energies and structure of charged defects). However, the properties of excited and localised electron/hole defect states would be unreliable.

4.3 Energies of Charged Defect Formation

Our intention is to elucidate the energetic and structural properties of the defect pairs in the silver halides. Initially, we have studied the energetics of formation of individual charged defects in the limit of infinite separation. These individual defects are the species previously studied by Mott-Littleton-based atomistic modelling[3,5] and conductivity measurements.[57,68]

We have thus considered three processes:

- Adding a silver ion to form a cation interstitial defect:

$$Ag^{+}(g) \longrightarrow Ag_{I}^{\bullet}. \tag{4.2}$$

- Removing a silver ion leaving a cation vacancy:

$$Ag_{Ag} \longrightarrow V'_{Ag} + Ag^{+}(g). \tag{4.3}$$

- Removing a halide ion resulting in an anion vacancy:

$$X_{X} \longrightarrow V_{X}^{\bullet} + X^{-}(g). \tag{4.4}$$

The resulting defect energies are reported in Tables 4.5, 4.6 and 4.7. Unfortunately, it is not possible to calculate the formation energies of individual defects

Table 4.5: Defect formation energies for AgF / eV.

	This Work
Cation Frenkel Pair	0.74
Schottky Pair	0.49

Table 4.6: Defect formation energies for AgCl / eV.

	This Work	Interatomic Potentials[5]	Experiment
Cation Frenkel Pair	0.36	1.46	1.45[55]
Schottky Pair	0.80	1.70	>1.5[52]

consistently (see Section 2.6), and thus the energies reported are for defect pairs only. It should be noted that experiment also only provides these values.

It can be seen from the tables, that the dominance of the charged cation Frenkel species for AgCl and AgBr is correctly predicted. Preliminary calculations, which we now believe were not fully converged (so have not been reported here), indicated that in all three materials the anion Frenkel species has a considerably higher formation energy. Therefore, they are very unlikely to be found in the real material. Again, experimental data are not available for AgF, so the results here must be considered as predictions.

All values are systematically lower in energy than would be expected, which is likely to be due to the incorrect description of electrostatic potential in the cell. For charged defects such as these, the potential in the supercell is contaminated with contributions from the periodic images of the defect. For example, it has recently been shown that the Makov-Payne corrected ionisation potential of an F-centre in a 64-ion supercell of NaCl is in error by 0.8eV for this reason.[175] Schultz has proposed an alternative to the jellium compensating scheme which correctly represents the electrostatic potential, and provides considerably more accurate defect energies.[175,176] However, his method requires a mixed boundary condition approach, and as such is incompatible with our plane wave basis set.

It should be noted that the positions of the energy bands vary with the defect charge state due to the change in the potential. An alternative correction scheme would be to line-up the low-energy core states between charged and neutral calculations. However, due to our use of pseudopotentials in our calculations, the

Table 4.7: Defect formation energies for AgBr / eV.

	This Work	Interatomic Potentials[5]	Experiment
Cation Frenkel Pair	0.03	1.05	1.00-1.05
Schottky Pair	0.98	1.40	-

core states were not clearly defined.

To our knowledge, the only method of improving the quality of our results was to employ a larger supercell in which the periodic charged defects were further separated. In order to investigate this we have performed key calculations using a larger, and more computationally expensive, 216-ion supercell. These calculations were only performed on silver chloride due to the large resources they require. The results of these calculations are shown in Table 4.8, along with the previously reported results for the smaller 64-ion cell.

Table 4.8: The convergence of defect formation energies with supercell size for AgCl / eV.

	64-Ion	216-Ion	Interatomic Potentials[5]	Experiment
Cation Frenkel Pair	0.36	0.77	1.46	1.45[55]
Schottky Pair	0.80	0.80	1.70	>1.5[52]

It can be seen from the table that the larger cell produces a Frenkel energy that is closer to the experimental value. The unchanged Schottky energy is more likely to be coincidence rather than being indicative of convergence having been achieved. Our 216-ion calculations reported here are at the limits of the currently available computing power. Hence, calculations using the next-largest cubic supercell (512-ions) would not be feasible. Instead, alternative methods, such as the QM/MM embedded cluster technique used in Chapter 5, should prove more efficient.

It is interesting to note that DFT correctly predicts the ordering of the defect pairs in AgCl and AgBr. There has been much debate over the last 25 years over the origin of the unique properties of the silver halides, including the dominance of the cation Frenkel defect.[6] It was previously thought that interatomic van der Waals forces stabilise the silver interstitial, lowering the Frenkel energy. DFT methods cannot model accurately the long range van der Waals attraction, but

as we have shown, still predict the dominance of this form of defect.

4.4 The Atomic Structure of Charged Defects

In this section, the atomic structure of each charged point defect is described. These properties are more reliable than the energetics obtained for the same models, as the energy difference between two similar configurations will, to a first approximation, be free of the problems described in the previous section.

4.4.1 Interstitial Silver Ion

The interstitial cation defect is of considerable interest as it is present in high concentrations in silver halide crystallites, and is unusually mobile. Most previous analyses assumed the interstitial ion in the silver halides to be at a body-centred (BC) site. Energetics from atomistic calculations on charged interstitials supported this assumption,[3–5] and it became the model with which all subsequent experimental data were interpreted.[57,68]

Our calculations on all three halides have shown the BC structure to be unstable. Instead, we have found the equilibrium configuration to involve a second cation, forming a dumbbell-shaped split-interstitial structure centred on a lattice site (see Figure 4.4), in agreement with the Hartree Fock results of Baetzold and Eachus[71] for AgCl and the ENDOR work of Bennebroek *et al.*[60,61] on AgCl and AgBr. It is worth noting that the interaction between the quadrupole moment of the defect and the background charge destabilised the split-interstitial structure to a greater extent than the BC structure, and thus application of our *a posteriori* correction terms was crucial when calculating the energy differences.

However, there is disagreement over the orientation of this Ag_2^{2+} species. Bennebroek *et al.* proposed a [110] orientation for the *neutral* defect in AgCl, and suggest that the charged defect should be qualitatively similar due to the diffuse nature of the trapped electron (with an effective radius estimated at 16.6Å). The orientation of the Ag_2^{+} species in AgBr could not be determined due to low spectral resolution. Our calculations, however, suggest a [111] orientation is more stable in AgCl by 0.4 eV. Similarly, we found the same equilibrium structure in AgF and AgBr. This is also the model Baetzold used for his Hartree Fock and post-Hartree Fock calculations, as well as being the most intuitively reasonable

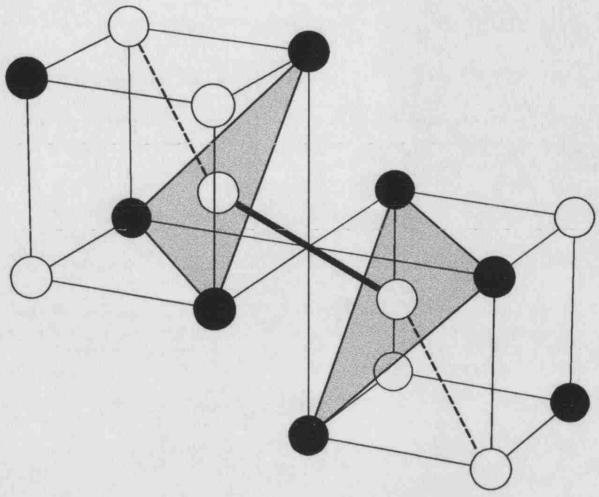

Figure 4.4: Illustration of the charged Ag_2^{2+} split-interstitial species in the [111] orientation, with a typical cation chain highlighted. White circles represent silver ions, black represent halide ions.

structure.

Bennebroek's analysis hinges upon how the symmetry of the split-interstitial species affects the equivalency of the surrounding shells of ions. In the ^{109}Ag ENDOR spectra for AgCl shown in Figure 4.5, the intensities of the peaks the authors assign to the second shell of silver ions have a 2:1 ratio. This is consistent with a symmetry of D_{4h}, and thus a [110] orientation. If their analysis was self-consistent and peak assignment was correct, it would be expected that the first peak would also be split.[177] This is not the case, and as such, doubt must be cast on their analysis.

As is common when dealing with H-centres in the alkali halides, the split-interstitial species can be treated as a molecular dimer within the crystal.[59] The bond length of the charged Ag_2^{2+} dimer was found to be 2.95Å in AgCl, with the silver ions located at the centres of two triangles of chloride ions, as shown in Figure 4.4. The distance between each member of the dimer and its nearest cation neighbours was found to be 2.94Å. We therefore observed chains of cations with approximately equal separation (indicated in Figure 4.4), suggesting the importance of electrostatics in determining the structure. The slight inequality in the bond lengths is likely to be due to electrostatic interactions with the surrounding chloride anions, which were situated at a distance of 2.49Å from each

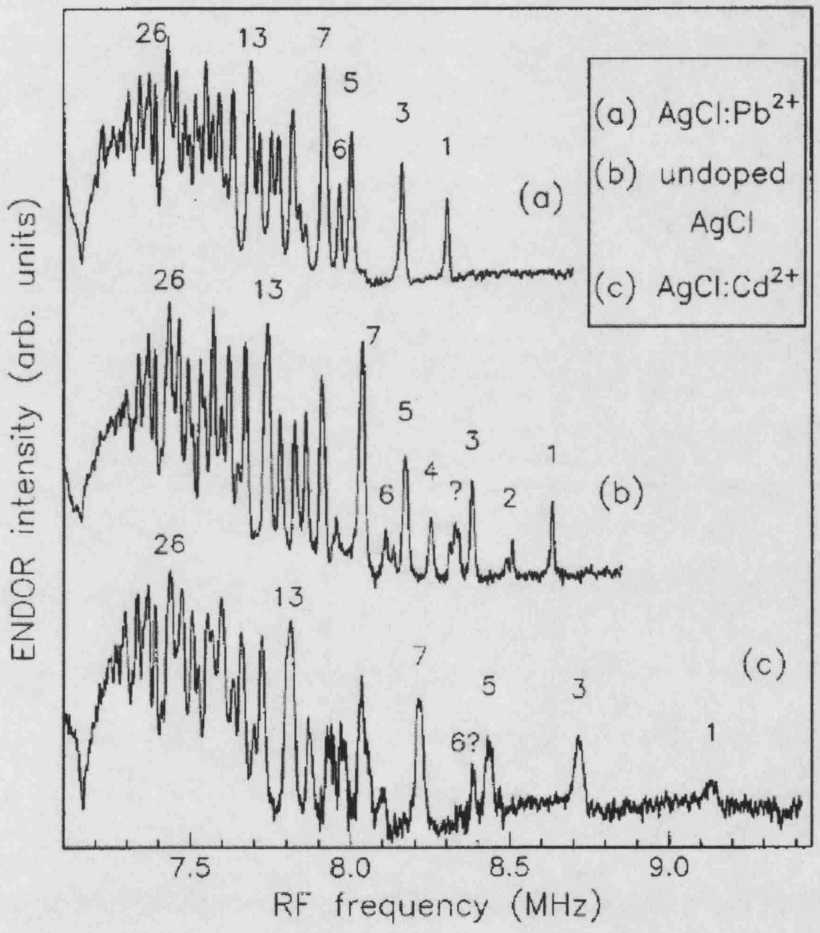

Figure 4.5: The ^{109}Ag ENDOR spectrum of AgCl from Reference 61. The authors propose that the peak labelled '2' in spectrum (b) indicates the D_{4h} symmetry of the Ag_2^+ species.

cation (0.28Å shorter than normal separation in pure AgCl, but with silver in a trigonal, rather than octahedral, configuration), displaced only slightly from their lattice sites (0.02Å outwards) due to the competition between Coulombic attraction and short-range repulsion. Silver fluoride showed very similar behaviour to AgCl, while AgBr had a longer dimer bond length, as can be seen in Table 4.9 together with the data for AgCl. While the interstitial ions in the smaller halides appeared to be sterically unrestricted in their triangle-centre equilibrium positions, the larger size of the bromide ions resulted in less free space for the cation, and therefore the anions relaxed outwards to reduce the short-range repulsion.

Table 4.9: Bond lengths around the Ag_2^{2+} dimer / Å. Subscripted ions are those of the interstitial pair, while unsubscripted ions are on lattice sites.

	$Ag_I - Ag_I$	$Ag_I - Ag$	$Ag_I - X$	$Ag - X$
AgF	2.69	2.76	2.28	2.50
AgCl	2.95	2.94	2.49	2.77
AgBr	4.11	2.89	2.64	2.91

To validate this analysis we performed calculations purely of the electrostatic energies. Atomic coordinates from our DFT calculations on each material were imported into the GULP code,[148] and assigned full ionic charges. Variation of the electrostatic energy was calculated as a function of the Ag_2^{2+} dimer bond length, while keeping the rest of the crystal fixed. This procedure gave an equilibrium bond length of 2.7Å for AgF, 2.9Å for AgCl and 3.1Å for AgBr. The values for AgF and AgCl are extremely close to the DFT data, confirming that electrostatic interactions control the structure of these system. Our tests on the molecular dimer, reported in Section 4.1.4, allow us to conclude that the interaction between silver cations at closer separation is well described, and hence corroborate our prediction for the split-interstitial geometry.

Migration Barriers

Calculations have also been performed on the body-centred interstitial species, as this geometry corresponds to the transition state for migration. As would be expected, in line with conductivity measurements, the barrier to migration was found to be very small. The barriers obtained by our method are shown in Table 4.10. A direct comparison with experiment is not possible as all experimental

data have been interpreted using a body-centred model.[70,178,179] However, our results compare very favourably with the averaged interstitial defect mobility values quoted by Weber and Friauf.[179] A reinterpretation based on the split-interstitial model would be very useful. However, the analysis would be far more complex as the migration path shows a greater degree of correlation.

Table 4.10: Barriers to migration / eV.

	Calculated	Experimental*
AgF	0.49	-
AgCl	0.06	0.05
AgBr	0.13	0.17

*Averaged interstitial defect mobility (Reference 179)

Previous atomistic calculations[66,180] have been used to study the difference in energy between the body-centred and split-interstitial species in AgCl. As mentioned above, these calculations find the BC geometry to be of lowest energy, with a [111]-orientated transition state 0.03eV higher in energy.[181] However, as stated in Section 4.2, we consider our method more accurately represents the silver halides, and thus can be considered more reliable.

With our equilibrium and transition state geometries and energies we can envisage facile motion of the interstitial species throughout the volume of the crystallite. Conversely, the [110] direction would restrict migration to within a plane, reducing the number of interstitial ions available for aggregation into a latent image cluster. This planar migration has not been observed in the silver halides. As a result our [111] orientation is the most likely candidate structure.

4.4.2 Silver Vacancies

For the corresponding charged cation vacancy, we observe small structural relaxations, as reported in Table 4.11. We find that the distance between the vacancy centre and nearest-neighbour anions increases, while the nearest silver ions relax inwards, as would be expected on electrostatic grounds.

Table 4.11: Inward displacement of shells of nearest-neighbour (NN) ions towards charged silver vacancies in the silver halides / Å.

	1st-NN	2nd-NN	3rd-NN
AgF	-0.11	+0.08	0.00
AgCl	-0.10	+0.06	-0.04
AgBr	-0.12	+0.05	-0.02

4.4.3 Anion Vacancies

Although anion vacancies are relatively rare in these materials, they are of inherent interest for two reasons:

- They form the counter-ion in the Schottky pair, and their study may elucidate why this defect type is less prevalent.
- Anion vacancies are well studied defects in the rocksalt alkali-metal halides, in which F-centres form readily.[59] Data from the silver halides would therefore provide an interesting comparison.

The calculated relaxations are reported in Table 4.12. We find that while AgBr obeys the expected behaviour based on electrostatics, the nearest-neighbour cations in AgF and AgCl relax towards the vacancy.

Table 4.12: Inward displacement of shells of nearest-neighbour (NN) ions towards charged anion vacancies in the silver halides / Å.

	1st-NN	2nd-NN	3rd-NN
AgF	+0.34	+0.12	-0.02
AgCl	+0.04	+0.11	-0.02
AgBr	-0.06	+0.10	-0.01

This is a further indication of the breakdown of the rigid ion model for these materials. As discussed in the Introduction, it is clear that the fundamental interactions within the silver halides differ from those of the alkali halides. The $p-d$ hybridisation, often referred to as partial-covalency, shortens the cation-anion distance. On removal of an ion to form a vacancy, the nature of the bonding around the defect necessarily changes. Around an anion vacancy, our results imply that

the bond-shortening effect is reduced, and therefore the nearest-neighbour cations must lower their energy by relaxing into the vacant space. The extent of this relaxation will be limited by the resultant changes in the electrostatic and short-ranged interactions. From the data in Table 4.12 we can see that this balance shifts smoothly from AgF to AgBr.

4.5 Energies of Formation of Neutral Defects

As has been previously described in the Introduction, the interactions between defects in the bulk and the electrons and holes liberated on photon capture are of great interest due to their relevance to the photographic effect. To increase the efficiency of the process, these electrons and holes must be prevented from recombining. Due to the small exciton binding energy (0.04 eV for AgCl, 0.022 eV for AgBr[182,183]) the electron-hole pair will rapidly dissociate into free species. Furthermore, due to the unusual band structure of the silver halides, the probability of free electron-hole recombination is small, as the process must be accompanied by a change in momentum (see Section 4.2). As a result, there is a low probability of recombination even in the pure silver halides.

This probability is, however, further reduced via hole trapping at negatively charged centres, such as the silver vacancy. The electron can also become trapped at a positively charged site such as an interstitial cation, although this centre is thought to be a very shallow trap and will thus only be significant at low temperatures.[184]

Using our method, we can calculate the energies of defect formation and also study the localisation of the trapped species. The processes we now study are subtly different from those described earlier:

- Adding a silver atom in its standard state (metallic silver) to form a neutral interstitial defect (which can be considered as an Ag^+ cation and an excess electron):

$$Ag(s) \longrightarrow Ag_I^{\bullet} + e^-. \tag{4.5}$$

- Removing a silver atom leaving a vacancy and an excess hole:

$$Ag_{Ag} \longrightarrow V'_{Ag} + h^+ + Ag(s). \tag{4.6}$$

- Removing a halogen atom resulting in a chlorine vacancy and an additional electron:

$$X_X \longrightarrow V^{\bullet}_X + e^- + \frac{1}{2}X_2(g). \tag{4.7}$$

As we are now dealing with adding and removing atoms in their standard states, and are maintaining charge balance, we are able to calculate point defect formation energies in addition to the formation energies of defect-pairs (see Section 2.6.1). The energetics for AgCl and AgBr are reported in Tables 4.13 and 4.14 respectively. Calculations on the trapping properties of AgF were not carried out for the reasons stated in Section 4.2.

Table 4.13: Formation energies of neutral and charged defects in AgCl / eV.

	Neutral Defects		Charged Defects	
	64 ion	216 ion	64 ion	216 ion
Silver Interstitial	2.07	1.76	-	-
Silver Vacancy	0.35	0.25	-	-
Chloride Vacancy	1.46	1.32	-	-
Cation Frenkel Pair	2.42	2.10	0.36	0.77
Schottky Pair	0.98	0.83	0.80	0.80

Table 4.14: Formation energies of neutral and charged defects in AgBr / eV.

	Neutral Defects	Charged Defects
Silver Interstitial	1.64	-
Silver Vacancy	0.36	-
Bromide Vacancy	2.66	-
Cation Frenkel Pair	2.00	0.03
Schottky Pair	2.28	0.98

Although the energies reported here can be considered to be more accurate than those of the charged defects, as all supercells were charge-neutral, it is clear

that we do not yet have convergence with supercell size. As will be explained in the following section, this is due to incorrect electron or hole localisation due to the presence of the defect images.

It should be noted that these energies of formation are included for the sake of completeness. Concentrations of point defects in the bulk are determined by the formation energies of charged pairs. As has been previously discussed in the Introduction, there are no deep electron traps in the bulk, with trapping occurring predominantly at surface sites. Unfortunately, due to the aforementioned problems with modelling charged systems within a supercell, and the deficiencies of GGA functionals in reproducing the band gap, accurate trap depths could not be calculated using this technique.

4.6 Structure and Localisation around Neutral Defects

The structure of the atoms around a neutral point defect is intimately related to the localisation of the excess hole or electron present. This relationship can be probed experimentally using electron spin resonance spectroscopy such as EPR and ENDOR. These techniques have both been applied to the study of the primary intrinsic defects in the silver halides.[48,50,60,61]

4.6.1 Interstitial Silver Ion

As described in Section 4.4, ENDOR spectroscopy identified a split-interstitial species in AgCl and AgBr, surrounded by a very diffuse trapped electron with Bohr radii of 16.6Å and 24.8Å respectively.[61] The corresponding optimised structures and electron localisations found by us are displayed in Figures 4.6 and 4.7. Our calculations predicted a small bond length increase of the Ag_2 species to 3.00Å for AgCl and 4.14Å for AgBr, which was indicative of shallow trapping. While a full quantitative comparison with experiment would require calculations on larger supercells capable of fully enclosing the electron density, we did observe diffuse localisation in both cases.

In AgCl, it can be seen that the electron density, although diffuse, is somewhat concentrated upon p-like polarization functions of the two interstitial cations. In

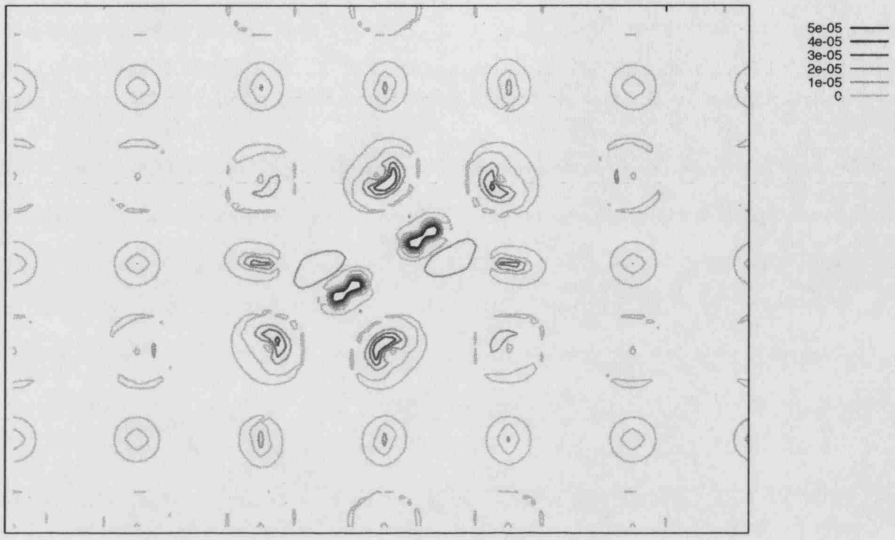

Figure 4.6: Spin localisation in defective AgCl: silver interstitial. Contour plot of the <110> plane in the larger 217-ion supercell containing the Ag_2^+ species (centre).

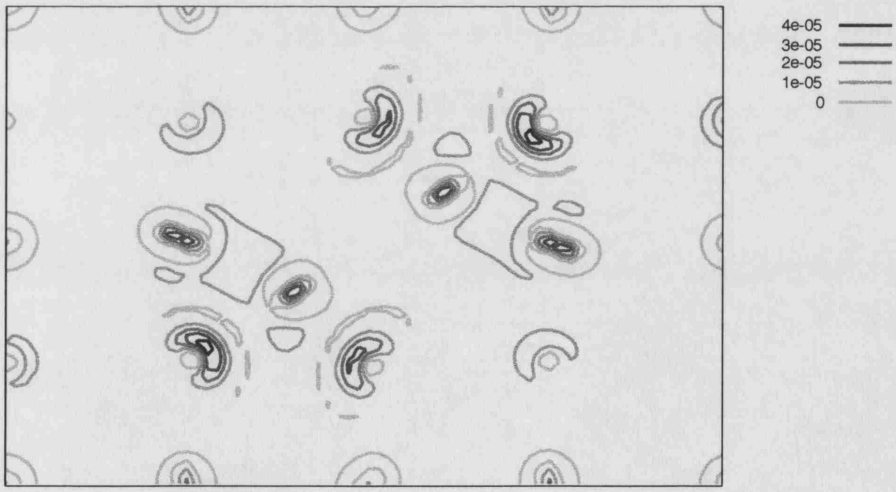

Figure 4.7: Spin localisation in defective AgBr: silver interstitial. Contour plot of the <110> plane in the smaller 65-ion supercell containing the Ag_2^+ species (centre).

contrast, the electron density is more evenly spread across a Ag_2Br_8 unit due to the increased dielectric constant.

It should be noted that some caution in the interpretation of our results is needed. GGA-DFT is well known to over-delocalise the electron distribution,[185] which may have the effect of increasing the bond lengths of the molecular ions in their neutral states, making the more constrained [110] geometries less favourable. However, our arguments based on conductivity and steric effects (Section 4.4.1) suggest that our [111] geometry can be considered more likely.

4.6.2 Silver Vacancies

The interaction of a silver vacancy with an electronic hole is perhaps of greatest interest, as the vacancy provides a deep trap, and is consequently more active in the photographic process. Examining the distribution of the hole in Figures 4.8 and 4.9, it can be seen that the hole predominantly localises on the silver cations, populating the $4d_{x^2-y^2}$ orbitals. This structure was found to be stable with respect to small symmetry-breaking perturbations of the nearest-neighbour ions. As a result of this the cations become fractionally more positively charged, and thus are attracted to the negatively charged vacancy. The magnitude of the relaxations are shown in Table 4.15.

Table 4.15: Inward displacement of shells of nearest-neighbour (NN) ions towards neutral silver vacancies in the silver halides / Å.

	1st-NN	2nd-NN	3rd-NN
AgCl	-0.09	+0.07	-0.04
AgBr	-0.14	+0.05	0.00

It should be noted that both spin density patterns show appreciable density on cations around the cell boundary. This is due to the close proximity of the image defects, and would disappear in the limit of infinite dilution. Indeed, we observe this effect in moving from the 63-ion to 215-ion AgCl supercells.

Previous experimental studies of the hole-vacancy complex in AgCl have suggested that the hole is centred on a *single* Jahn-Teller elongated lattice cation adjacent to the vacancy.[50,186] The difference in our distribution may be due to the localisation problem in DFT. Pacchioni *et al.* have recently found that the

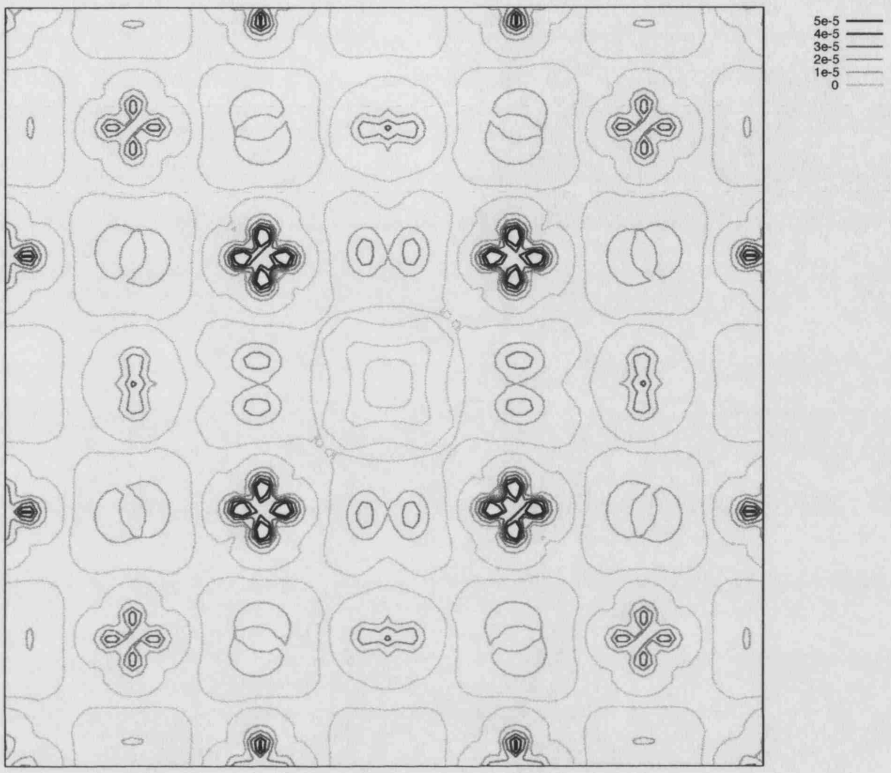

Figure 4.8: Spin localisation in defective AgCl: silver vacancy. Contour plot of a <100> plane in the larger 215-ion supercell containing the vacancy (centre).

hole in an α-quartz Al centre is incorrectly described by DFT.[187] Experiment and MP2 calculations showed localisation on a single oxygen site, while hybrid and pure DFT methods showed the hole to be delocalised over a number of oxygen ions. More recent hybrid functionals[188] have, however, managed to reproduce experimental behaviour.[189]

4.6.3 Anion Vacancies

The electronic properties of vacancies at anion sites are also of considerable interest. In the alkali halides, F-centres form, stabilising the excited electron.[59] It can be seen in Figures 4.10 and 4.11 that diffuse F-centres also form in AgCl and AgBr. However, the electron is largely located upon the nearest neighbour

Figure 4.9: Spin localisation in defective AgBr: silver vacancy. Contour plot of a <100> plane in the smaller 63-ion supercell containing the vacancy (centre).

cations, rather than being centred on the vacancy itself as in a conventional F-centre.

It can be seen from Table 4.16 that trapping of an electron causes the neighbouring silver ions to contract symmetrically into the vacancy by 0.70Å for AgCl. Again, the radial displacement of the other ions is small, which could, however, be due to the constraints imposed by the small size of the cell. When breaking the initial symmetry, the system relaxes back to the symmetrical geometry shown in the figure.

Table 4.16: Inward displacement of shells of nearest-neighbour (NN) ions towards neutral anion vacancies in the silver halides / Å.

	1st-NN	2nd-NN	3rd-NN
AgCl	+0.70	+0.08	0.01
AgBr	−0.02	+0.09	0.00

In the majority of systems studied previously,[59,131] the nearest neighbour cations to the vacancy expand outwards. The unusual cation contraction ob-

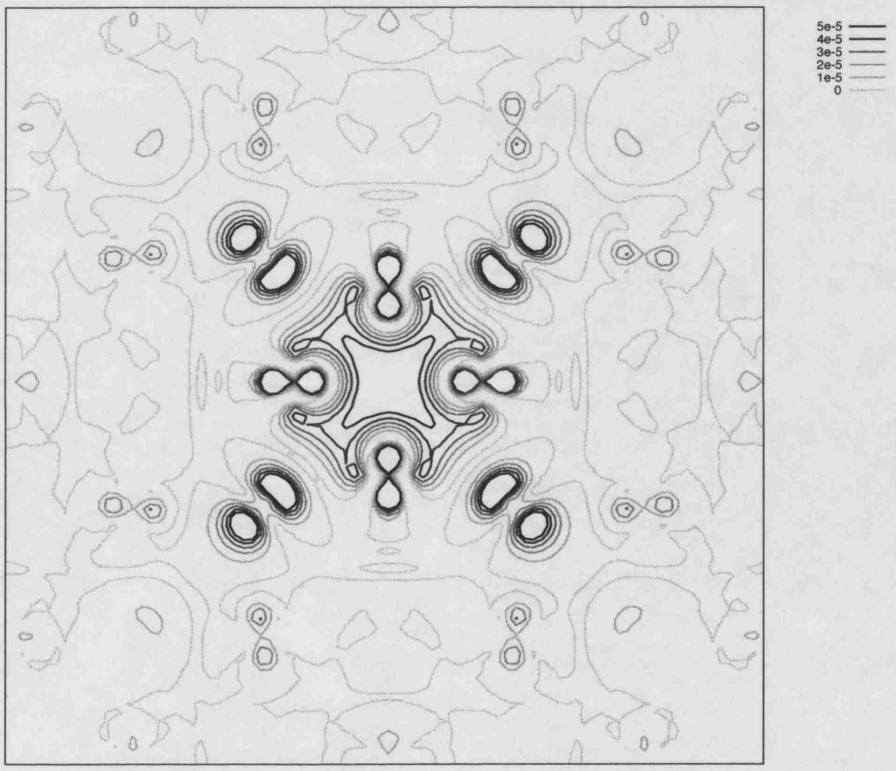

Figure 4.10: Spin localisation in defective AgCl: chlorine vacancy. Contour plot of a <100> plane in the larger 215-ion supercell containing the vacancy (centre).

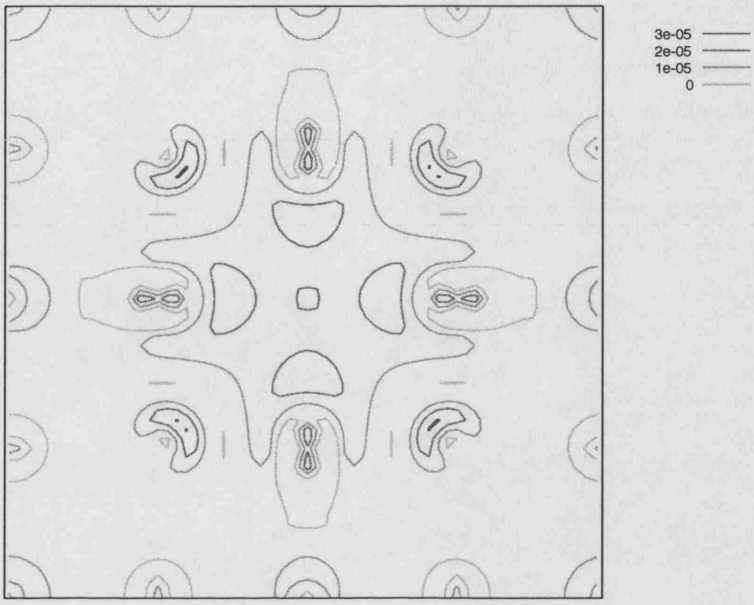

Figure 4.11: Spin localisation in defective AgBr: bromine vacancy. Contour plot of a <100> plane in the smaller 63-ion supercell containing the vacancy (centre).

served in our calculations therefore warranted further examination. As a test of the basis set used, we employed the DMol3 code[190] (which employs an atom-centred numerical basis) to repeat the calculation. We found the same structural relaxations as reported in Table 4.16 to within 4%, the difference being due to less stringent convergence criteria.

As a further test, we used our methodology to study a well known and extensively studied system. Sodium chloride (NaCl) was chosen owing to its apparent similarities to AgCl; being isostructural with a common anion, and lattice parameters that match to within 0.1Å. Using the same procedure as above we studied the F-centre, and found a well-localised electron contained within the vacancy (see Figure 4.12). We also observed small structural relaxations, with the nearest-neighbour cations moving outwards by 0.025Å. On removal of this trapped electron to form a charged defect, we find outward relaxation of the cations and inward relaxation of the nearest anions, consistent with the electrostatics and with magnitudes comparable with previous embedded-cluster calculations.[141]

Thus, we believe that our results for the silver halides are valid, and that

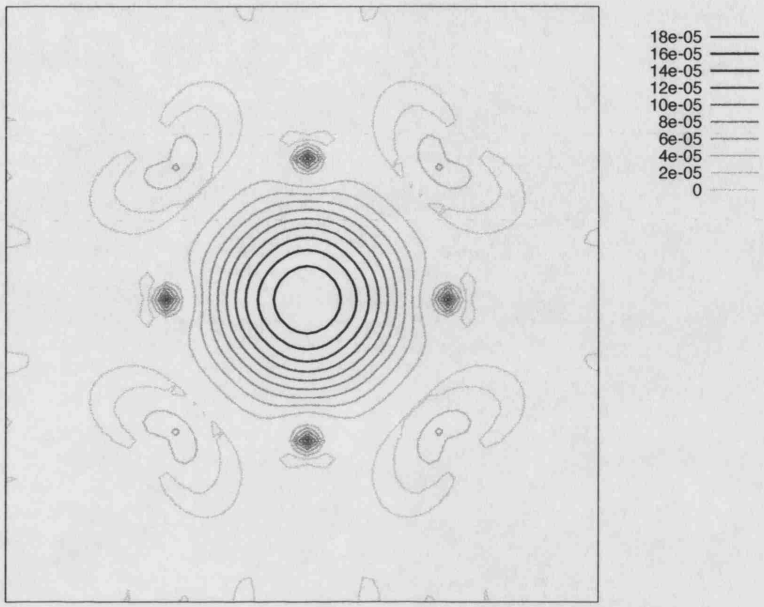

Figure 4.12: Spin localisation in defective NaCl: chloride vacancy (F-Centre). Contour plot of a <100> plane containing the vacancy (centre).

the unusual inward relaxation around the anion vacancy in AgCl can again be attributable to the complex nature of the bonding in this material.

4.7 Conclusions

When applying the supercell methodology, we have found the calculation of energies of formation of paired charged defects to be especially problematic. The spurious interactions between a defect and its images results in contributions to the energy that cannot be entirely removed using *a posteriori* correction factors. Within the plane wave methodology we are unaware of any existing schemes which address this problem. Consequently our only option is to increase the size of the supercell. However, the limits of current computational resources are reached rapidly.

Nevertheless, we have gained interesting structural information on the point defects, including the prediction of [111]-orientated split interstitial structure for the charged silver interstitial species. In addition, we have confirmed the presence of the neutral split-interstitial as predicted by Bennebroek *et al.* on the basis of

their ENDOR spectra.[61] We have also observed unusual relaxations around the vacancies, which we consider reflects the nature of the bonding in these materials.

With these calculations, we have gained interesting insights into the localisation of electrons and holes around these point defects. Although no quantitative comparisons could be made with experiment due to the small size of our models, we found good qualitative agreement between our calculations and Bennebroek's ENDOR work. In contrast, we find that our calculations incorrectly predict the localisation of the hole around the cation vacancy. The observed behaviour is, however, entirely consistent with other similar studies which have found that GGA-DFT tends to over-delocalise the hole state.

This chapter has shown that despite the limitations imposed by the choice of the plane wave basis set and supercell method, useful information can be obtained relating to intrinsic defects in the silver halides. In the following chapter, we extend this work to the important (100) surface using the hybrid QM/MM technique.

Chapter 5

QM/MM Embedding

As discussed in the Introduction, the defect properties of the silver halides are strongly influenced by the presence of a crystalline surface. Point defects on the important (100) surface have been studied here using the QM/MM embedding technique described in Chapter 2. The {111} surfaces have been omitted from this study due to the additional complexity involved in modelling polar surfaces.[72] However, their properties may be important in the understanding of modern photographic emulsions.

The calculations presented here are very demanding on computational resources, and consequently required extensive use of national terascale supercomputing facilities. Therefore we had to be selective in our calculations. While a direct comparison with the results of the previous chapter would have been desirable, we have chosen to concentrate our resources on surface properties for the reasons given above.

In the following section, we will provide a complete description of the two models used in this work: the semi-infinite model, and our 'nanocube'. We then proceed to describe the results we obtained from each model in turn.

5.1 Method

For this work the ChemShell code[140] was employed, which allows the coupling of a QM calculation to an MM calculation using a simple shell-script-like interface. For the calculations reported here, the quantum mechanical code GAMESS-UK[136] was used in combination with the semi-classical shell-model code GULP.[148]

A general description of the embedded cluster technique was provided in Chapter 2. The methods used for these calculations are detailed in this section.

5.1.1 Model

In this work, we used two models, both employing a self-consistent polarized embedding procedure. The first system was a semi-infinite surface, while the second consisted of a finite nano-particle (herein referred to as a 'nanocube').

The innermost regions of each model were identical, consisting of:

Region 1 Described fully quantum-mechanically

Region 2 Interface, described with full core pseudopotentials *and* interatomic potentials (cations only)

Region 3 Described using interatomic potentials (also included in QM Hamiltonian, as described in Section 2.6.2)

Where the models differed was in their description of the remainder of the system. The semi-infinite model, as its name suggests, attempted to replicate the effects of an infinite system using a computationally-tractable finite series of point charges (Figure 5.1). The nanocube, on the other hand, was an explicitly finite system (Figure 5.2).

Our initial calculations were performed using the semi-infinite model. However, it became apparent that the use of a finite cluster would have a number of advantages for the problems we were studying. Most importantly, it allowed the study of a range of surface and bulk-like sites within a single framework (e.g. terraces, kinks and steps). However, with this advantage came the disadvantage that we were modelling the properties of neither the idealised material, nor a fully realistic system. Instead, we were modelling a simplified system which should exhibit some of the key properties of the real crystallite.

5.1.2 Description of the QM region

Region 1 was described fully quantum-mechanically using the GAMESS-UK code,[136] and consisted of a cluster of 15-30 ions, depending on the geometry of the system.

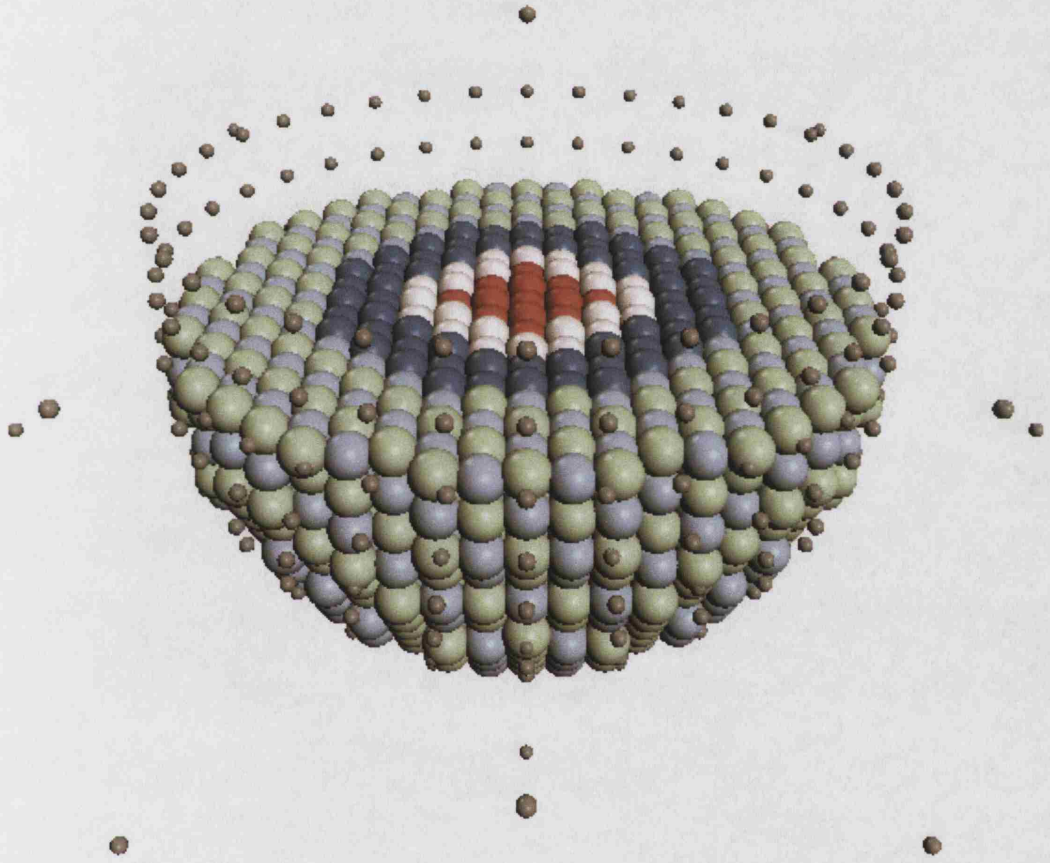

Figure 5.1: Illustration of the five-region model for the semi-infinite surface. Red ions correspond to those treated fully quantum-mechanically, white are those in the interface region, and dark blue corresponds to the relaxed MM region. The remainder of the hemisphere was composed of rigid MM ions. The point charges, reproducing the field of the infinite crystal, are shown in grey.

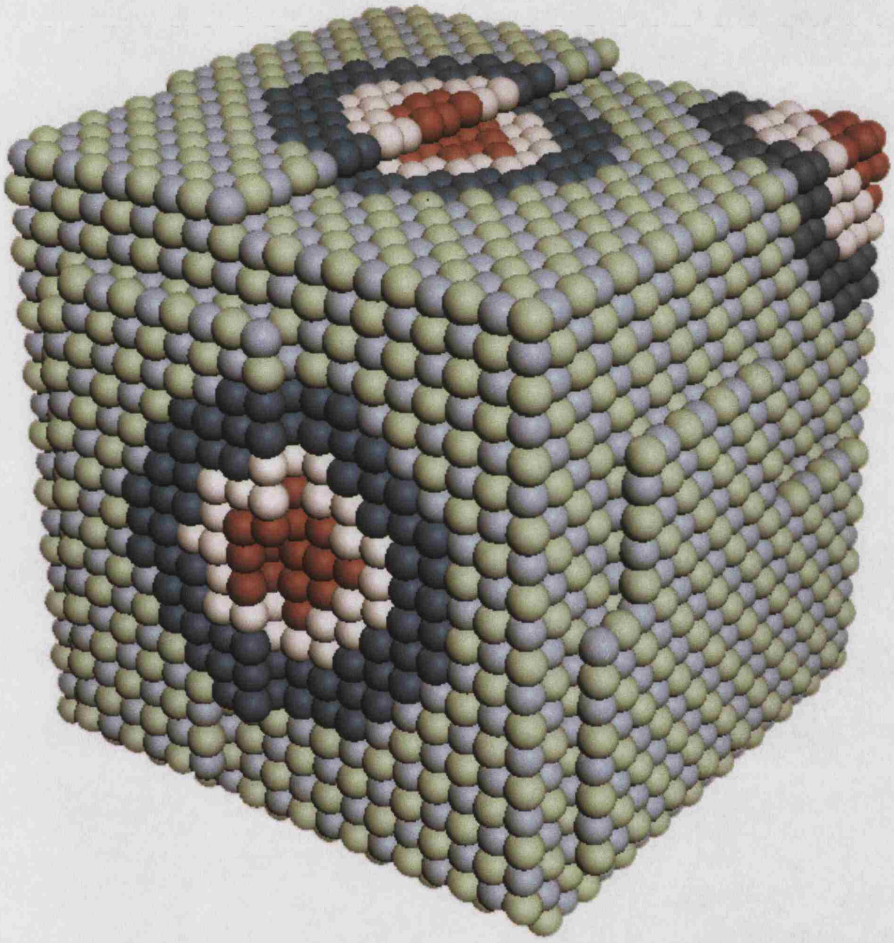

Figure 5.2: Illustration of the four-region model for the 'nanocube'. Highlighted are various choices of the QM region: positive kink [front left], step [top] and corner [top right]. Red ions correspond to those treated fully quantum-mechanically, white are those in the interface region, dark blue corresponds to the relaxed MM region, and the remainder of the nanocube was composed of rigid MM ions.

Table 5.1: Properties of relevant dimers calculated using GAMESS-UK, our custom basis set (see text), and a variety of functionals. Dissociation energies are in electron-volts, and bond lengths are in Angstroms.

	B97-2[128]	B97-1[126]	B3LYP[123]	Expt.[165]
$D_e(AgCl)$	3.308	3.327	3.032	3.239
$d(AgCl)$	2.319	2.326	2.330	2.281
$D_e(Ag_2)$	1.873	1.919	1.664	1.64
$d(Ag_2)$	2.571	2.576	2.580	2.53
$D_e(Cl_2)$	2.420	2.465	2.244	2.51
$d(Cl_2)$	2.012	2.032	2.042	1.99

Each ion was described with a TZVP-quality basis set, which were modified versions of the basis sets developed by Ahlrichs, in which the most diffuse functions were removed in order to prevent the instabilities in the SCF procedure that are often experienced when dealing with solid-state systems.[191] In addition, a small-core pseudopotential was placed on the silver ion,[192] which reduced computational load and took into account certain relativistic effects.

Hybrid functionals provide significantly better estimates of the band gap and lattice parameters than either pure Hartree Fock or pure DFT. Therefore, they should also reproduce the localisation of holes and electrons more accurately. The B97-2 hybrid DFT functional was employed for all calculations.[128] Our tests, reported in Table 5.1, have shown this functional to produce results that were significantly more accurate than both the B97-1[126] and the commonly used B3LYP[123] functionals.

5.1.3 Description of the Interface Region

The interface region existed to prevent mobile charge within Region 1 escaping towards positively charged centres in the outer regions. In the current implementation this was achieved by placing full-core pseudopotentials on the cations surrounding Region 1. Thus these centres appeared as structured positively-charged centres, but were not assigned basis functions and thus were unable to trap mobile charge.

Our calculations employed a customised version of the full-core pseudopoten-

tials of Stoll *et al.*,[193] in which we introduced a local component with an exponent manually adjusted such that the bond length of the AgCl dimer matched the value obtained using the small-core pseudopotential.

The possibility of having Region 2 anions is currently under investigation.[194] Progress has been limited, as current QM codes do not have the functionality to allow the use of full-core anion pseudopotentials, as this would be meaningless in most contexts.

In addition to the QM description of the ions in this region, each centre was assigned short-range interatomic potentials. In this way, the interactions within Region 2, and between Region 2 and Region 3 could be included.

The semi-infinite model described here has been used previously within our group to study the surfaces of catalytically-active metal oxide materials.[146,195] For these calculations, the oxygen anion was treated using the shell-model while the metal cation was treated as a rigid ion. Consequently, the code required some modifications in order to deal with shell-model cations within the interface region. As a first approximation, the small number of cations in this region were converted to rigid ions, removing the ambiguity of where to situate the pseudopotentials. These rigid ions interact with the shell-model ions in the adjacent Region 3 using our standard short-ranged interatomic potentials. This approximation appeared to work well, and so no further enhancements to the model were pursued.

5.1.4 Description of the MM region

Region 3 extended outwards from the defect cluster to create a hemisphere of radius 15Å. As reported in Chapter 3, we have derived a new set of interatomic potentials tailored to QM/MM embedding. A full description of their derivation can be found in Section 3.3.2, and the potentials are reported in Table 3.5.

The centres in this region were free to polarize as part of the self-consistent embedding procedure, and were also active in geometry optimisation calculations.

5.1.5 Description of the Remainder of the System

The shape of this region defines the difference between the semi-infinite model and the 'nanocube' structure. In each case, this region is present purely to provide a field for the inner regions, and remains static throughout the calculations.

In the semi-infinite surface model, we surrounded the inner regions by a hemispherical shell of static ions 26Å in radius (Region 4). The hemisphere containing all four regions was initially excised from an MM-relaxed surface slab. It was subsequently partitioned into the regions described above, and augmented by a series of point charges which were least-squares fitted to reproduce the electrostatic potential of the infinite system within the active (relaxed) region.

The ions in Region 4 experienced long-range electrostatic interactions with the inner regions, and due to their associated interatomic potentials, also had short-ranged interactions with Region 3. The point charges of Region 5 were placed at locations with spherical symmetry below the surface, and with cylindrical symmetry above the surface. In order to improve the fit of the electrostatic potential, additional charges were placed at large distances from the cluster (typically 100Å) whose rôle is to reproduce the multipole moments of the system. Additional details of this method have been described previously by Sokol *et al.*[146]

For our nanocube, the model is considerably simpler. Rather than being hemispherical, Region 4 comprised the entire remainder of the structure, as illustrated in Figure 5.2. External point charges were no longer required, as a finite system was being modelled.

The nanocube used in this work was created by hand from a cubic supercell of AgCl of edge 55Å. A variety of surface defects were created on its faces, and the entire system was relaxed using our interatomic potentials. Although artificially created and smaller-scale than a real grain (photographic films contain grains of size 50 - 1000 nm), our nanocube contained features that we would expect to find in a full-sized, annealed, system.

The rest of this chapter describes the results obtained using these two methods, starting with the semi-infinite model (Section 5.2), and later moving to the nanocube (Section 5.3).

5.2 Semi-Infinite Surfaces

In order to provide general results relating to the surface and its basic defects, initial calculations were performed using the semi-infinite model. Although extension of this model to study bulk defects would be straightforward, we had

limited computational resources and so this was not pursued.

5.2.1 The (100) Surface: Self-Embedding Test

In section 3.3.2, the 'rumpling' of the (100) surface layer was discussed. There, we proposed that the increased interionic spacings observed in the surface layers of the QM calculation were due to a reduction in hybridisation of the valence band. This behaviour was not observed using the simple shell-model interatomic potentials.

For all the calculations in this section our QM cluster consisted of 19 ions, arranged in a square pyramid, which was then surrounded by 32 Region 2 cations; a hemisphere of approximately 350 Region 3, and 1500 Region 4, shell-model ions; and around 250 point charges. Initially, our unrelaxed QM/MM cluster had surface properties inherited from the MM-relaxed slab. The magnitudes of the QM/MM relaxations upon geometry optimisation of this defect-free cluster therefore give a measure of the accuracy of the embedding model, and is known as the self-embedding test. Because of the known deficiencies of our interatomic potentials, we can expect the relaxations from the MM positions in the surface layers to be relatively large.

As can be seen in Figure 5.3, the characteristic rumpling effect is reproduced throughout all regions in our cross-section. Quantitative results are reported in Table 5.2. As would be expected, our QM/MM calculation show relaxations intermediate between the two extremes of the QM and MM calculations.

The discrepancies in the magnitudes of the surface relaxations have been shown to be a result of the failure of the MM potentials. However, there is little scope for their improvement while remaining within the current versions of the shell model. Our embedding calculations necessarily involve energy differences between two similar systems. As a result, small errors in the absolute positions of our MM ions are of reduced significance. We therefore believe that our model is satisfactory for the purposes here.

5.2.2 Surface Defects

Following the work in the previous chapter on structural defects within the bulk of the silver halides using the supercell model, we now wish to extend this study to the formation of individual point defects on the flat (100) surface of AgCl

Table 5.2: A comparison of surface rumpling using three codes. The CASTEP and MARVINS results are identical to those in Table 3.7, while the QM/MM values come from the central column of ions from two separate calculations, each having 19 'Region 1' ions arranged in an square pyramid. Values quoted are vertical displacements from the unrelaxed lattice-site positions / Å.

	MM: MARVINS		
	Ag-topped	Cl-topped	Average
Surface Layer	-0.18	+0.11	−0.04
Surface - 1	-0.07	+0.10	+0.02
Surface - 2	-0.03	+0.01	−0.01

	QM: CASTEP		
	Ag-topped	Cl-topped	Average
Surface Layer	+0.22	+0.42	+0.32
Surface - 1	+0.24	+0.33	+0.29
Surface - 2	+0.18	+0.22	+0.20

	QM/MM: ChemShell		
	Ag-topped	Cl-topped	Average
Surface Layer	-0.02	+0.17	+0.08
Surface - 1	-0.15	+0.04	−0.06
Surface - 2	-0.08	-0.14	−0.11

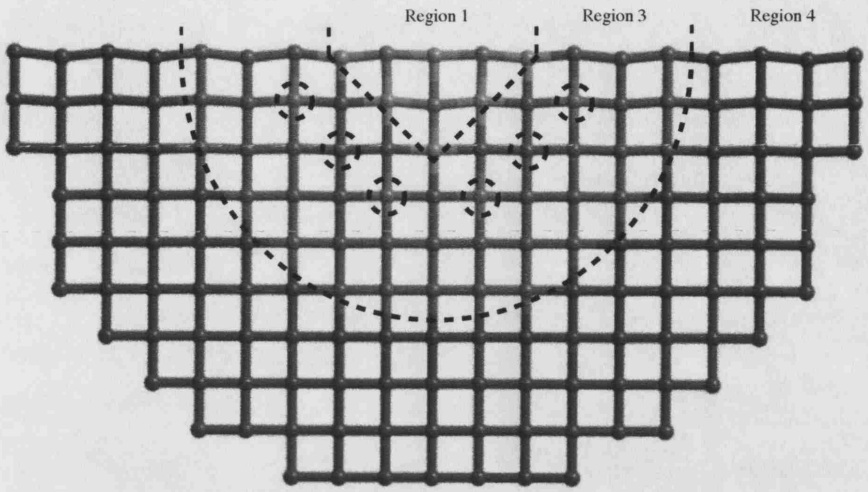

Figure 5.3: A slice through the cluster representing the (100) surface. The regions of the model are marked, with Region 2 ions identified using dashed circles. Region 5 has been been omitted for clarity.

using our QM/MM model. We used the same model as for the self-embedding test above, which included up to the third-nearest neighbour ions within Region 1. When studying vacancy defects, a 'ghost atom' (comprised of basis functions but no nucleus) was employed in order to reduce basis set superposition error.

At the surface of a material, defects need not be formed in charge-balancing pairs since the surface itself may become charged. The calculated defect formation energies, relative to isolated ions, were -3.52 eV, 4.39 eV and 4.68 eV for the Ag_I, V_{Ag} and V_{Cl} species respectively. Surface-layer Frenkel pairs therefore have a formation energy of 0.87 eV. Unfortunately, there are no experimental data with which to compare this value. However, due to the increased interatomic spacing near the surface, we would expect the defects to be formed more easily than in the bulk, where the experimentally-determined Frenkel energy is 1.49 eV (see Table 1.2).

5.2.3 Depths of Electron and Hole Traps

As we have described in the Introduction, knowledge of the processes of electron and hole trapping at defect sites is vitally important to the understanding of latent image formation. As well as knowing the defect concentrations, it is therefore desirable to know the positions of the electron traps relative to the conduction

Table 5.3: Positions of the defect levels at the (100) surface of AgCl, relative to the vacuum level. The valence band maximum is located at -7.63 eV, and the conduction band minimum is at -2.51 eV. All values are in electron-volts.

	Vertical	Relaxed	Stabilisation Energy
Ag_I	-3.26	-4.12	−0.86
V_{Ag}	-7.14	-6.69	+0.45
V_{Cl}	-1.69	-3.44	−1.75

band, and the hole traps relative to the valence band.

To calculate these quantities, we must determine the energy levels of the defects relative to a common reference energy, which is usually taken to be the vacuum level. In order to position the valence band we must calculate the vertical ionisation energy, while the conduction band may be obtained through calculation of the electron affinity. For our semi-infinite surface model we calculated a value for the band gap of 5.1 eV, which is in very good agreement with the experimental *direct* band gap for the bulk (see Table 1.1). This result would suggest that our 19-ion QM cluster is too small to reproduce the effects of the indirect band gap. However, a larger cluster was too expensive for the calculations here. Nevertheless, we have proceeded with the 19-ion cluster on the basis that the conduction band minimum is located at the gamma-point, and therefore should be well-described. For completeness we have calculated the properties of the states near the valence band, but they may be considered to be less accurate.

Figure 5.4 and Table 5.3 show the results of our calculations for point defects on the (100) surface. In the figure, solid lines represent the vertical trapping levels, while the dashed lines show the extent of stabilisation upon ionic relaxation. From the data, it is clear that the surface interstitial cation represents a good electron trap, and due to the relaxation processes described above, the electron would become deeply trapped. The unrelaxed F-centre represents a resonance state, as it is located within the conduction band. However, upon ionic relaxation, it becomes a stable, bound, neutral defect. Although there is uncertainty in the accuracy of the calculations, our results indicate that the surface silver vacancy is an efficient hole trap.

In the following section, the structural properties of each of the charged and neutral surface point defects will be discussed.

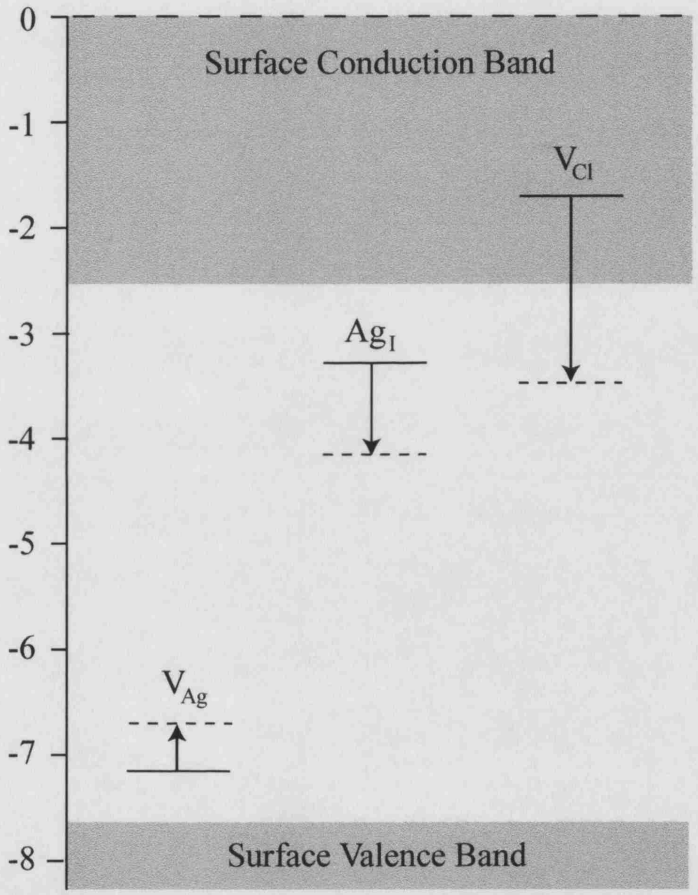

Figure 5.4: The depths of electron and hole traps at point defects on the (100) surface of AgCl. Dashed lines show the extent of further stabilisation upon ionic relaxation.

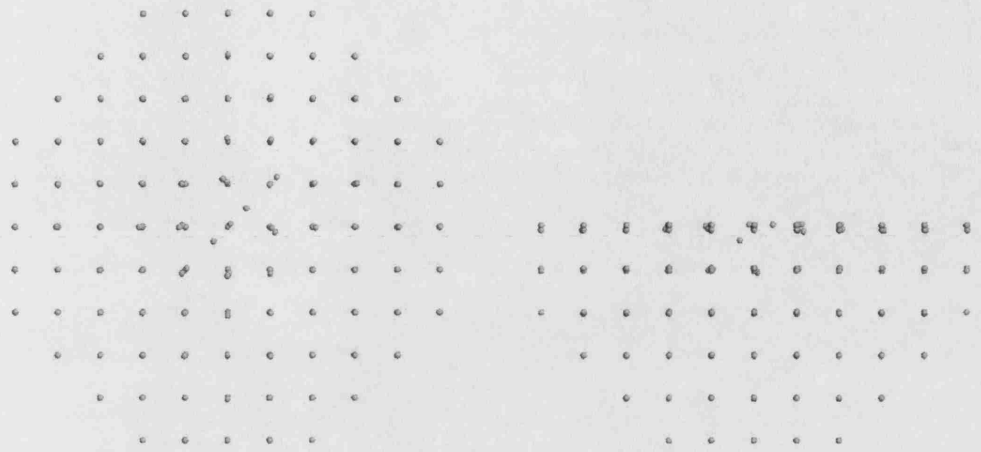

Figure 5.5: The structure of the charged interstitial defect on the (100) surface of AgCl. Plan view [left] and side view [right].

5.2.4 Structural Properties

Interstitial Cation

As for the bulk defects studied in Chapter 4, we find a split-interstitial structure to be of lower energy than a conventional body-centred geometry. Due to the lower coordination at the surface, the Ag_2^{2+} dimer is distorted from the [111] orientation into a flatter geometry with an angle of only 18.4° to the surface plane, as shown in Figure 5.5. There is also a corresponding increase in the dimer bond length to 3.17Å - an increase of 7% over the bulk value calculated using the CASTEP code in the previous chapter.

Due to the asymmetry of this split-interstitial species, with one ion protruding from the surface, the effects of electron trapping differ from the symmetrical bulk case. We observe that the electron initially localises upon the protruding cation, as can be seen in Figure 5.6. The electron then becomes stabilised through relaxation of the cation out of the plane of the surface, and as a result, the split-interstitial form is lost. The final geometry and localisation pattern are shown in Figure 5.7. It is interesting to note that the nearest neighbour cations displace such that a Ag_4 tetrahedron is formed (highlighted in Figure 5.7), which is indicative of covalent bonding. Indeed, in the spin density distribution we observed a small accumulation of density in the centre of the tetrahedron.

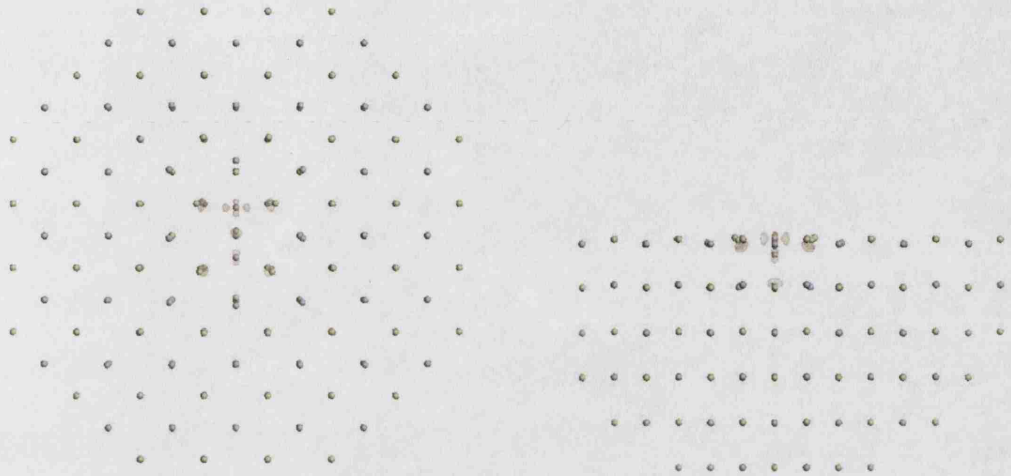

Figure 5.6: The localisation of the trapped electron on the interstitial defect on the (100) surface of AgCl before relaxation.

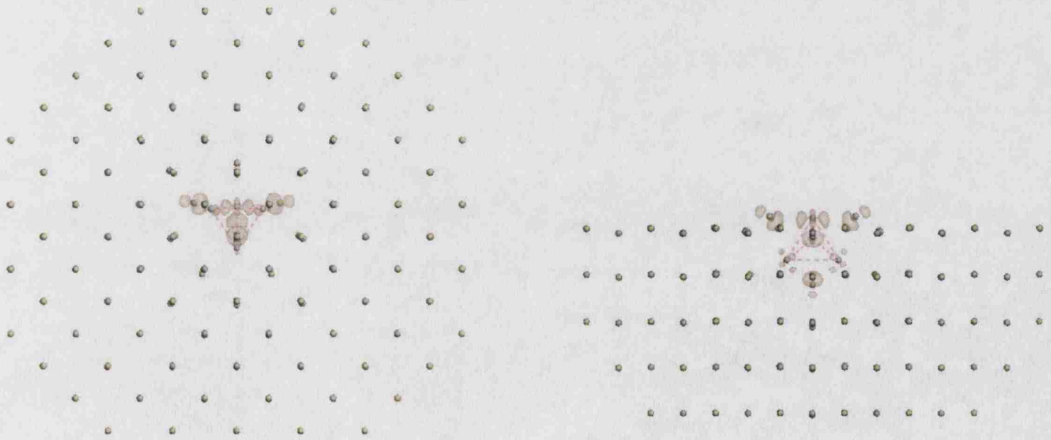

Figure 5.7: The localisation of the trapped electron on the interstitial defect on the (100) surface of AgCl after relaxation.

Figure 5.8: The localisation of the trapped hole next to a cation vacancy on the (100) surface of AgCl.

Cation Vacancy

The relaxation around the charged cation vacancy can be explained on simple electrostatic grounds, as was the case for the bulk defect. Here, the surface anions relaxed 0.42Å outwards, while the anion below the vacancy, whose vertical position is already strongly perturbed by the presence of the surface, relaxed 0.21Å downwards.

As can be seen in Figure 5.8, when a hole is present it strongly localised in the $4d_{x^2-y^2}$ orbital of a single cation located in a subsurface next-nearest-neighbour position to the vacancy. This behaviour is similar to that experimentally-determined for the bulk,[50] as discussed in Section 4.6, and supports our assumption that GGA-DFT was incorrectly describing our bulk system.

Eachus *et al.* have studied this system using a combination of EPR, ENDOR and *ab initio* calculations, and have suggested that the hole may be localised over four equivalent chloride ions on the surface layer.[186] However, they described inconsistencies in the results of their analysis and intended to perform additional experiments before providing a definitive assignment.

Anion Vacancy

Similar to the cation vacancy, but in contrast to our bulk results (Section 4.4), the relaxations around the anion vacancy were consistent with predictions based upon electrostatics, with the surface cations relaxing 0.26Å outwards, and the subsurface cation relaxing 0.34Å downwards. The difference is likely to be due to the reduced level of hybridisation in the surface layers, as discussed in Section

Figure 5.9: The localisation of the trapped electron on the (100) surface anion vacancy (F-centre). Plan view [left] and side view [right].

5.2.1.

For the neutral anion vacancy in the bulk (F-centre), we observed unusually large inward relaxations of the nearest-neighbour cations. The same behaviour was observed here, with relaxations of 0.63Å for the surface species, and 0.26Å for the subsurface cation. The observed localisation, shown in Figure 5.9, was remarkably similar to that obtained in our bulk calculations (Figure 4.10). The results here, which used a more accurate functional than our work in the previous chapter, give further credibility to these unusual findings. Again it should be emphasised that this centre is largely of technical and methodological interest, as it would not be present in great enough concentrations to be experimentally detectable.

5.2.5 Subsurface Defects

As described in the Introduction, the silver halides are known to have a surface space-charge layer. We have initially investigated the depth-dependence of the charged defect formation energies using the semi-infinite model down to a depth of two atomic layers. Our calculations were most accurate when the defect was in the centre of the cluster, when the description of the lattice polarization in the outer layers was optimal. Thus, the QM/MM cluster was redefined for each subsurface layer, as illustrated in Figure 5.10. In addition, two clusters were required for each layer: one cation-centred, one anion-centred.

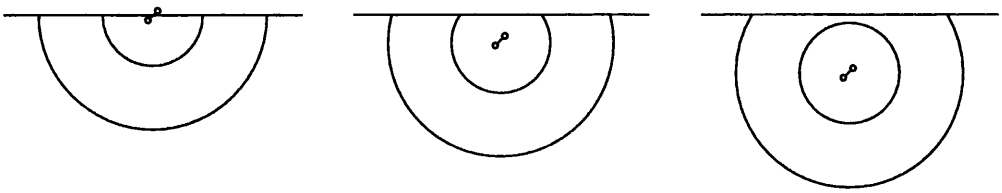

Figure 5.10: Illustration of the variation of the QM/MM cluster from the surface through to the second subsurface layer.

The energies of point defect formation, relative to isolated ions, at two depths are shown in Table 5.4, along with the surface-layer results from the previous section. The data follow smooth trends with the exception of the interstitial cation, where we believe that the additional relaxation of the surface-layer defect, as described above, stabilises this species. Hence, we suggest that the interstitial cations and anion vacancies are most stable at bulk, or bulk-like, sites. Conversely, cation vacancies are most stable at surface sites. This is consistent with experimental measurements of a negative surface potential for the (100) surface of AgCl,[77,78] and is similar to the semi-classical results of Baetzold *et al.* for AgBr.[72]

Table 5.4: Charged point defect formation energies for the surface and two subsurface layers / eV.

	Ag_I	V_{Ag}	V_{Cl}
Surface	-3.52	4.39	4.68
Surface - 1	-3.42	4.44	4.37
Surface - 2	-3.47	4.64	4.21

From these calculations, we would expect a large concentration of cation vacancies, with a compensating subsurface concentration of cation interstitial defects. We can therefore consider the surface silver vacancy to be the dominant hole trapping centre in microcrystalline AgCl crystals, in agreement with Eachus *et al.*[186] However, due to its low concentration, we would not expect the surface interstitial cation to be an important trapping centre.

5.3 Nanocube Calculations

The remainder of this chapter deals with calculations performed using the nanocube structure, described previously, and illustrated in Figure 5.2. Using this technique, the results from the semi-infinite model were extended so that they compare the formation energies and trap depths at a variety of surface sites. The results of these calculations are reported in the following sections.

5.3.1 Surface Point Defect Formation Energies

In order to understand the relative abundance of our surface point defects, we have calculated the energies of formation, relative to isolated ions, of defects at a variety of locations on the surface of our nanocube. Additionally, we have studied point defect formation at the centre of our model system, at sites which have an electrostatic potential within 3% of bulk values, and should therefore have bulk-like properties. Anion defects have been neglected as the calculations would require a large amount of computer time, and yet they are not thought to play a significant rôle in latent image formation.

Table 5.5: Charged point defect formation energies at various sites on the nanocube / eV.

	Ag_I	V_{Ag}
Flat (100)	-3.52	4.62
Bulk-like	-3.91	4.91
Step	-3.79	5.23
Positive Kink	-3.37	5.25

Our calculated defect energies are reported in Table 5.5. By comparing our new data for the flat surface with values from the semi-infinite model (Table 5.4), we can see that the approximations inherent to the nanocube model do not affect the formation energies strongly. If we therefore consider the defect formation energies from our bulk-like cluster as part of the series in Table 5.4, they can be seen to be consistent with the trends described, and support our assumption that interstitial cations are most stable at bulk sites.

The atomic structures of our bulk-like defects were largely the same as found in the previous chapter. However, we observed significant relaxations around

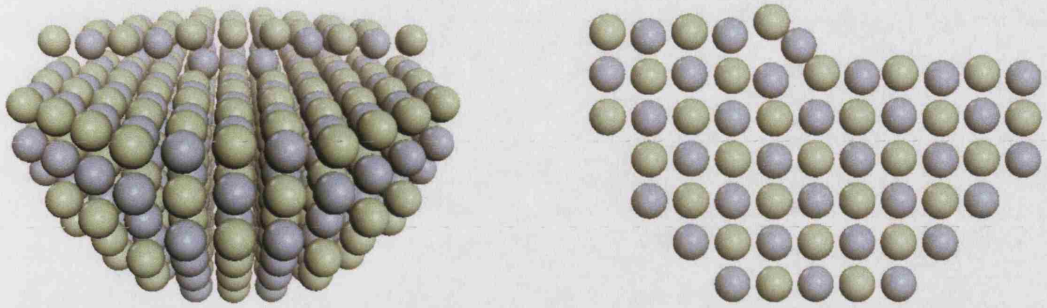

Figure 5.11: A step on the (100) surface of AgCl with a cation vacancy [left] and interstitial [right].

each defect, extending for many more shells of ions than were present within the confines of our supercells. As a result, our Ag_2^{2+} species elongated by 3% to 3.05 Å, with corresponding expansions in the distances to the nearest-neighbour ions. Similarly, the anions adjacent to the cation vacancy relax 0.35 Å outwards, compared to only 0.11 Å in the supercell calculations, due to the removal of the constraints of periodicity.

We have found the formation of point defects on extended defects, such as steps and kinks, to be energetically unfavourable compared to the sites previously discussed. The formation of a cation vacancy along a step edge was found to require considerably more energy than formation on the flat surface due to the creation of sites of very low coordination. As can be seen in Figure 5.11, formation of the cation vacancy was accompanied by considerable structural relaxation of the 3-coordinate nearest-neighbour anions, which can be accounted for by simple electrostatics. The case of the interstitial ion at a step is interesting because it was found to be more stable there than on the flat face. At first sight, the atomic structure was unusual, as the interstitial ion was at its lowest energy when located midway between two chloride ions at the step edge (see the slice in Figure 5.11 [right]). However, this site minimises interaction with the exposed cations along the edge of the step.

As described in the Introduction, the positive kink on the (100) surface is thought to play a key rôle in latent image formation, as it provides a site for growth of the silver cluster. These processes have been studied previously,[86,88–90] but to our knowledge have always assumed little structural relaxation of the kink itself. In contrast, we found that the silver cation on the corner of the kink site

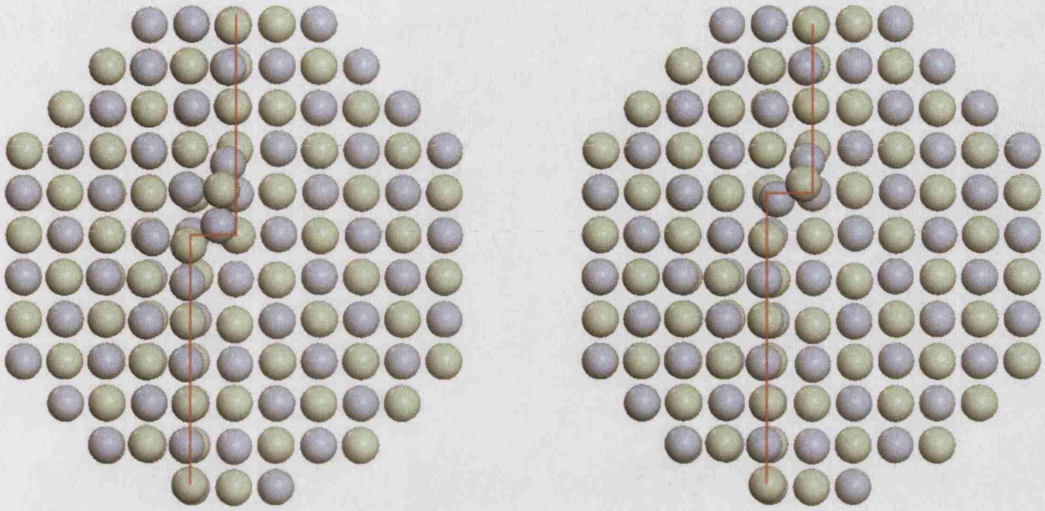

Figure 5.12: Structural relaxation of the positive kink [left] and negative kink [right].

rose out of the surface so as to minimise its interaction with its cation neighbours, as can be seen in Figure 5.12.

We also considered the negative kink, which for the purposes of Table 5.5, was considered to be cation vacancy on a positive kink. Here we see very similar structural relaxations to those described for the positive kink.

5.3.2 Electron and Hole Trapping

As for the semi-infinite model, we can calculate the trap-depths of various centres located on the surface or in the interior of our nanocube. Unlike in the previous section, we now have sites of low coordination that can also trap holes and electrons, such as kinks and corners. Indeed, the trapping of an electron at a positive kink site is one of the fundamental tenets of the direct photolysis mechanism (as described in Section 1.2.1).

Additionally, we may use the present method to provide a comparison with the results of the neutral defects from the previous chapter. As reported in Section 4.6.2, the choice of a method employing GGA-DFT and periodic boundary conditions for the study of spin localisation presented two issues: the self-interaction error lead to an over-delocalised spin density, and the defect images perturbed the localisation pattern leading to artefacts. Here, we have employed a more

accurate hybrid functional which should reduce the effects of the self-interaction error and improve the reproduction of the band gap. However, we must remember that with the size of our QM clusters, it is unlikely that our description of the electronic structure adequately reproduces the hybridisation of the valence band.

Figure 5.13 and Table 5.6 show the results of our calculations. It is clear that both the cation interstitial species and the positive kink site provide good electron traps, while the cation vacancies provide good traps for free holes. Interestingly, from a simple comparison of the positions of the valence band edges, we found that a hole in the valence band is considerably more stable within the bulk of the crystal, which can simply be ascribed to the reduced hybridisation at the surface, which results in less spreading of the energy levels in the valence band, and therefore a lower valence band maximum.

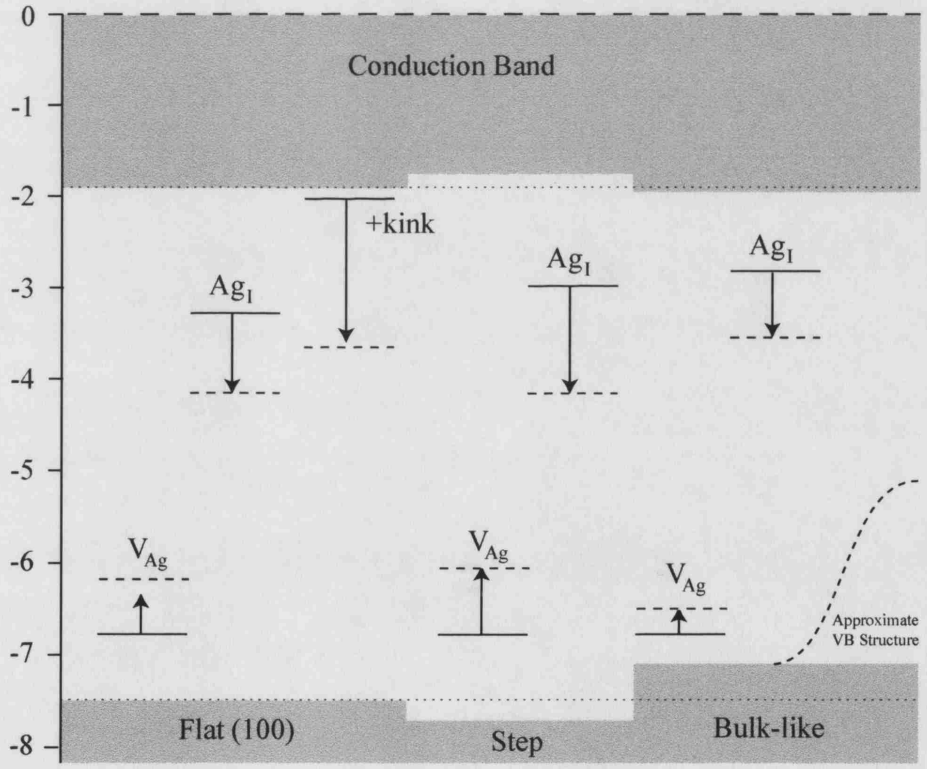

Figure 5.13: The depths of electron and hole traps at point defects on the nanocube. Dashed lines show the extent of further stabilisation upon ionic relaxation. The approximate position of the bulk valence band maximum has also been included for reference.

Table 5.6: Positions of the defect levels below the vacuum level for three regions of the nanocube. The position of the valence band maximum (VBM) and conduction band minimum (CBM) are included in the table for reference. Both vertical (v) and relaxed (r) defect levels are reported. All values are in electron-volts.

	VBM	CBM	$Ag_I(v)$	$Ag_I(r)$	$V_{Ag}(v)$	$V_{Ag}(r)$
Flat	1.90	7.47	3.24	4.12	6.76	6.18
Bulk	1.96	7.09	2.84	3.53	6.78	6.48
Step	1.75	7.71	2.98	4.33	6.76	6.05

Electron Trapping Centres

In keeping with the results from the semi-infinite model, we found that the interstitial cation provides an efficient electron trap, both at the surface and at the other sites studied, and that this ability depended only weakly upon the location of the defect, as can be seen in Figure 5.13. The distribution of an electron at an interstitial defect within the bulk is reported in Figure 5.14. The electron localisation observed for the defect on the flat surface was identical to that reported in Section 5.2.4, so will not be replicated here.

For the bulk defect, we found the electron to localise largely upon the same p-like polarization functions, as we saw using the supercell method (Figure 4.6). However, in these calculations, we observed a greater degree of localisation, with density accumulating between the two ions forming a partially-covalent bond, accounting for the 12% reduction of the Ag_2 bond length to 2.70Å. This result is in contrast to the supercell results which saw little localisation, and hence little change in ionic separation. We consider that the current approach is more accurate owing to the use of an hybrid functional, as this has been shown to be important in predicting localisation properties in similar systems.[185]

We have also found that the positive kink on the (100) surface will trap an electron, as it is positioned only slightly below the vacuum level at -2.02eV (see Figure 5.13). Upon capture of the electron, a very strong reconstruction occurs, stabilising the centre by 1.6 eV. From Figure 5.15, it can be seen that the result is a bound tetrahedral cluster of silver ions equally sharing the excess electron, which is similar to the behaviour discussed for the trapped electron at a surface interstitial defect in Section 5.2.4, but is more pronounced in this case.

This stabilisation mechanism has not been observed before. Fundamental to

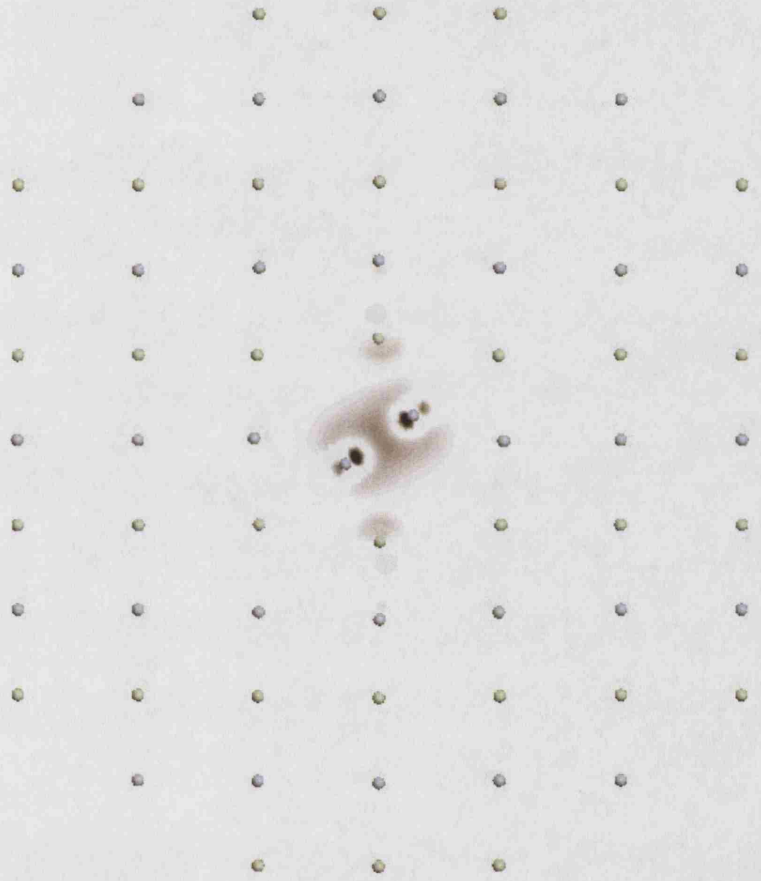

Figure 5.14: Spin distribution of a trapped electron at an interstitial ion in the bulk: slice through the (110) plane.

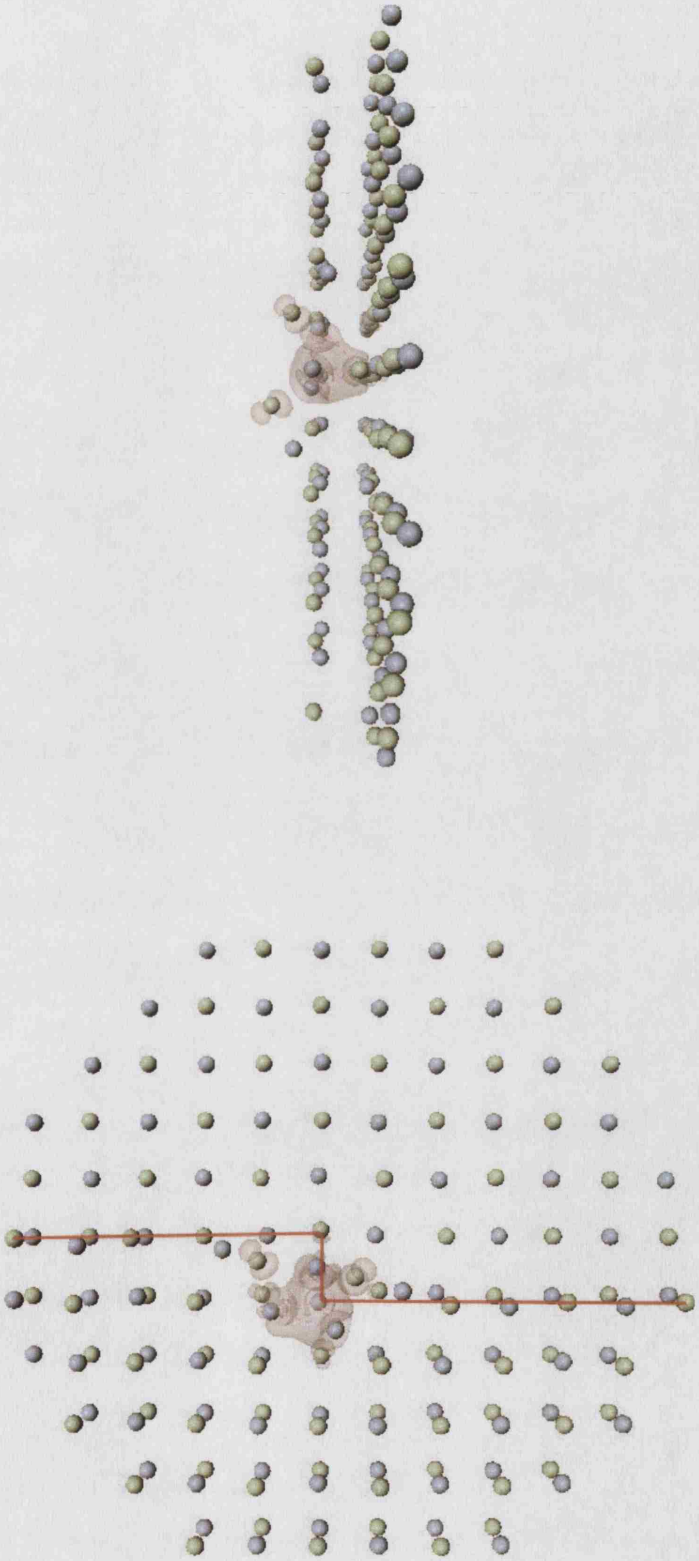

Figure 5.15: Structural relaxation and spin distribution of an electron trapped at a positive kink site on the (100) surface of AgCl. The tetrahedral geometry of the cluster of silver ions described in the text is highlighted in pink.

Mitchell's photo-aggregation model is the suggestion that the positive kink would not trap an electron deeply enough to provide sufficient time for the migrating interstitial cations to reach the surface.[95] However, our calculations show that this process can indeed occur, and thus we can further corroborate this crucial aspect of the direct photolysis mechanism.

Also worthy of discussion is the rôle of corner sites, as these are sites of low coordination, and have been shown to trap electrons in other materials.[141] We have found that the silver-tipped corner is a resonance state, but will relax to form a stable defect, much like the case of the anion vacancy. However, we must be aware that the number of these defects is necessarily small, and thus they are not thought to play a significant rôle in electron trapping.

In order to determine the most likely trapping site, we must consider the trap depths reported here along with the defect concentrations. Experimental studies of the (100) surface suggested that the concentration of positive kink sites is high, while studies of the space-charge layer found that the concentration of surface interstitial defects was low. We therefore predict, in line with the direct photolysis mechanism, that positive kinks are the dominant surface electron trap. However, our results do not preclude trapping of electrons at bulk cation interstitial defects.

Hole Trapping Centres

From Table 5.5 and Figure 5.15, we would expect the dominant hole-traps in microcrystalline silver chloride to be silver vacancies either in the bulk or at the flat (100) surface. Figure 5.16 shows the spin density distribution of the hole around the cation vacancy in the bulk and at a step on the flat surface. Again, the distribution for the hole at the vacancy on the flat (100) surface was identical to that described in Section 5.2.4, so will not be replicated here.

The localisation of the hole at a vacancy in the bulk shows a distinct axial symmetry, with a single mirror plane. The hole is localised on two cations at [2,0,0] and [-2,0,0], and four cations at [1,1,0], [1,-1,0], [-1,1,0] and [-1,-1,0], as can be seen in Figure 5.16. This unusual distribution may represent a local minimum in the energy surface. More likely, is that the hole is most stable at a [2,0,0] position, but cannot fully localise there due to the small size of our QM cluster. Therefore we treat this result as suspicious, and expect the true ground state to consist of a hole localised on a single cation, as seen for the surface cation

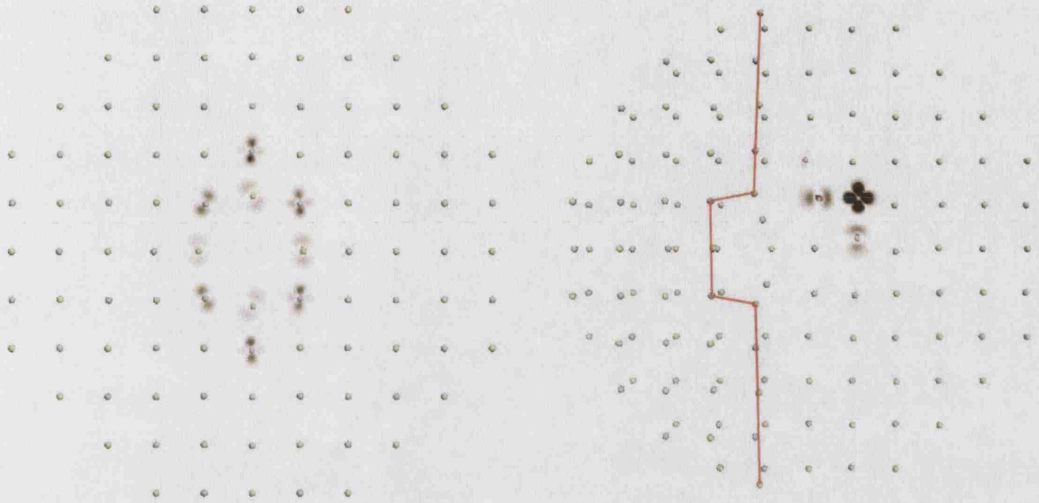

Figure 5.16: A trapped hole close to a cation vacancy in the bulk [left] and on the edge of a step [right].

vacancy (Section 5.2.4), and for the vacancy on the step (Figure 5.16 [right]). As predicted, this result contrasts with the delocalised hole from the previous chapter (Section 4.6.2), calculated using a pure GGA functional.

From the results here it is clear that the site at which the hole is most likely to trap depends on the size of the crystallite. For large crystals, we would expect free holes to migrate towards the bulk due to its valence band structure, where they could trap at bulk cation vacancies. However, for small crystallites, the increased cation vacancy concentration due to the space-charge layer is likely to offset this effect, and thus holes will trap at the surface.

5.3.3 Latent Pre-image Centre

The final component of our study involves extending our calculations to model a system that has direct relevance to latent image formation. Thus far we have modelled electron trapping at a positive kink site on the (100) surface of AgCl. According to the direct photolysis theory, a subsurface interstitial cation would then migrate towards the trapped electron until they recombine, forming a silver atom at the kink site. This atom is known as the latent pre-image centre (see Section 1.2 for more details). We have studied the structure and properties of this centre, and the results are reported in Figure 5.17.

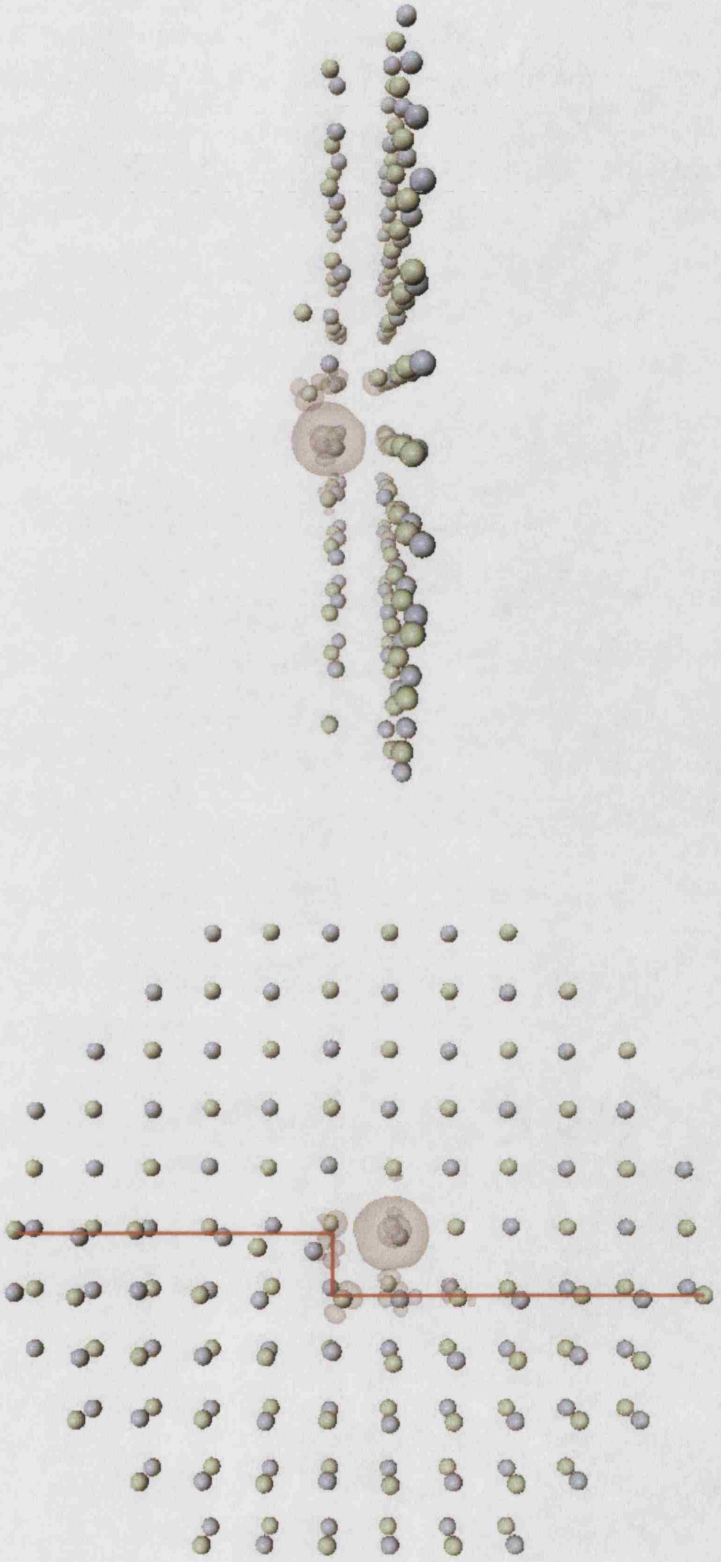

Figure 5.17: Structural relaxation and spin distribution of the latent pre-image centre at a positive kink site on the (100) surface of AgCl.

As can be seen in the figure, the electron preferentially localised in the silver ion's 5*s* orbital. This is not surprising given that this site has a positive electrostatic potential. Without further calculations, which could not be performed due to lack of resources, we can only speculate about the process of formation of this centre. However, we can envisage a process by which a subsurface interstitial cation migrates towards the electron trapped at the positive kink (Figure 5.15), whereupon an ion would be forced from the Ag_4 tetrahedron into a site surrounding the positive kink. Depending upon the electrostatic potential at its new location, the trapped electron may localise more strongly upon the ejected cation, and the system would relax to the stable configuration shown in Figure 5.17. From here, the centre may grow or decay according to the mechanisms proposed in the literature.

5.4 Conclusions

We have shown in this chapter that QM/MM embedding is a very effective tool for studying defects in the silver halides. We have employed two model systems in this work: a semi-infinite surface, and a finite nano-cluster which we assume reflects the properties of a realistic photographic crystallite.

With the former model, we have been able to study the structures and energetics of point defects on the (100) surface of AgCl. We have also calculated the properties of these intrinsic hole and electron traps. Furthermore, we have been able to characterise the space-charge layer, known to be present in the silver halides.

Using our novel nanocube structure, we have been able to extend this work to study the properties of point defects on and around surface defects such as steps and kinks. From this work, we have been able to characterise the most likely intrinsic electron and hole traps in silver chloride.

Finally, we have also been able to speculate on the formation processes of the latent pre-image centre - a key stage in latent image formation.

Chapter 6

Discussion

In this thesis, we have described our work on three broad categories of problems relating to the silver halides: charged point defects, neutral point defects, and photographically-relevant centres on the (100) surface. These systems were studied using a mixture of the supercell technique and the hybrid QM/MM approach, each of which had its own advantages for problems of this type.

Initially we investigated the possibility of using semi-classical interatomic potentials for some of this work. However, it quickly became apparent that the silver halides represent materials that are very difficult to model in this fashion, mainly due to their unusual valence band structure. Thus, the use of the method was confined to the QM/MM study reported in Chapter 5, where its inaccuracies were far less critical. The bulk of this work therefore employed density functional theory, which provides an excellent balance between accuracy with numerical efficiency.

As well as gaining important new insights into the silver halides, our work can also be treated as a methodological study. In this final chapter we will therefore discuss both the conclusions pertaining to the silver halides, and those pertaining to the methods used.

Charged Defects

In our investigation into the structures and energetics of charged point defects in the silver halides, we initially employed the supercell method. We found that the unwanted effects of periodicity could, to a certain extent, be reduced by *a posteriori* application of both the monopole-monopole and monopole-quadrupole

correction terms. However, errors in the electrostatic potential of the cell resulted in incorrect energies, which caused the defect-pair formation energies to be systematically too low by around 1 eV for a 64-ion supercell. While methods have been developed to circumvent this problem, to our knowledge, none of them are applicable for use with a plane wave basis set. We employed a larger 216-ion supercell for a number of key calculations, but found that the improvement in our energetics was not substantial, and thus we concluded that the use of this method was not appropriate for the calculation of these properties. However, due to the nature of the calculations involved, we believe that the structural properties we obtained were correct.

We also employed the hybrid QM/MM approach to study a similar set of problems. Due to the expense of these calculations, and therefore the need to be selective, we did not investigate the idealised bulk defects. However, using our novel nanocube structure, we did calculate the properties of charged defects in bulk-like positions, and at a variety of surface sites, using an accurate hybrid functional. This model not only freed us of the spurious defect-defect interactions, but also allowed us to relax many more shells of neighbouring ions - the effects of which are particularly important when modelling charged defects. The drawback of this method is that its ability to reproduce long-ranged modulations in the electron density is limited by the size of the QM cluster, an effect which is especially important for indirect band gap materials such as silver chloride. In contrast, these effects can be included routinely in periodic calculations using a representative set of k-points.

This combination of two complementary techniques has given us insights into the properties of bulk and surface point defects. We have predicted that the interstitial cation adopts a split-interstitial configuration both in the bulk and at the (100) surface. We have also quantified the extent of the relaxations around the vacancies. Despite our concerns over the energetics from these models, we successfully predict the dominance of the Frenkel defect pair. Through calculation of the depth-dependence of the point defect formation energies we have also verified the existence of the space-charge layer in AgCl.

Neutral Defects

We have used the same two techniques to study neutral defects, in which an electron or hole is trapped in or around the charged defect. Of fundamental relevance to the processes of latent image formation are the positions of the defect levels within the band gap, as these determine the trapping probabilities of the centres, and hence the fate of the free electron/hole pair. From a fundamental perspective, we were also interested in the structural forms of these defects and the distribution of the trapped species.

With the supercell approach, many of the limitations described previously for charged defects were removed. The primary interaction between a neutral defect and its periodic neighbours is of quadrupole-quadrupole origin, which decreases as L^{-5}, and was thus neglected in this study. The electrostatic potential in the cell was also far more accurate, leading to much better formation energies. However, new limitations were introduced, such as the ability of the supercell to enclose the spin density distribution. Although not intrinsic to the method, the primary factor affecting the accuracy of these calculations was the use of a GGA functional, which has previously been shown to over-delocalise the distribution of trapped electrons and holes and also significantly underestimates the band gap. However, hybrid functionals have recently been implemented in the CASTEP code, promising improvements in these properties for future calculations.

The use of QM/MM techniques for these problems suffer the same limitations as for the charged defects, in that use of a 'small' cluster may affect the ability of the calculation to reproduce an indirect band gap. Additionally, we must be aware that we cannot model extended delocalised states such as a free electron in the conduction band or a free hole in the valence band.

Nevertheless, we have obtained meaningful results using these techniques. We have shown that the cation vacancy will trap a hole in a $4d$ orbital of an adjacent cation. In line with recent work on other systems, this result required the use of an accurate hybrid functional, otherwise a more delocalised state was observed. The interstitial cation was found to trap an electron, and retain its split-interstitial configuration in the bulk, in agreement with experiment. At the (100) surface, the electron predominantly localised on a single cation, drawing it further out of the surface plane. The anion vacancy F-centre is stable in the bulk and at the surface, and exhibited unusually-large inward relaxations of the surrounding

cations. However, this neutral centre will have a negligible concentration as the charged anion vacancy is itself relatively rare.

Photographically-Relevant Centres

In addition to the intrinsic point defects described above, we have also studied the properties of a number of systems which are thought to be relevant to the formation of a latent image. These calculations made use of a novel finite nanocluster which consisted of a cube of edge 55Å, with surfaces exhibiting important structural features. Although smaller than a realistic photographic crystallite, we assume that the properties calculated for our system are representative of reality.

The most significant of these is the positive kink site on the (100) surface. A number of previous studies have investigated the growth of the latent image cluster. However, to our knowledge, the properties of the 'bare' site have not been reported. In our calculations, we observed relaxation of the corner cation out of the surface in order to minimise its interaction with nearby cations. In agreement with experiment, and the direct photolysis mechanism, we predicted that this centre will trap an electron. On doing so, it underwent significant relaxation, resulting in a covalently-bound tetrahedral cluster of cations, and effect which has not been observed before, and which explains the stability of the electron at this site.

We have also calculated the properties of the latent pre-image centre, which we have confirmed to consist of a single silver atom located at a positive kink. This centre is not developable, and is thought to form and decay a number of times before growing to a stable, developable, size. Finally, given our findings, we speculated about the formation processes of the pre-image centre.

Conclusions

We have shown that with these two complementary computational techniques, we can achieve a greater degree of understanding about the silver halides, and their rôle in latent image formation. We have also shown that each method has its drawbacks and merits, and that a combined approach is the only way of determining defect properties accurately.

With this work , we have shed light upon the defect properties of the rocksalt-structured silver halides, including the structures, energetics and trapping be-

haviours. These results, in combination with our studies of the surface positive kink site, have provided new insight into the processes behind latent image formation.

Appendix A

The Interaction Between Two Charged Polarizable Ions

Analytical Result

The potential at point 2, due to ion 1 is,

$$\phi_2 = \frac{q_1}{r_{12}} + \frac{\vec{r_{12}} \cdot \vec{p_1}}{r_{12}^3}, \tag{A.1}$$

and therefore the electric field is:

$$\vec{E_2} = -\nabla\phi_2 = \frac{q_1}{r_{12}^2}\vec{n_{12}} + \frac{3\vec{r_{12}}(\vec{p_1} \cdot \vec{r_{12}})}{r_{12}^5} - \frac{\vec{p_1}}{r_{12}^3}. \tag{A.2}$$

Realising that $\vec{p_1}$ must be along $\vec{n_{12}}$ leads to the relations: $\vec{p_1} = p_1\vec{n_{12}}$, and $\vec{p_1} \cdot \vec{r_{12}} = p_1 r$, and so the electric field can be written:

$$\vec{E_2} = \frac{q_1}{r^2}\vec{n_{12}} + \frac{2p_1}{r^3}\vec{n_{12}}. \tag{A.3}$$

Similarly, defining p_2 as $\vec{p_2} = p_2\vec{n_{12}}$ leads to:

$$\vec{E_1} = -\frac{q_2}{r^2}\vec{n_{12}} + \frac{2p_2}{r^3}\vec{n_{12}}, \tag{A.4}$$

and hence the polarizabilities:

$$\vec{p_2} = \alpha_2\vec{E_2} = \left(\frac{\alpha_2 q_1}{r^2} + \frac{2\alpha_2 p_1}{r^3}\right)\vec{n_{12}}, \tag{A.5}$$

$$\vec{p_1} = \alpha_1 \vec{E_1} = \left(-\frac{\alpha_1 q_2}{r^2} + \frac{2\alpha_1 p_2}{r^3} \right) \vec{n_{12}}. \tag{A.6}$$

Substituting and rearranging results in:

$$\vec{p_2} = \alpha_2 r \left(\frac{q_1 r^3 - 2\alpha_1 q_2}{r^6 - 4\alpha_1 \alpha_2} \right) \vec{n_{12}}, \tag{A.7}$$

$$\vec{p_1} = -\alpha_1 r \left(\frac{q_2 r^3 - 2\alpha_2 q_1}{r^6 - 4\alpha_1 \alpha_2} \right) \vec{n_{12}}. \tag{A.8}$$

An expression for the work done can then be obtained:

$$\begin{aligned} W &= q_2\phi_2 - p_2 E_2 \\ &= \frac{q_1 q_2}{r} + \frac{q_2 p_1}{r^2} - \frac{1}{\alpha_2} p_2^2 \\ &= \frac{q_1 q_2}{r} - \frac{q_2 \alpha_1}{r} \left(\frac{q_2 r^3 - 2\alpha_2 q_1}{r^6 - 4\alpha_1 \alpha_2} \right) - \alpha_2 r^2 \left(\frac{q_2 r^3 - 2\alpha_2 q_1}{r^6 - 4\alpha_1 \alpha_2} \right)^2 \end{aligned} \tag{A.9}$$

For identical species $q_1 = q_2 = q$, $\alpha_1 = \alpha_2 = \alpha$:

$$W = \frac{q^2}{r} - \frac{q\alpha}{r} \left(\frac{qr^3 - 2\alpha q}{r^6 - 4\alpha^2} \right) - \alpha r^2 \left(\frac{qr^3 - 2\alpha q}{r^6 - 4\alpha^2} \right)^2 \tag{A.10}$$

Iterative Procedure

The equations for the dipole moment (Equations A.5 and A.6) must be supplemented with the hyperpolarizability (β):

$$p = \alpha E + \frac{1}{2}\beta E^2 \tag{A.11}$$

The above equation can no longer be solved analytically. However, using an iterative procedure within Mathematica[196] we have determined the first few terms of the expansion of this unknown function. Th resultant equation is too complex to reproduce here. However, for identical species (with unit charge) the expansion reduces to:

$$W = \frac{1}{r} - \frac{2\alpha}{r^4} + \frac{6\alpha^2}{r^7} - \frac{16\alpha^3}{r^{10}} - \frac{5\beta^2}{2r^{11}} + \frac{40\alpha^4}{r^{13}} + \frac{18\alpha\beta^2}{r^{14}} + ..., \tag{A.12}$$

while for non-identical species with equal and opposite charges, the expansion reduces to:

$$\begin{aligned} W \;=\; & -\frac{1}{r} - \frac{\alpha_1+\alpha_2}{r^4} - \frac{\beta_1+\beta_2}{2r^6} - \frac{6\alpha_1\alpha_2}{r^7} - \frac{4\alpha_1\beta_2+4\alpha_2\beta_1}{r^9} \\ & - \frac{8\alpha_1^2\alpha_2+8\alpha_2^2\alpha_1}{r^{10}} - \frac{5\beta_1\beta_2}{2r^{11}} + ..., \end{aligned} \tag{A.13}$$

where each subscript refers to a given ion.

Bibliography

[1] L. Pauling. The Sizes of Ions and the Structure of Ionic Crystals. *J. Am. Chem. Soc.*, **49**, 765, 1927.

[2] M. Bucher. Orbital-Moments Analysis of Ionic Radii in Silver and Copper Halides. *Phys. Rev. B*, **27**(10), 5919–5923, 1983.

[3] C. R. A. Catlow, J. Corish and P. W. M. Jacobs. A Calculation of the Frenkel Defect Formation Energy in Silver Chloride. *J. Phys. C*, **12**, 3433–3445, 1979.

[4] P. W. M. Jacobs, J. Corish and B. A. Devlin. Theoretical Calculation of Defect Energies for Silver Bromide. *Photog. Sci. Engng.*, **26**(1), 50–55, 1982.

[5] R. C. Baetzold, C. R. A. Catlow, J. Corish, F. M. Healy, P. W. M. Jacobs, M. Leslie and Y. T. Tan. The Effects of Three-Body Interactions on Crystal Properties and Defect Energies in Silver Halides. *J. Phys. Chem. Solids*, **50**(8), 791–800, 1989.

[6] M. Bucher. Lattice Spacing of Hypothetical AgCl and AgBr with "Switched-Off" van der Waals Interactions. *Phys. Rev. B*, **35**(12), 6432–6434, 1987.

[7] M. Bucher. Interaction Potentials for AgCl and AgBr. *Phys. Rev. B*, **30**(2), 947–956, 1984.

[8] C.-H. Kiang and W. A. Goddard III. Polarisation Effects in the AgBr Interaction Potential. *J. Phys. Chem.*, **99**, 14334–14339, 1995.

[9] K. Doll, P. Pyykkö and H. Stoll. Closed-Shell Interaction in Silver and Gold Chlorides. *J. Chem. Phys.*, **109**(6), 2339, 1998.

[10] P. R. Vijayaraghavan, R. M. Nicklow, H. G. Smith and M. K. Wilkinson. Lattice Dynamics of Silver Chloride. *Phys. Rev. B*, **1**(12), 4819–4826, 1970.

[11] Y. Fujii, S. Hoshino, S. Sakuragi, H. Kanzaki, J. W. Lynn and G. Shirane. Neutron Scattering Study of the Lattice Dynamics of AgBr at 4.4K. *Phys. Rev. B*, **15**(1), 358–368, 1977.

[12] K. Fischer, H. Bilz, R. Haberkorn and W. Weber. Covalency and Deformability of Ag^+-ions in the Lattice Dynamics of Silver Halides. *Phys. Stat. Sol. B*, **54**, 285–294, 1972.

[13] W. G. Kleppmann and H. Bilz. Effect of Quadrupolar Deformability on the Ionic Conductivity of Silver Salts. *Commun. Phys.*, **1**, 105–110, 1976.

[14] W. G. Kleppmann and W. Weber. Theory of the Quadrupolar Deformability in Silver Halides. *Phys. Rev. B*, **20**(4), 1669–1677, 1979.

[15] S. Ghosh, A. N. Basu and S. Sengupta. Unified Study of the Lattice Mechanical Properties of the AgCl Crystal. *Phys. Rev. B*, **23**(4), 1818–1826, 1981.

[16] T. Tomoyose, A. Fukuchi and M. Kobayashi. Influence of Quadrupolar Deformability on Phonon Dispersion in Silver and Copper Halides. *Solid State Ionics*, **167**, 83–90, 2004.

[17] B. Dorner, W. von der Osten and W. Bührer. Lattice Dynamics of AgBr. *J. Phys. C: Solid State Phys.*, **9**, 723–732, 1976.

[18] W. Hidshaw, J. T. Lewis and C. V. Briscoe. Elastic Constants of Silver Chloride from 4.2 to 300K. *Phys. Rev.*, **163**(3), 876–881, 1967.

[19] W. C. Hughes and L. S. Cain. Second-Order Elastic Constants of AgCl from 20 to 430C. *Phys. Rev. B*, **53**(9), 5174–5180, 1996.

[20] L. S. Cain and G. Hu. High-Temperature Elastic Constants of AgBr. *Phys. Rev. B*, **64**, 104104, 2001.

[21] W. Martienssen. Über die Excitonenbanden der Alkalihalogenidkristalle. *J. Phys. Chem. Solids*, **2**(4), 257–267, 1957.

[22] F. Seitz. Speculations on the Properties of the Silver Halide Crystals. *Rev. Mod. Phys.*, **23**(4), 328–352, 1951.

[23] J. A. Krumhansl. In R. G. Breckenridge, B. R. Russell and E. E. Hahn (editors) *Photoconductivity Conference*, page 450. John Wiley & Sons, Inc., New York, 1956.

[24] H. Tamura and T. Masumi. Cyclotron Resonance of Positive Holes in AgBr. *Solid State Commun.*, **12**(11), 1183–1186, 1973.

[25] T. Tani. *Photographic Sensitivity: Theory and Mechanisms*. Oxford Series in Optical and Imaging Sciences. Oxford University Press, 1996.

[26] F. C. Brown. *Point Defects in Solids*, volume 1, chapter 8. Plenum, New York, 1972.

[27] B. L. Joesten and F. C. Brown. Indirect Optical Absorption of AgCl-AgBr Alloys. *Phys. Rev.*, **148**(2), 919–927, 1966.

[28] K. Nakamura and W. von der Osten. Exciton Relaxation in AgCl Studied by Resonant Raman Scattering. *J. Phys. C: Solid State Phys.*, **16**, 6669–6680, 1983.

[29] F. Basanni, R. S. Knox and W. B. Fowler. Band Structure and Electronic Properties of AgCl and AgBr. *Phys. Rev.*, **137**(4A), 1217–1225, 1965.

[30] R. C. Birtcher, P. W. Deutsch, J. F. Wendelken and A. B. Kunz. Valence Band Structure in Silver Fluoride. *J. Phys. C*, **5**, 562–566, 1972.

[31] P. M. Scop. Band Structure of Silver Chloride and Silver Bromide. *Phys. Rev.*, **139**(3A), 934–940, 1965.

[32] A. B. Kunz. Electronic Structure of AgF, AgCl, and AgBr. *Phys. Rev. B*, **26**(4), 2070–2075, 1982.

[33] E. Aprà, E. Stefanovich, R. Dovesi and C. Roetti. An Ab Initio Hartree-Fock Study of Silver Chloride. *Chem. Phys. Lett.*, **186**(4,5), 329–335, 1991.

[34] F. Kirchhoff, J. M. Holender and M. J. Gillan. Energetics and Electronic Structure of Silver Chloride. *Phys. Rev. B*, **49**(24), 17420–17423, 1994.

[35] R. H. Victora. Calculated Electronic Structure of Silver Halide Crystals. *Phys. Rev. B*, **56**(8), 4417–4421, 1997.

[36] G. S. Nunes, P. B. Allen and J. L. Martins. Electronic Structure of Silver Halides. *Solid State Commun.*, **105**(6), 377–380, 1998.

[37] D. Vogel, P. Krüegr and J. Pollmann. Ab Initio Electronic Structure of Silver Halides Calculated with Self-Interaction and Relaxation-Corrected Pseudopotentials. *Phys. Rev. B*, **58**(7), 3865–3869, 1998.

[38] P. K. de Boer and R. A. de Groot. Conduction Band of the Photographic Compound AgCl. *J. Phys. Chem. A*, **103**(5113-5115), 1999.

[39] H. Overhof and U. Gerstmann. Spatial Distribution of the Conduction-Band Particle Density in Silver Halides. *Phys. Rev. B*, **62**(19), 12585–125, 2000.

[40] C. M. I. Okoye. Full-Potential Study of the Electronic Structure of Silver Halides. *Phys. Stat. Sol. B*, **234**(2), 580–589, 2002.

[41] L. J. Sham. Density-Functional Theory of the Energy Gap. *Phys. Rev. Lett.*, **51**(20), 1888–1891, 1983.

[42] M. T. Bennebroek, A. Arnold, O. G. Poluektov, P. G. Baranov and J. Schmidt. Spatial Distribution of the Wave Function of the Self-Trapped Exciton in AgCl. *Phys. Rev. B*, **53**(23), 15607, 1996.

[43] F. C. Brown. Hall Effect in AgCl at Low Temperature. *Phys. Rev.*, **92**(2), 502–503, 1953.

[44] R. K. Ahrenkiel. Studies of the Polaron Mobility in AgBr at High Temperature. *Phys. Rev.*, **180**(3), 859–863, 1969.

[45] P. Müller, S. Spenke and J. Teltow. Hole Conduction in Non-Stoichiometric Silver Chloride. *Phys. Stat. Sol.*, **41**(1), 81, 1970.

[46] R. K. Ahrenkiel and R. S. van Heyningen. Lifetime and Drift Mobility of Holes in AgBr. *Phys. Rev.*, **144**(2), 576–581, 1966.

[47] M. Hohne and M. Stasiw. ESR Detection of Self-Trapped Holes in AgCl. *Phys. Stat. Sol.*, **28**(1), 247, 1968.

[48] M. T. Bennebroek, A. V. Duijn-Arnold, J. Schmidt, O. G. Poluektov and P. G. Baranov. Self-Trapped Hole in Silver Halide Crystals: A Pulsed EPR/ENDOR Study at 95 GHz. *Phys. Rev. B*, **66**, 054305, 2002.

[49] J. P. Spoonhower and A. P. Marchetti. Trapped Holes in Silver Halides. *J. Phys. Chem. Solids*, **51**(7), 793–804, 1990.

[50] C. Kao, L. G. Rowan and L. M. Slifkin. EPR Study of Hole Trapping at Cation Vacancies in Silver Halides. *Phys. Rev. B*, **42**(5), 3142–3151, 1990.

[51] W. Jost and G. Nehlep. *Z. Phys. Chem. B Lpz*, **32**, 1, 1936.

[52] R. D. Fouchaux and R. O. Simmons. Measurements of Thermal Expansion and Thermal Equilibrium Defects in Silver Chloride. *Phys. Rev. A*, **136**(6a), 1664–1674, 1964.

[53] A. W. Lawson. Thermal Expansion in Silver Halides. *Phys. Rev.*, **78**, 185, 1950.

[54] H. C. Abbink and D. S. Martin. Ionic Conductivity of Silver Chloride Containing Cadmium Chloride. *J. Phys. Chem. Solids*, **27**, 205–215, 1966.

[55] J. K. Aboagye and R. J. Friauf. Anomalous High-Temperature Ionic Conductivity in the Silver Halides. *Phys. Rev. B*, **11**(4), 1654–1664, 1975.

[56] R. J. Friauf. *The Physics of Latent Image Formation in the Silver Halides.* World Scientific, Singapore, 1984.

[57] B. A. Devlin and J. Corish. A Theoretical and Experimental Study of Ionic Motion in Silver Bromide Crystals. *J. Phys. C: Solid State Phys.*, **20**(5), 705–721, 1987.

[58] A. P. Batra and L. M. Slifkin. Temperature Dependence of Frenkel-Defect Formation Energy Deduced from Diffusion of Sodium in Silver Chloride. *Phys. Rev. B*, **12**(8), 3473, 1975.

[59] A. M. Stoneham. *Theory of Defects in Solids.* Oxford University Press, 1975.

[60] M. T. Bennebroek, O. G. Poluektov, A. J. Zakrzewski, P. G. Baranov and J. Schmidt. Structure of the Intrinsic Shallow Electron Center in AgCl Studied by Pulsed Electron Nuclear Double Resonance Spectroscopy at 95 GHz. *Phys. Rev. Lett.*, **74**(3), 442–445, 1995.

[61] M. T. Bennebroek, A. Arnold, O. G. Poluektov, P. G. Baranov and J. Schmidt. Shallow Electron Centers in Silver Halides. *Phys. Rev. B*, **54**(16), 11276–11289, 1996.

[62] L. Cordone and M. U. Palma. Permanent Photoinduced Conductivity in Silver Halide Crystals. *Phys. Rev. Lett.*, **16**(1), 22–25, 1966.

[63] L. Cordone, S. L. Fornili and S. Micciancio. Nucleation of Hole Traps in Silver Halide Crystals. *Phys. Rev.*, **188**(3), 1404–1407, 1969.

[64] C. W. McCombie and A. B. Lidiard. Ratio of Ionic Conductivity to Tracer Diffusion in Interstitialcy Migration. *Phys. Rev.*, **101**, 1210, 1956.

[65] R. J. Friauf. Ionic Transport Processes in the Silver Halides. *J. Phys. Chem.*, **66**, 2380–2383, 1962.

[66] P. W. M. Jacobs, J. Corish and C. R. A. Catlow. Ionic Mobility in Silver Chloride. *J. Phys. C*, **13**(10), 1977–1988, 1980.

[67] R. J. Friauf. Diffusion of Silver in Silver Bromide and Evidence for Interstitialcy Migration. *Phys. Rev.*, **105**(3), 843–848, 1957.

[68] J. Corish and D. C. A. Mulcahy. The Ionic Conductivity of Cadmium-Doped Silver Chloride Crystals. *J. Phys. C*, **13**, 6459, 1980.

[69] J. F. Hamilton. The Silver Halide Photographic Process. *Adv. Phys.*, **37**(4), 359–441, 1988.

[70] J. E. Hove. Interstitialcy Diffusion Mechanism in Silver Chloride. *Phys. Rev.*, **102**(3), 915–916, 1956.

[71] R. C. Baetzold and R. S. Eachus. The Possibility of a Split Interstitial Silver Ion in AgCl. *J. Phys.: Condens. Matter*, **7**, 3991–3999, 1995.

[72] R. C. Baetzold, Y. T. Tan and P. W. Tasker. A Computational Approach to Silver Halide Surfaces. *Surf. Sci.*, **195**, 579–593, 1988.

[73] P. Tangyunyong, T. N. Rhodin, Y. T. Tan and K. J. Lushington. SEXAFS Study of AgBr(111) and (100) Surfaces and Comparison to Theoretical Models. *Surf. Sci.*, **255**(3), 259–268, 1991.

[74] J. F. Hamilton and L. E. Brady. A Model for the AgBr (111) Surface, Based on the Symmetry of Nucleation Sites for Evaporated Metal. *Surf. Sci.*, **23**(2), 389–402, 1970.

[75] G. Hegenbart and T. Müssig. Atomic Force Microscopy Studies of Atomic Structures on AgBr(111) Surfaces. *Surf. Sci.*, **275**(1-2), L655–L661, 1992.

[76] G. Travot, G. Sirand-Rey and J. Bernedo. Apparatus for the Ionic Conduction and Space Charge Measurements of Photographic Emulsions. *J. Phys. E: Sci. Instrum.*, **13**, 1231–1235, 1980.

[77] S. Danyluk and J. M. Blakely. Space Charge Regions at Silver Halide Surfaces: Experimental Results for Undoped AgCl. *Surf.Sci.*, **41**(2), 259–370, 1974.

[78] S. K. Wonnell and L. M. Slifkin. Subsurface Ionic Space Charges in Silver Chloride and Silver Bromide. *Solid State Ionics*, **75**, 101–106, 1995.

[79] K. Lehovec. Space-Charge Layer and Distribution of Lattice Defects at the Surface of Ionic Crystals. *J. Chem. Phys.*, **21**(7), 1123–1128, 1953.

[80] K. L. Kliewer. Space Charge in Ionic Crystals-III. Silver Halides Containing Divalent Cations. *J. Phys. Chem. Solids*, **27**(4), 705–717, 1966.

[81] R. B. Poeppel and J. M. Blakely. Origin of Equilibrium Space Charge Potentials in Ionic Crystals. *Surf. Sci.*, **15**(3), 507–523, 1969.

[82] J. F. Hamilton and L. E. Brady. The Role of Mobile Silver Ions in Latent-Image Formation. *J. Phys. Chem.*, **66**, 2384–2396, 1962.

[83] R. W. Gurney and N. F. Mott. The Theory of the Photolysis of Silver Bromide and the Photographic Latent Image. *Proc. R. Soc. Lond. A*, **164**, 151–167, 1938.

[84] J. Malinowski. Latent Image Formation in Silver Halides. *Photog. Sci. Eng.*, **14**(2), 112–121, 1970.

[85] T. Oikawa and T. Kaneda. Early Stages of Latent Formation in AgCl Grains Undoped or Doped with Iridium Ions. *J. Appl. Phys.*, **81**(6), 2465, 1997.

[86] R. C. Baetzold. Properties of Silver Clusters on AgBr Surface Sites. *Photog. Sci. Eng.*, **19**(1), 11–16, 1975.

[87] R. C. Baetzold. Electronic Effects in Silver Latent Image Particles. *J. Photog. Sci.*, **28**, 15–22, 1980.

[88] R. C. Baetzold. Calculated Properties of Ag Clusters on Silver Halide Cubic Surface Sites. *J. Phys. Chem. B*, **101**, 8180–8190, 1997.

[89] R. C. Baetzold. Properties of Silver Clusters Adsorbed to Silver Bromide. *J. Phys. Chem. B*, **105**, 3577–3586, 2001.

[90] R. C. Baetzold. Computational Study of Sulfur Sensitizing Centers on AgBr. *J. Imaging. Sci. Technol.*, **45**(3), 247–253, 2001.

[91] A. P. Marchetti, K. Lushington and R. Baetzold. Photophysics of Sulfur-Containing Centers on AgBr Surfaces. *J. Phys. Chem. B*, **107**, 136–146, 2003.

[92] T. A. Babcock, M. H. Sewell, W. C. Lewis and T. H. James. Hypersensitization of Spectroscopic Films and Plates Using Hydrogen Gas. *Astron. J.*, **79**(12), 1479–1487, 1974.

[93] K. Seki, H. Yanagi, Y. Kobayashi, T. Ohta and T. Tani. UV Photoemission Study of Dye / AgBr Interfaces in Relation to Spectral Sensitization. *Phys. Rev. B*, **49**(4), 2760–2766, 1994.

[94] J. W. Mitchell. The Basic Concepts of the Photoaggregation Theory. *J. Imag. Sci. Techn.*, **39**(3), 193–204, 1995.

[95] J. W. Mitchell. Photographic Sensitivity. *J. Photogr. Sci.*, **6**, 57–80, 1958.

[96] C. R. A. Catlow and W. C. Mackrodt (editors) *Computer Simulation of Solids*, volume 166 of *Lecture Notes in Physics*. Springer-Verlag, 1982.

[97] J. D. Gale and A. L. Rohl. The General Utility Lattice Program (GULP). *Mol. Simul.*, **29**(5), 291–341, 2003.

[98] P. P. Ewald. Die Berechnung Optischer und Elektrostatisher Gitterpotentiale. *Ann. Phys.*, **64**, 253–287, 1921.

[99] M. Leslie and M. J. Gillan. The Energy and Elastic Dipole Tensor of Defects in Ionic Crystals Calculated by the Supercell Method. *J. Phys C: Solid State Phys.*, **18**, 973–982, 1985.

[100] G. Makov and M. C. Payne. Periodic Boundary Conditions in Ab Initio Calculations. *Phys. Rev. B*, **51**(7), 4014–4022, 1995.

[101] J. E. Lennard-Jones. *Proc. Camb. Phil. Soc.*, **27**, 469, 1931.

[102] B. M. Axilrod and E. Teller. Interaction of the van der Waals Type Between Three Atoms. *J. Chem. Phys.*, **11**, 299–300, 1943.

[103] A. L. Rohl, K. Wright and J. D. Gale. Evidence from Surface Phonons for the (2 x 1) Reconstruction of the (1 0 1 4) Surface of Calcite from Computer Simulation. *Am. Mineral.*, **88**, 921–925, 2003.

[104] B. G. Dick and A. W. Overhauser. Theory of Dielectric Constants of Alkali Halide Crystals. *Phys. Rev.*, **112**(1), 90–103, 1958.

[105] A. D. B. Woods, W. Cochran and B. N. Brockhouse. Lattice Dynamics of Alkali Halide Crystals. *Phys. Rev.*, **119**(3), 980–999, 1960.

[106] C. R. A. Catlow, K. M. Diller and M. J. Norgett. Interatomic Potentials for Alkali Halides. *J. Phys. C: Solid State*, **10**, 1395–1412, 1977.

[107] C. R. A. Catlow, J. Corish, K. M. Diller, P. W. M. Jacobs and M. J. Norgett. A Theoretical Study of Intrinsic and Extrinsic Defect Properties of Alkali Halides. *J. Phys. (Paris)*, **37**(12), C7–253, 1976.

[108] C. R. A. Catlow, I. D. Faux and M. J. Norgett. Shell and Breathing Shell-Model Calculations for Defect Formation Energies and Volumes in Magnesium Oxide. *J. Phys. C: Solid State Phys.*, **9**(3), 419–429, 1976.

[109] A. Aguado, L. Bernasconi, S. Jahn and P. A. Madden. Multipoles and Interaction Potentials in Ionic Materials from Planewave-DFT Calculations. *Faraday Discuss.*, **124**, 171–184, 2003.

[110] M. Wilson, P. A. Madden and B. J. Costa-Cabral. Quadrupole Polarization in Simulations of Ionic Systems: Application to AgCl. *J. Phys. Chem.*, **100**, 1227–1237, 1996.

[111] J. Applequist. A Multipole Interaction Theory of Electric Polarization of Atomic and Molecular Assemblies. *J. Chem. Phys.*, **83**(2), 809–826, 1985.

[112] P. A. Madden and M. Wilson. 'Covalent' Effects in 'Ionic' Systems. *Chem. Soc. Rev.*, pages 339–350, 1996.

[113] R. Fletcher and M. J. D. Powell. A rapidly convergent descent method for minimization. *Comput. J.*, **6**(2), 163–168, 1963.

[114] D. F. Shanno. Conditioning of quasi-Newton methods for function minimization. *Math. Comput.*, **24**(111), 647–656, 1970.

[115] L. H. Thomas. The Calculation of Atomic Fields. *Proc. Cambridge Phil. Roy. Soc.*, **23**, 542–548, 1927.

[116] E. Fermi. Un Metodo Statistico per la Determinazione di Alcune Priorieta dell'Atome. *Rend. Accad. Naz. Lincei*, **6**, 602–607, 1927.

[117] P. Hohenberg and W. Kohn. Inhomogeneous Electron Gas. *Phys. Rev.*, **136**(3B), 1964.

[118] W. Kohn and L. J. Sham. Self-Consistent Equations Including Exchange and Correlation Effects. *Phys. Rev.*, **140**(4A), 1965.

[119] F. Herman, J. P. Van Dyke and I. P. Ortenburger. Improved Statistical Exchange Approximation for Inhomogeneous Many-Electron Systems. *Phys. Rev. Lett.*, **22**(16), 807–811, 1969.

[120] A. D. Becke. Density-Functional Exchange-Energy Approximation with Correct Asymptotic Behaviour. *Phys. Rev. A*, **38**, 3098–3100, 1988.

[121] J. P. Perdew and Y. Wang. Accurate and Simple Analytic Representation of the Electron-Gas Correlation-Energy. *Phys. Rev. B*, **45**(23), 13244–13249, 1992.

[122] J. P. Perdew, K. Burke and M. Ernzerhof. Generalized Gradient Approximation Made Simple. *Phys. Rev. Lett.*, **77**, 3865–3868, 1996.

[123] A. D. Becke. Density-Functional Thermochemistry. III. The Role of Exact Exchange. *J. Chem. Phys.*, **98**(7), 5648–5652, 1993.

[124] A. D. Becke. Density-Functional Thermochemistry. V. Systematic Optimization of Exchange-Correlation Functionals. *J. Chem. Phys.*, **107**(20), 8554–8560, 1997.

[125] L. A. Curtiss, K. Raghavachari, G. W. Trucks and J. A. Pople. Gaussian-2 Theory for Molecular Energies of First- and Second-Row Compounds. *J. Chem. Phys.*, **94**(11), 7221–7230, 1991.

[126] F. A. Hamprecht, A. J. Cohen, D. J. Tozer and N. C. Handy. Development and Assessment of New Exchange-Correlation Functionals. *J. Chem. Phys.*, **109**(15), 6264–6271, 1998.

[127] Q. Zhao, R. C. Morrison and R. G. Parr. From Electron Densities to Kohn-Sham Kinetic Energies, Orbital Energies, Exchange-Correlation Potentials, and Exchange-Correlation Energies. *Phys. Rev. A*, **50**(3), 2138–2142, 1994.

[128] P. J. Wilson, T. J. Bradley and D. J. Tozer. Hybrid Exchange-Correlation Functional Determined from Thermochemical Data and Ab Initio Potentials. *J. Chem. Phys.*, **115**(20), 9233–9242, 2001.

[129] D. R. Hamann, M. Schlüter and C. Chiang. Norm-Conserving Pseudopotentials. *Phys. Rev. Lett.*, **43**(20), 1494–1498, 1979.

[130] I. M. Boswarva and A. B. Lidiard. Energy of Formation of Schottky Defects in Ionic Crystals. *Philos. Mag.*, **16**, 805, 1967.

[131] A. L. Shluger, A. S. Foster, J. L. Gavartin and P. V. Sushko. Defects in Wide-Gap Oxides: Computer Modelling and Challenges. In J. Greer, A. Korkin and J. Labanowski (editors) *Nano and Giga Challenges in Microelectronics*, pages 151–222. Elsevier, 2003.

[132] A. M. Stoneham, C. R. A. Catlow and A. Lidiard (editors) *J. Phys.: Condens. Matter*, volume 16(27). Institute of Physics, July 2004.

[133] L. Kleinman. Comment on the Average Potential of a Wigner Solid. *Phys. Rev. B*, **24**(12), 7412–7414, 1981.

[134] D. B. Laks, C. G. Van de Walle, G. F. Neumark, P. E. Blöchl and S. T. Pantelides. Native Defects and Self-Compensation in ZnSe. *Phys. Rev. B*, **45**(19), 10965–10978, 1992.

[135] G. Roma and Y. Limoge. A First Principles Study of Native Defects in α-Quartz. *Nucl. Instrum. Meth. B*, **202**, 120–124, 2003.

[136] M. F. Guest, J. H. van Lenthe, J. Kendrick, K. Schoffel, P. Sherwood, with contributions from R D Amos, R. J. Buenker, H. J. J. van Dam, M. Dupuis, N. C. Handy, I. H. Hillier, P. J. Knowles, V. Bonacic-Koutecky, W. von Niessen, R. J. Harrison, A. P. Rendell, V. R. Saunders, A. J. Stone, D. J. Tozer and A. H. de Vries. GAMESS-UK. CCLRC Daresbury Lab, Warrington, UK; derived from the original GAMESS code: M Dupuis, D Spangler, J Wendoloski. NRCC Software Catalog, vol. 1, program QG01 (GAMESS); NRCC: Berkely, 1980.

[137] M. J. Frisch, G. W. Trucks, H. B. Schlegel, G. E. Scuseria, M. A. Robb, J. R. Cheeseman, J. A. Montgomery, Jr., T. Vreven, K. N. Kudin, J. C. Burant, J. M. Millam, S. S. Iyengar, J. Tomasi, V. Barone, B. Mennucci, M. Cossi, G. Scalmani, N. Rega, G. A. Petersson, H. Nakatsuji, M. Hada, M. Ehara, K. Toyota, R. Fukuda, J. Hasegawa, M. Ishida, T. Nakajima, Y. Honda, O. Kitao, H. Nakai, M. Klene, X. Li, J. E. Knox, H. P. Hratchian, J. B. Cross, V. Bakken, C. Adamo, J. Jaramillo, R. Gomperts, R. E. Stratmann, O. Yazyev, A. J. Austin, R. Cammi, C. Pomelli, J. W. Ochterski, P. Y. Ayala, K. Morokuma, G. A. Voth, P. Salvador, J. J. Dannenberg, V. G. Zakrzewski, S. Dapprich, A. D. Daniels, M. C. Strain, O. Farkas, D. K. Malick, A. D. Rabuck, K. Raghavachari, J. B. Foresman, J. V. Ortiz, Q. Cui, A. G. Baboul, S. Clifford, J. Cioslowski, B. B. Stefanov, G. Liu, A. Liashenko, P. Piskorz, I. Komaromi, R. L. Martin, D. J. Fox, T. Keith, M. A. Al-Laham, C. Y. Peng, A. Nanayakkara, M. Challacombe, P. M. W. Gill, B. Johnson, W. Chen, M. W. Wong, C. Gonzalez and J. A. Pople. Gaussian 03, Revision C.02. Gaussian, Inc., Wallingford, CT, 2004.

[138] J. M. Vail, A. H. Harker, J. H. Harding and P. Saul. Calculations for electronic point defects with self-consistent lattice polarisation: the F^+ centre in MgO. *J. Phys. C: Solid State Phys.*, **17**, 3401–3414, 1984.

[139] J. H. Harding, A. H. Harker, P. B. Keegstra, R. Pandey, J. M. Vail and C. Woodward. *Physica B*, **131**, 151, 1985.

[140] P. Sherwood, A. H. de Vries, M. F. Guest, G. Schreckenbach, C. R. A. Catlow, S. A. French, A. A. Sokol, S. T. Bromley, W. Thiel, A. J. Turner, S. Billeter, F. Terstegen, S. Thiel, J. Kendrick, S. C. Rogers, J. Casci, M. Watson, F. King, E. Karlsen, M. Sjøvoll, A. Fahmi, A. Schäfer and C. Lennartz. QUASI: A General Purpose Implementation of the QM/MM Approach and its Application to Problems in Catalysis. *J. Mol. Struc-Theochem*, **632**, 1–28, 2003.

[141] P. V. Sushko. *Development and Application of Embedded Cluster Methodologies for Defects in Ionic Materials.* Ph.D. thesis, The Royal Institution of Great Britain, 2000.

[142] C. Pisani, F. Corà, R. Nada and R. Orlando. Hartree-Fock perturbed-cluster treatment of local defects in crysals I. The EMBED program: general features. *Comp. Phys. Comm.*, **82**, 139–156, 1994.

[143] N. Govind, Y. A. Wang, A. J. R. de Silva and E. A. Carter. Accurate ab initio energetics of extended systems via explicit correlation embedded in a density functional environment. *Chem. Phys. Lett.*, **295**, 129–134, 1998.

[144] D. Bakowles and W. Thiel. Hybrid Models for Combined Quantum Mechanical and Molecular Mechanical Approaches. *J. Phys. Chem.*, **100**, 10580–10594, 1996.

[145] W. Jost. Diffusion and Electrolytic Conduction in Crystals (Ionic Semiconductors). *J. Chem. Phys.*, **1**, 466–475, 1933.

[146] A. A. Sokol, S. T. Bromley, S. A. French, C. R. A. Catlow and P. Sherwood. Hybrid QM/MM Embedding Approach for the Treatment of Localized Surface States in Ionic Materials. *Int. J. Quantum Chem.*, **99**, 695–712, 2004.

[147] A. A. Sokol and C. R. A. Catlow. In preparation.

[148] J. D. Gale. GULP: A Computer Program for the Symmetry-Adapted Simulation of Solids. *J. Chem. Soc., Faraday Trans.*, **93**(4), 629–637, 1997.

[149] D. H. Gay and A. L. Rohl. MARVIN - A New Computer Code for Studying Surfaces and Interfaces and its Application to Calculating the Crystal Morphologies of Corundum and Zircon. *J. Chem. Soc., Faraday Trans.*, **91**(5), 925–936, 1995.

[150] J. E. Mayer. Dispersion and Polarisability and the van der Waals Potential in the Alkali Halides. *J. Chem. Phys.*, **1**, 270–279, 1933.

[151] R. D. Banhatti and Y. V. G. S. Murti. Role of Induced Quadrupoles in the Simulation of Intrinsic Point Defects in AgCl and NaCl. *Phys. Rev. B*, **48**(10), 6839–6853, 1993.

[152] J. D. Gale. 2001. Private Communication.

[153] M. Leslie. Daresbury Laboratory Report DL/SCI/TM3IT, 1982.

[154] J. D. Gale, C. R. A. Catlow and W. C. Mackrodt. Periodic Ab Initio Determination of Interatomic Potentials for Alumina. *Modelling Simul. Mater. Sci. Eng.*, **1**, 73–81, 1992.

[155] U. Puntambekar, J. M. Recio and R. Pandey. Defect Energy Calculations of Alkali Chlorides using Ab Initio Potentials. *Solid State Commun*, **85**(5), 423–425, 1993.

[156] P. T. Wedepohl. Influence of Electron Distribution on Atomic Interaction Potentials. *Proc. Phys. Soc.*, **92**, 79–93, 1967.

[157] S. Sawada and K. Nakamura. Theory of Surface Rumpling in Rock-Salt Structured Ionic Crystals. *J. Phys. C: Solid State Phys.*, **12**(6), 1183–1193, 1979.

[158] O. Robach, G. Renaud and A. Barbier. Very-High-Quality MgO(001) Surfaces: Roughness, Rumpling and Relaxation. *Surf. Sci.*, **401**, 227–235, 1998.

[159] A. Losch and H. Niehus. Structure analysis of the KBr(100) surface - An investigation with a new method for surface analysis of insulators. *Surf. Sci.*, **420**(2-3), 148–156, 1999.

[160] M. D. Segall, P. J. D. Lindan, M. J. Probert, C. J. Pickard, P. J. Hasnip, S. J. Clark and M. C. Payne. First-Principles Simulation: Ideas, Illustrations and the CASTEP Code. *J. Phys.: Condens. Matter*, **14**, 2717–2744, 2002.

[161] D. D. Koelling and B. N. Harmon. A Technique for Relativistic Spin-Polarised Calculations. *J. Phys. C*, **10**, 3107–3114, 1977.

[162] H. J. Monkhurst and J. D. Pack. On Special Points for Brillouin Zone Integrations. *Phys. Rev. B*, **13**, 5188, 1976.

[163] B. Simard, P. A. Hackett, A. M. James and P. R. R. Langridge-Smith. The Bond Length of the Silver Dimer. *Chem. Phys. Lett.*, **186**, 415–422, 1991.

[164] Q. Ran, R. W. Schmude, K. A. Gingerich and D. W. Wilhite. Dissociation Energy and Enthalpy of Formation of Gaseous Silver Dimer. *J. Phys. Chem.*, **97**(8535-8540), 1993.

[165] D. R. Lide (editor) *Handbook of Chemistry and Physics*. CRC Press, 83rd edition, 2002-2003.

[166] K. P. Huber and G. Herzberg. *Molecular Spectra and Molecular Structure Constants of Diatomic Molecules*. Van Nostrand, New York, 1979.

[167] A. S. Abbasov, T. K. Azizov, N. A. Alleva, I. Y. Aliev, F. M. Mustafaev and F. M. Mamedov. *Zh. Fiz. Khim.*, **50**, 2172, 1976.

[168] A. G. Gaydon. *Dissociation Energies and Spectra of Diatomic Molecules*. Chapman & Hall, London, 3rd edition, 1968.

[169] D. L. Hildenbrand and K. H. Lau. Thermochemistry of Gaseous AgCl, Ag3Cl3, and CuCl. *High Temp. Mater. Sci.*, **35**, 11–20, 1996.

[170] G. Makov, R. Shah and M. C. Payne. Periodic Boundary Conditions in Ab Initio Calculations. II. Brillouin-Zone Sampling for Aperiodic Systems. *Phys. Rev. B*, **53**(23), 15513–15517, 1996.

[171] R. M. Martin. *Electronic Structure: Basic Theory and Practical Methods*. Cambridge University Press, 2004.

[172] H. Ott. *Z. Krist.*, **63**, 222, 1926.

[173] A. P. Marchetti and G. L. Bottger. Optical Absorption Spectrum of AgF. *Phys. Rev. B*, **3**(8), 2604–2607, 1971.

[174] B. N. Onwuagba. The Electronic Structure of AgF, AgCl and AgBr. *Solid State Commun*, **97**(4), 267–271, 1996.

[175] P. A. Schultz. Charged Local Defects in Extended Systems. *Phys. Rev. Lett.*, **84**(9), 1942–1945, 2000.

[176] J. Lento, J.-L. Mozos and R. M. Nieminen. Charged Point Defects in Semiconductors and the Supercell Approach. *J. Phys.: Condens. Matter*, **14**(10), 2637–2654, 2002.

[177] T. D. Pawlik. 2004. Private Communication.

[178] J. Corish and P. W. M. Jacobs. Ionic Conductivity of Silver Chloride Single-Crystals. *J. Phys. Chem. Solids*, **33**(9), 1799, 1972.

[179] M. D. Weber and R. J. Friauf. Interstitialcy Motion in the Silver Halides. *J. Phys. Chem. Solids*, **30**, 407–419, 1969.

[180] A. K. Shukla, S. Ramdas and C. N. Rao. Mechanism of Ion Movement in AgCl and AgBr. *J. Solid State Chem.*, **8**, 120–125, 1973.

[181] J. Corish. Calculated and Experimental Defect Parameters for Silver Halides. *J. Chem. Soc., Faraday Trans. 2*, **85**(5), 437–456, 1989.

[182] M. Ueta, H. Kanzaki, K. Koboyashi, Y. Toyozawa and E. Hanamura. *Exitonic Processes in Solids*, chapter 6. Springer, Berlin, 1986.

[183] H. Kanzaki and S. Sakuragi. Optical Absorption and Luminescence of Excitons in Silver Halides Containing Isoelectronic Impurities. Part II. AgBr:Cl^- and AgBr. *J. Phys. Soc. Jpn.*, **29**(4), 924–935, 1970.

[184] R. C. Brandt and F. C. Brown. Induced Infrared Absorption due to Bound Charge in the Silver Halides. *Phys. Rev.*, **181**(3), 1241, 1969.

[185] J. L. Gavartin, P. V. Sushko and A. L. Shluger. Modeling Charge Self-Trapping in Wide-Gap Dielectrics: Localization Problem in Local Density Functionals. *Phys. Rev. B*, **67**, 035108, 2003.

[186] R. S. Eachus, T. D. Pawlik and R. C. Baetzold. Multifrequency Electron Paramagnetic Resonance and Electron-Nuclear Double-Resonance Studies of Photo-Hole Processes in AgBr and AgCl Emulsion Grains. *J. Phys.: Condens. Matter*, **12**, 8893–8911, 2000.

[187] G. Pacchioni, F. Frigoli, D. Ricci and J. A. Weil. Theoretical Description of Hole Localization in a Quartz Al Center: The Importance of Exact Electron Exchange. *Phys. Rev. B*, **63**(5), 054102, 2000.

[188] Y. Zhao, B. J. Lynch and D. G. Truhlar. Development and Assessment of a New Hybrid Density Functional Model for Thermochemical Kinetics. *J. Phys. Chem. A*, **108**(14), 2715–2719, 2004.

[189] J. To, A. A. Sokol, S. A. French, N. Kaltsoyannis and C. R. A. Catlow. Hole Localization in $[AlO_4]^0$ Defects in Silica Materials. *J. Chem. Phys.*, **122**(14), 144704, 2005.

[190] B. Delley. From Molecules to Solids with the DMol3 Approach. *J. Chem. Phys.*, **113**(18), 7756, 2000.

[191] S. Suhai, P. S. Bagus and J. Ladik. An Error Analysis for Hartree-Fock Crystal Orbital Calculations. *Chem. Phys.*, **68**(3), 467–471, 1982.

[192] D. Andrae, U. Haussermann, M. Dolg, H. Stoll and H. Preuss. Energy-Adjusted Ab Initio Pseudopotentials for the 2nd and 3rd Row Transition-Elements. *Theor. Chim. Acta*, **77**(2), 123–141, 1990.

[193] H. Stoll, P. Fuentealba, P. Schwerdtfeger, J. Flad, L. v Szentpály and H. Preuss. Cu and Ag as One-Electron Atoms: Cl Results and Quadrupole Corrections for Cu_2, Ag_2 CuH and AgH. *J. Chem. Phys.*, **81**(6), 2732–2736, 1984.

[194] A. A. Sokol. 2004. Private Communication.

[195] S. A. French, A. A. Sokol, S. T. Bromley, C. R. A. Catlow, S. C. Rogers, F. King and P. Sherwood. From CO_2 to Methanol by Hybrid QM/MM Embedding. *Angew. Chem.*, **113**(23), 4569–4572, 2001.

[196] Wolfram Research, Inc. *Mathematica*. Champaign, Illinois, 4.1 edition, 2001.